The Employment of Aerodynamic Forces to Obtain Maximum Range of a Rocket Missile

DEREK F. LAWDEN, M.A.

(Canterbury University, New Zealand)

SUMMARY: The programming of the thrust direction of a rocket missile, to obtain maximum range over a flat earth by the most favourable employment of the aerodynamic forces, is considered for the special case when these forces are small by comparison with the missile weight. The cases of a V.2-type missile, (*a*) with lift and (*b*) without lift, are dealt with in detail and numerical results have been computed.

1. Introduction

In an earlier paper[1], the problem of achieving maximum range with a rocket missile by appropriate choice of the thrust direction programme was solved, in principle, under very general conditions. In the same paper, a complete solution was found for the special case of a missile being fired over a flat earth and subject to no air resistance. It was found that the direction of thrust had then to be kept fixed. The effect of earth curvature and the consequent variation in gravity have been discussed in a second paper[2]. In the present paper, an attempt is made to assess the effect which the presence of an atmosphere will have upon the optimum trajectory. In general, the calculation of the trajectory of maximum range has been shown[1] to involve the estimation of the conditions at "all-burnt" and an integration backwards along the missile track to the instant of firing. The estimated conditions at "all-burnt" have then to be adjusted until the rocket co-ordinates and velocity components at the launcher are correct. Having programmed an electronic computer for the backwards integration, this process of adjustment could be carried out without too great difficulty. However, the author's resources do not extend further than a desk machine and accordingly he has been forced to restrict himself to a special case for which it is possible to avoid the laborious procedure, but which will, none the less, reveal the main features of the atmospheric effect. This is the case for which the aerodynamic forces are small by comparison with the missile weight, so that the atmospheric effect can be regarded as a perturbation superposed on the known optimum trajectory in the absence of aerodynamic forces. Aerodynamic forces would be relatively small for a large intercontinental missile or for a missile launched at high altitude, though possibly not quite small enough to satisfy fully the assumptions of the present analysis. However, it may be expected

Received August 1957.

[The Aeronautical Quarterly, Vol. IX, May 1958]

that the main characteristics of the optimum thrust direction programme, in the case where the aerodynamic forces are relatively large, will be qualitatively similar to those for the special case to be considered, and hence that the results obtained will be of significance under more general conditions than those assumed in their calculation.

NOTATION

A	*see* equation (7)
A_{rs}, B_{rs}	values of α_{rs}, β_{rs} respectively on the optimum trajectory in the absence of aerodynamic forces (this will be referred to as trajectory A)
$\varepsilon A_{rs}', \varepsilon B_{rs}'$	first-order corrections to A_{rs}, B_{rs} to allow for aerodynamic forces
D	drag component
f	acceleration component due to motor thrust
F_1, F_2	components of missile retardation due to gravity and/or aerodynamic forces
F_1', F_2'	values taken by the expressions for F_1, F_2 on trajectory A
g	acceleration due to gravity
G_1, G_2	*see* equation (4)
l_1, l_2	direction cosines of direction of motor thrust
L	lift component
L_1, L_2	values of l_1, l_2 on trajectory A
$\varepsilon L_1', \varepsilon L_2'$	first-order corrections to L_1, L_2 to allow for aerodynamic forces
M	rocket mass
N_1, N_2	*see* equation (27)
N_1', N_2'	*see* equation (28)
q_1, q_2	rocket's co-ordinates at "all-burnt"
$\dot{q}_1, \dot{q}_2$	rocket's velocity components at "all-burnt"
Q_1, Q_2	values of q_1, q_2 on trajectory A
$\varepsilon Q_1', \varepsilon Q_2'$	first-order corrections to Q_1, Q_2 to allow for aerodynamic forces
$\dot{Q}_1, \dot{Q}_2$	values of $\dot{q}_1$, $\dot{q}_2$ on trajectory A
$\varepsilon \dot{Q}_1', \varepsilon \dot{Q}_2'$	first-order corrections to $\dot{Q}_1$, $\dot{Q}_2$ to allow for aerodynamic forces
R	missile range
t	time after launching
T	value of t at "all-burnt"
v	rocket velocity
x_1, x_2	co-ordinates of the rocket

X_1, X_2 values of x_1, x_2 on trajectory A

$\varepsilon X_1', \varepsilon X_2'$ first-order corrections to X_1, X_2 to allow for aerodynamic forces

y_{ik}, z_{ik} *see* equations (5)

Y_{ik}, Z_{ik} values of y_{ik}, z_{ik} on trajectory A

$\varepsilon Y_{ik}', \varepsilon Z_{ik}'$ first-order corrections to Y_{ik}, Z_{ik} to allow for aerodynamic forces

α_{rs}, β_{rs} *see* after equation (7)

δ angle of yaw

δ_{ik} Kronecker deltas

ε small parameter multiplying aerodynamic forces

θ inclination of the rocket's velocity to the horizontal

ϕ inclination of the rocket thrust to the horizontal

ρ atmospheric density

ρ_0 atmospheric density at sea level

2. An Extension of the General Theory

If Ox_1, Ox_2 are horizontal and vertical axes respectively through the launcher and lying in the plane of the trajectory, the equations of motion of the missile are

$$\ddot{x}_i + F_i = f l_i, \qquad (i = 1, 2) \quad . \quad . \quad . \quad . \quad . \quad (1)$$

where f is the acceleration due to the motor thrust, (l_1, l_2) are the direction cosines of the direction of thrust and $(-F_1, -F_2)$ are the net components of force per unit mass acting upon the rocket due to all agencies but its own thrust. In Ref. 1 it was assumed that the F_i were explicitly expressible as functions of the variables x_i, $\dot{x}_i$, M (rocket mass) and t. However, since the aerodynamic lift force will depend upon the orientation of the rocket axis relative to the direction of motion, the theory will now be extended by assuming that the direction of this axis is along the line of thrust and hence that

$$F_i = F_i(x_1, x_2, \dot{x}_1, \dot{x}_2, l_1, l_2, M, t) \quad . \quad . \quad . \quad . \quad (2)$$

Proceeding as in Ref. 1, it can now be shown that the thrust direction programme for maximum range R is determined by the equation

$$l_1 : l_2 = \left[G_1 \left(1 - \frac{1}{f} \frac{\partial F_1}{\partial l_1} \right) - G_2 \frac{\partial F_2}{\partial l_1} \right] : \left[G_2 \left(1 - \frac{1}{f} \frac{\partial F_2}{\partial l_2} \right) - G_1 \frac{\partial F_1}{\partial l_2} \right], \qquad (3)$$

where $$G_i = \frac{\partial R}{\partial q_r} \alpha_{ri} + \frac{\partial R}{\partial \dot{q}_r} \beta_{ri},^* \quad . \quad . \quad . \quad . \quad . \quad (4)$$

*The summation convention is operative in equation (4) and throughout the paper.

WAYNE STATE UNIVERSITY LIBRARIES
KRESGE-HOOKER SCIENCE LIBRARY

and (q_1, q_2), $(\dot{q}_1, \dot{q}_2)$ are the rocket co-ordinates and velocity components respectively at "all-burnt." The functions α_{rs}, β_{rs} have already been introduced in Ref. 1 as follows.

$$\text{Let} \quad y_i = y_{ik}(t), \quad z_i = z_{ik}(t) \quad (i=1,2; \quad k=1,2,3,4) \quad . \quad . \quad (5)$$

represent a linearly independent set of solutions of the equations

$$\left.\begin{aligned} \dot{z}_i + \frac{\partial F_i}{\partial \dot{x}_j} z_j + \frac{\partial F_i}{\partial x_j} y_j = 0, \\ \dot{y}_i - z_i = 0. \end{aligned}\right\} (i=1,2) \quad . \quad . \quad . \quad . \quad . \quad (6)$$

Forming the determinant

$$A = \begin{vmatrix} z_{11} & z_{12} & z_{13} & z_{14} \\ z_{21} & z_{22} & z_{23} & z_{24} \\ y_{11} & y_{12} & y_{13} & y_{14} \\ y_{21} & y_{22} & y_{23} & y_{24} \end{vmatrix}, \quad . \quad . \quad . \quad . \quad . \quad (7)$$

the quantities α_{rs}, β_{rs} are the determinants formed from A by replacement of its s^{th} row by the elements

$$y_{r1}(T), \; y_{r2}(T), \; y_{r3}(T), \; y_{r4}(T),$$

and $\quad z_{r1}(T), \; z_{r2}(T), \; z_{r3}(T), z_{r4}(T), \quad$ respectively.

3. Solution for Small Aerodynamic Forces

Neglecting earth curvature and rotation, the equations of motion (1) will be written in the form

$$\left.\begin{aligned} \ddot{x}_1 + \varepsilon F_1 = f l_1, \\ \ddot{x}_2 + g + \varepsilon F_2 = f l_2, \end{aligned}\right\} \quad . \quad . \quad . \quad . \quad . \quad . \quad . \quad (8)$$

where $(-\varepsilon F_1, \; -\varepsilon F_2)$ are net components of the aerodynamic forces per unit mass and ε is a small parameter.

If, now, in the absence of an atmosphere, the optimum trajectory and thrust direction programme are determined by the equations

$$x_i = X_i(t), \quad . \quad . \quad . \quad . \quad . \quad . \quad . \quad (9)$$

$$l_i = L_i(t), \quad . \quad . \quad . \quad . \quad . \quad . \quad . \quad (10)$$

respectively, the presence of the small aerodynamic forces can be allowed for by replacement of these equations by

$$x_i = X_i(t) + \varepsilon X_i'(t) + O(\varepsilon^2), \quad . \quad . \quad . \quad . \quad . \quad (11)$$

$$l_i = L_i(t) + \varepsilon L_i'(t) + O(\varepsilon^2), \quad . \quad . \quad . \quad . \quad . \quad (12)$$

respectively. Substituting from equations (11) and (12) into equations (8), and equating coefficients of like powers of ε from the two members of each equation, it will be found that

$$\ddot{X}_1 = fL_1, \quad \ddot{X}_2 + g = fL_2, \quad . \quad . \quad . \quad . \quad . \quad (13)$$

$$\ddot{X}_i' + F_i' = fL_i' \quad (i = 1, 2), \quad . \quad . \quad . \quad . \quad . \quad (14)$$

where F_i' is the result of substituting $x_i = X_i$, $l_i = L_i$ into F_i.

Similarly, it will be assumed that

$$\left.\begin{aligned} y_i &= Y_i + \varepsilon Y_i' + O(\varepsilon^2), \\ z_i &= Z_i + \varepsilon Z_i' + O(\varepsilon^2). \end{aligned}\right\} \quad . \quad . \quad . \quad . \quad . \quad (15)$$

Substitution in equations (6) then yields the equations

$$\dot{Z}_i = 0, \quad \dot{Y}_i - Z_i = 0, \quad . \quad . \quad . \quad . \quad . \quad (16)$$

$$\left.\begin{aligned} \dot{Z}_i' + \frac{\partial F_i'}{\partial \dot{X}_j} Z_j + \frac{\partial F_i'}{\partial X_j} Y_j &= 0, \\ \dot{Y}_i' - Z_i' &= 0. \end{aligned}\right\} \quad . \quad . \quad . \quad . \quad (17)$$

If the fundamental set of solutions of equations (6) is taken to be the one which at $t = T$ ("all-burnt") satisfies the conditions

$$z_{ik} = \delta_{ik}, \quad y_{ik} = \delta_{i+2,k}, \quad . \quad . \quad . \quad . \quad . \quad (18)$$

where $\delta_{ik} = 0$ $(i \neq k)$ and is unity otherwise, then, since the conditions (18) are to be satisfied for all ε,

$$Z_{ik} = \delta_{ik}, \quad Y_{ik} = \delta_{i+2,k}, \quad . \quad . \quad . \quad . \quad . \quad (19)$$

$$Z_{ik}' = Y_{ik}' = 0, \quad . \quad . \quad . \quad . \quad . \quad 20)$$

at $t = T$.

The four sets of solutions of the equations (16) satisfying the conditions (19) are

$$\left.\begin{array}{llll} (i) & Z_{11}=1, & Z_{21}=0, & Y_{11}=t-T, \quad Y_{21}=0; \\ (ii) & Z_{13}=0, & Z_{23}=0, & Y_{13}=1, \quad Y_{23}=0; \\ (iii) & Z_{13}=0, & Z_{23}=0, & Y_{13}=1, \quad Y_{23}=0; \\ (iv) & Z_{14}=0, & Z_{24}=0, & Y_{14}=0, \quad Y_{24}=1. \end{array}\right\} \quad . \quad (21)$$

Employing each of these sets of values for the quantities Y_i and Z_i in equations (17) in turn, corresponding sets of values for the quantities Y_i', Z_i' may be found by integration backwards from $t=T$, subject to the initial conditions (20). The quantities $\partial F_i'/\partial X_j$, $\partial F_i'/\partial \dot{X}_j$ are to be calculated along the optimum trajectory in the absence of an atmosphere. This trajectory can be found by the method of Ref. 1 and thus these quantities are available for integration.

The determinants α_{rs}, β_{rs} may now be computed in the form

$$\left.\begin{aligned} \alpha_{rs} &= A_{rs}+\varepsilon A_{rs}'+O(\varepsilon^2), \\ \beta_{rs} &= B_{rs}+\varepsilon B_{rs}+O(\varepsilon^2), \end{aligned}\right\} \quad . \quad . \quad . \quad . \quad . \quad (22)$$

where

$$\left.\begin{array}{ll} A_{11}=T-t, & A_{12}=0, \\ A_{21}=0, & A_{22}=T-t, \\ B_{11}=1, & B_{12}=0, \\ B_{21}=0, & B_{22}=1, \end{array}\right\} \quad . \quad . \quad . \quad . \quad (23)$$

and

$$\left.\begin{aligned} A_{11}' &= -Y_{11}'+(T-t)(Y_{24}'+Z_{22}')+(T-t)^2 Z_{24}', \\ A_{12}' &= -Y_{12}'-(T-t)(Y_{14}'+Z_{12}')-(T-t)^2 Z_{14}', \\ A_{21}' &= -Y_{21}'-(T-t)(Y_{23}'+Z_{21}')-(T-t)^2 Z_{23}', \\ A_{22}' &= -Y_{22}'+(T-t)(Y_{13}'+Z_{11}')+(T-t)^2 Z_{13}', \\ B_{11}' &= Y_{13}'+Y_{24}'+Z_{22}'+(T-t)Z_{24}', \\ B_{12}' &= -Z_{12}'-(T-t)Z_{14}', \\ B_{21}' &= -Z_{21}'-(T-t)Z_{23}', \\ B_{22}' &= Y_{13}'+Y_{24}'+Z_{11}'+(T-t)Z_{13}'. \end{aligned}\right\} \quad . \quad . \quad (24)$$

At "all-burnt," suppose that

$$\left.\begin{aligned} q_i &= Q_i+\varepsilon Q_i'+O(\varepsilon^2), \\ \dot{q}_i &= \dot{Q}_i+\varepsilon \dot{Q}_i'+O(\varepsilon^2), \end{aligned}\right\} \quad . \quad . \quad . \quad . \quad . \quad (25)$$

Then, from equation (3), it will be found that the optimum thrust direction programme is determined by the equation

$$\frac{l_1}{l_2} = \frac{L_1 + \varepsilon L_1' + O(\varepsilon^2)}{L_2 + \varepsilon L_2' + O(\varepsilon^2)} = \frac{N_1 + \varepsilon N_1' + O(\varepsilon^2)}{N_2 + \varepsilon N_2' + O(\varepsilon^2)} \quad . \quad . \quad . \quad . \quad (26)$$

where $$N_i = \frac{\partial R}{\partial Q_j} A_{ji} + \frac{\partial R}{\partial \dot{Q}_j} B_{ji}. \quad . \quad . \quad . \quad . \quad . \quad (27)$$

$$\left.\begin{aligned} N_i' = \frac{\partial R}{\partial Q_j} A_{ji}' + \frac{\partial R}{\partial \dot{Q}_j} B_{ji}' + A_{ji}\left(\frac{\partial^2 R}{\partial Q_j \partial Q_k} Q_k' + \frac{\partial^2 R}{\partial Q_j \partial \dot{Q}_k} \dot{Q}_k'\right) + \\ + B_{ji}\left(\frac{\partial^2 R}{\partial \dot{Q}_j \partial Q_k} Q_k' + \frac{\partial^2 R}{\partial \dot{Q}_j \partial \dot{Q}_k} \dot{Q}_k'\right) - \frac{1}{f} \frac{\partial F_j'}{\partial L_i} N_j. \end{aligned}\right\} \quad . \quad . \quad . \quad (28)$$

The quantities Q_i, $\dot{Q}_i$ specify the missile position and velocity at "all-burnt" in the absence of an atmosphere and can therefore be found without difficulty. Accordingly, the quantities N_i' can be computed as linear forms in the unknowns Q_k', $\dot{Q}_k'$ from the equations (28).

Multiplying across in equation (26) and equating coefficients of like powers of ε from the two members of the resulting equation, it will be found that

$$L_1 N_2 = L_2 N_1, \quad . \quad . \quad . \quad . \quad . \quad . \quad (29)$$

$$L_1' N_2 + L_1 N_2' = L_2' N_1 + L_2 N_1'. \quad . \quad . \quad . \quad . \quad (30)$$

But $l_1^2 + l_2^2 = 1$ identically, and hence

$$L_1^2 + L_2^2 = 1, \quad . \quad . \quad . \quad . \quad . \quad . \quad (31)$$

$$L_1 L_1' + L_2 L_2' = 0. \quad . \quad . \quad . \quad . \quad . \quad (32)$$

Equations (29) and (31) now imply that

$$L_1 = N_1/(N_1^2 + N_2^2)^{1/2}, \qquad L_2 = N_2/(N_1^2 + N_2^2)^{1/2}, \quad . \quad . \quad (33)$$

and equations (30) and (32) that

$$L_1' = \frac{N_2(N_2 N_1' - N_1 N_2')}{(N_1^2 + N_2^2)^{3/2}}, \qquad L_2' = \frac{N_1(N_1 N_2' - N_2 N_1')}{(N_1^2 + N_2^2)^{3/2}}. \quad . \quad (34)$$

Equations (34) determine the L_i' as linear expressions in the quantities Q_k', $\dot{Q}_k'$. Substituting these expressions in the right hand members of equations (14), the quantities $\ddot{X}_i'$ are also given as linear expressions in these unknowns. Integration of $\ddot{X}_i'$ with respect to t over the interval $(0, T)$ yields $\dot{Q}_i'$, and a second integration

over the same interval yields Q_i'. Thus, the quantities Q_i', $\dot{Q}_i'$ can be expressed linearly in terms of themselves, thus providing four simultaneous equations from which their values can be computed.

The N_i' are now completely determined and the thrust direction programme can be found to $O(\varepsilon)$.

4. Application of the Theory to a V.2-type Missile

The theory of the previous sections will now be applied to the case of a missile having aerodynamic characteristics approximating to those of the V.2 missile. Since, for such a missile, the aerodynamic forces are not small by comparison with the weight, it will be supposed that they are reduced by a factor ε by, for example, supposing the atmospheric density reduced by the same factor. An equivalent assumption would be that the thrust and weight forces are increased by a factor $1/\varepsilon$. The effect on the thrust due to the difference between jet and atmospheric pressures at the venturi exit will be neglected. Units will be the usual absolute units of the f.p.s. system (*i.e.* forces will be expressed in poundals) unless otherwise stated.

It will be assumed that the aerodynamic forces acting upon the missile can be resolved into a drag component D acting in a direction opposite to that of the motion and a lift component L acting in the upwards sense and perpendicular to D. Then, if θ is the angle made by the direction of motion with the x_1-axis,

$$\left.\begin{aligned} F_1 &= (D\cos\theta + L\sin\theta)/M, \\ F_2 &= (D\sin\theta - L\cos\theta)/M, \end{aligned}\right\} \quad . \quad . \quad . \quad . \quad (35)$$

$$\text{and} \qquad \tan\theta = \dot{x}_2/\dot{x}_1, \quad . \quad . \quad . \quad . \quad . \quad (36)$$

If v is the rocket velocity, so that

$$v = (\dot{x}_1^2 + \dot{x}_2^2)^{1/2}, \quad . \quad . \quad . \quad . \quad . \quad (37)$$

ρ is the atmospheric density and ρ_0 is the density at sea level, the drag will be supposed given by

$$D = 0{\cdot}15\,\frac{\rho}{\rho_0}\,v^2. \quad . \quad . \quad . \quad . \quad (38)$$

Assuming a steady temperature lapse rate of 2°C per 1,000 ft. and taking the launcher to be at sea level, then

$$\frac{\rho}{\rho_0} = (1 - 7x_2 \times 10^{-6})^{4{\cdot}26}. \quad . \quad . \quad . \quad . \quad (39)$$

If ϕ is the angle made by the rocket axis with the horizontal, so that

$$\cos\phi = l_1, \qquad \sin\phi = l_2, \quad . \quad . \quad . \quad . \quad . \quad (40)$$

then $\delta = \phi - \theta$ (radians) is the angle of yaw. The lift will be supposed determined by the formula

$$L = 6{\cdot}28\,\frac{\rho}{\rho_0}\,v^2\delta. \quad . \quad . \quad . \quad . \quad . \quad (41)$$

Taking the initial mass of the missile as 28,500 lb. and the rate of propellant expenditure as 275 lb./sec., the rocket mass at time t is given by

$$M = 28{,}500 - 275t. \quad . \quad . \quad . \quad . \quad . \quad (42)$$

Also, if the motor thrust is taken to be 60,000 lb. wt., then, with $g = 32{\cdot}2$,

$$f = 1{\cdot}932 \times 10^6 / M. \quad . \quad . \quad . \quad . \quad . \quad (43)$$

Equations (35), together with equations (36)-(41), now determine the F_i as functions of the quantities x_i, $\dot{x}_i$, l_i, M, t. The partial derivatives of the F_i with respect to the first six of these variables are:—

$$\left.\begin{aligned}
&\frac{\partial F_1}{\partial x_1} = \frac{\partial F_2}{\partial x_1} = 0,\\
&\frac{1}{F_1}\frac{\partial F_1}{\partial x_2} = \frac{1}{F_2}\frac{\partial F_2}{\partial x_2} = -2{\cdot}982 \times 10^{-5}/(1 - 7x_2 \times 10^{-6}),\\
&\frac{\partial F_1}{\partial \dot{x}_1} = \left[(3+\cos 2\theta)\,D + L\sin 2\theta + \frac{L}{\delta}(1-\cos 2\theta)\right]/(2Mv),\\
&\frac{\partial F_2}{\partial \dot{x}_1} = \left[D\sin 2\theta - L\,(3+\cos 2\theta) - \frac{L}{\delta}\sin 2\theta\right]/(2Mv),\\
&\frac{\partial F_1}{\partial \dot{x}_2} = \left[D\sin 2\theta + L\,(3-\cos 2\theta) - \frac{L}{\delta}\sin 2\theta\right]/(2Mv),\\
&\frac{\partial F_2}{\partial \dot{x}_2} = \left[D\,(3-\cos 2\theta) - L\sin 2\theta + \frac{L}{\delta}(1+\cos 2\theta)\right]/(2Mv),\\
&\frac{1}{f}\frac{\partial F_1}{\partial l_1} = -0{\cdot}3918 \times 10^{-6}\,\frac{L}{\delta}\sin\theta,\\
&\frac{1}{f}\frac{\partial F_1}{\partial l_2} = 0{\cdot}3382 \times 10^{-6}\,\frac{L}{\delta}\sin\theta,\\
&\frac{1}{f}\frac{\partial F_2}{\partial l_1} = 0{\cdot}3918 \times 10^{-6}\,\frac{L}{\delta}\cos\theta,\\
&\frac{1}{f}\frac{\partial F_2}{\partial l_2} = -0{\cdot}3382 \times 10^{-6}\,\frac{L}{\delta}\cos\theta
\end{aligned}\right\} \quad . \quad (44)$$

A thrust duration of $T=70$ sec. was assumed. After the cessation of motor thrust, the effect of the aerodynamic forces upon the subsequent motion of the missile was neglected. Thus the horizontal range of the missile from "all-burnt" can be calculated from the *in vacuo* formula

$$\frac{\dot{q}_1}{g}\{\dot{q}_2+\sqrt{(\dot{q}_2^2+2gq_2)}\}.$$

The net range is then given by

$$R=q_1+\frac{\dot{q}_1}{g}\left\{\dot{q}_2+\sqrt{(\dot{q}_2^2+2gq_2)}\right\}. \quad . \quad . \quad . \quad (45)$$

The optimum trajectory for the missile in the absence of aerodynamic forces has been calculated in Ref. 1. In this case, the direction of thrust is constant and

$$\phi=49^\circ\ 12'. \quad . \quad . \quad . \quad . \quad . \quad . \quad (46)$$

The values of the partial derivatives (44) at points along this trajectory were computed (five-second intervals) and, by a process of numerical integration, the values of the quantities Y_{ik}', Z_{ik}' were found at these same points from equations (17) and initial conditions (20).

Substitution in equations (24) now provided tables of values of the A_{ij}', B_{ij}'.

The conditions at "all-burnt" on the optimum trajectory in the absence of aerodynamic forces were taken from Ref. 1 to be as follows:—

$$\left.\begin{aligned} Q_1&=147{,}700, & Q_2&=92{,}250,\\ \dot{Q}_1&=5{,}171. & \dot{Q}_2&=3{,}737. \end{aligned}\right\} \quad . \quad . \quad . \quad . \quad (47)$$

The numerical values of the partial derivatives $\partial R/\partial Q_i$, $\partial^2 R/\partial Q_i\partial Q_j$, and so on, were then computed and the quantities N_i, N_i' tabulated from the equations (27) and (28). Tables of values of the L_i' now followed from equations (34) and a further four numerical integrations of the equations (14) resulted in simultaneous equations for the unknowns Q_i', $\dot{Q}_i'$, as explained in the previous section. The solution of these equations proved to be

$$\left.\begin{aligned} Q_1'&=882{,}000, & Q_2'&=-618{,}000,\\ \dot{Q}_1'&=6{,}850. & \dot{Q}_2'&=-930. \end{aligned}\right\} \quad . \quad . \quad . \quad (48)$$

The functions X_i' were now tabulated, thus determining, to the first order in ε, the effect on the optimum trajectory of the aerodynamic forces. The optimum trajectory in the absence of these forces is shown, drawn to scale, in Fig. 1 as the curve A. Taking $\varepsilon=0{\cdot}05$, the optimum trajectory in the presence of these forces

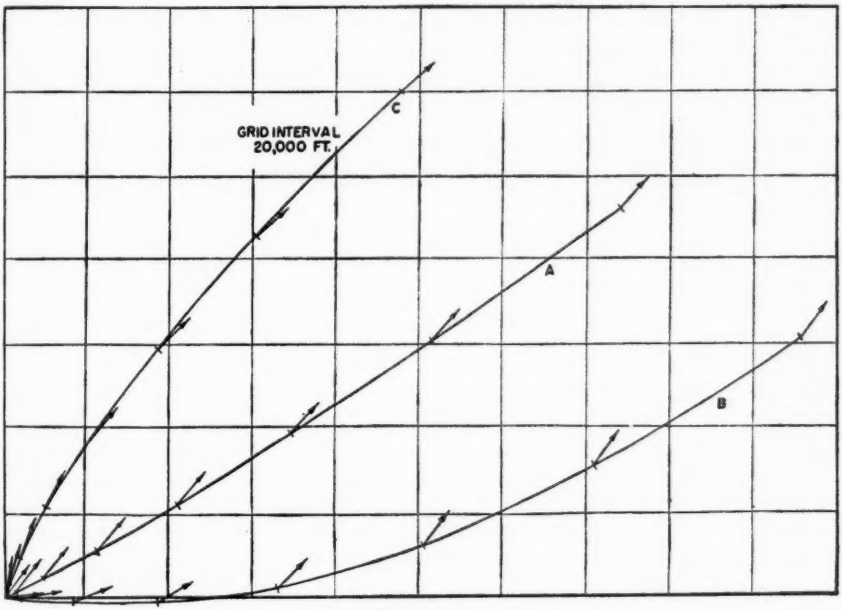

FIGURE 1.

is shown, to the same scale, as the curve B. With such a large value for ε, it is probable that second-order effects are significant, but this value has been taken with the object of magnifying the divergence from the *in vacuo* trajectory, in order that its nature will be clear from the figure. The direction of thrust (and hence of the rocket axis) is indicated by arrows at 10-second intervals.

It will be observed that the early portion of the track B is approximately horizontal (in fact, it dips below the earth's surface initially, although, of course, this cannot correspond to a practicable trajectory). During this time, the missile gathers momentum and its angle of yaw increases to provide a steadily increasing lift force, by means of which it eventually gains altitude. During the latter stages of the motion, the angle of yaw is decreased. Thus, broadly speaking, the lift assists in the generation of the vertical momentum permitting the rocket thrust to be employed primarily in the generation of the horizontal momentum. Under normal atmospheric conditions it may be expected that, for the optimum trajectory, the lift will be responsible for the greater part of the vertical momentum.

The manner of variation of the angles ϕ and δ with the time is shown graphically in Fig. 2.

The increase in range, beyond that attained in the absence of the aerodynamic forces is given by

$$R=\varepsilon\left(\frac{\partial R}{\partial Q_i}Q_i'+\frac{\partial R}{\partial \dot{Q}_i}\dot{Q}_i'\right)=1{\cdot}64\varepsilon\times 10^6. \quad . \quad . \quad . \quad (49)$$

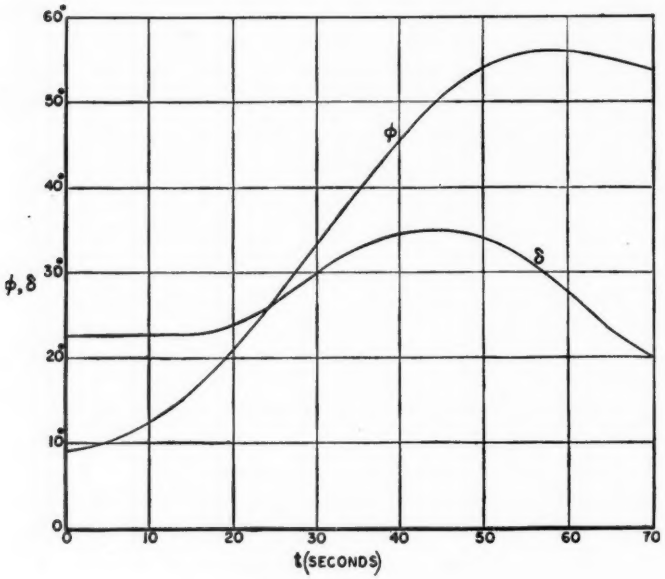

FIGURE 2.

It is interesting to observe that the range increment is positive and, with $\varepsilon = 0{\cdot}05$, amounts to about 16 miles. If, however, the action of air resistance during the ballistic phase is taken into account, the apparent increment may well be converted into a decrement. Nevertheless, it is clear that, by appropriate choice of the thrust direction programme, the adverse effect of drag upon the range can be offset, to a large extent, by a compensating effect provided by the lift.

As a check upon the validity of these conclusions, the whole problem was recomputed, neglecting the lift force. The optimum trajectory for a V.2-type missile subject to drag alone was therefore found. The following values were obtained for the quantities Q_i', $\dot{Q}_i'$,

$$\left.\begin{aligned} Q_1' &= -104{,}700, & Q_2' &= 53{,}800, \\ \dot{Q}_1' &= -2{,}050, & \dot{Q}_2' &= 240. \end{aligned}\right\} \quad . \quad . \quad . \quad (50)$$

With these values, it will be found that

$$\delta R = -4{\cdot}9\varepsilon \times 10^5, \quad . \quad . \quad . \quad . \quad . \quad (51)$$

i.e. there is a range decrement which amounts to about 5 miles when $\varepsilon = 0{\cdot}05$.

The optimum trajectory for this missile (with $\varepsilon = 0{\cdot}5$) is shown as curve C in Fig. 1. In this case, no advantage is to be derived by remaining in the lower strata of the atmosphere. Thus, the thrust is now employed to gain altitude fairly rapidly, in order that advantage may be taken of the lower atmospheric density, and consequent lower drag, at the greater heights during the phase of acceleration towards maximum velocity. The thrust direction is again shown by arrows at 10-second intervals.

Acknowledgments

The author is indebted to the Senate of the University of New Zealand for a grant in aid of the research reported in this paper.

He also wishes to express his thanks to Mr. D. G. King-Hele of the Royal Aircraft Establishment for the provision of the numerical data upon which the formulae for the drag and lift forces acting upon a V.2-type missile given in Section 4 of the paper are based. However, Mr. King-Hele is to be absolved from responsibility for the somewhat crude formulae which have been fitted to his data for the purpose of simplifying the numerical computations with which the author was faced.

References

1. Lawden, D. F. Dynamic Problems of Interplanetary Flight. *The Aeronautical Quarterly*, Vol. VI, pp. 165-180, August 1955.

2. Lawden, D. F. Maximum Ranges of Intercontinental Missiles. *The Aeronautical Quarterly*, Vol. VIII, pp. 269-278, August 1957.

The Compressible Flow Through Cascade Actuator Discs

J. H. HORLOCK

(University Engineering Laboratory, Cambridge)

SUMMARY: A theory of the incompressible flow through two- and three-dimensional cascade actuator discs has been developed by several workers over the past ten years, and its accuracy has been confirmed in several experiments. This theory is briefly reviewed, and a parallel theory for subsonic compressible flow through actuator discs is developed. Approximate solutions for several examples are considered, including a compressible shear flow through a two-dimensional cascade, and a compressible flow through an annular cascade of guide vanes.

1. A Review of Incompressible Flow Through Cascade Actuator Discs

1.1. INTRODUCTION

The incompressible flow through cascade actuator discs has been studied by several authors[1]-[6]. A brief review of approximate solutions to the two- and three-dimensional problems is given here, to provide a basis for comparison with the compressible solutions derived later.

Referring to Fig. 1, a co-ordinate system x, y, z is considered, with velocities u, v, w and vorticities ξ, η, ζ.

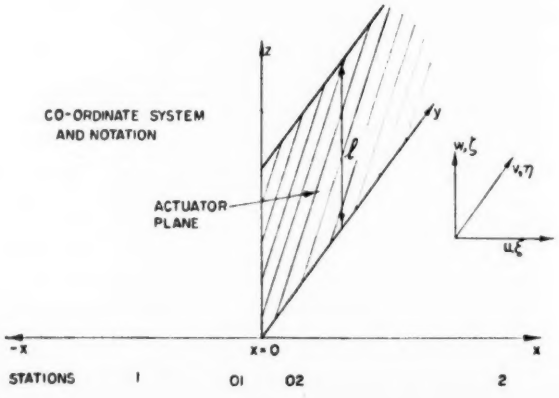

FIGURE 1. The two-dimensional problem.

Received July 1957.

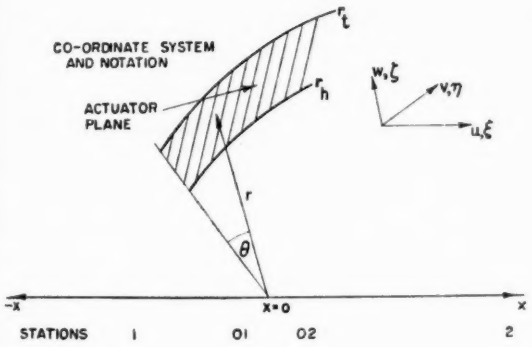

FIGURE 2. The three-dimensional problem.

A cascade actuator disc made up of an infinite number of blades each of very small axial length, is located at $x=0$. The flow from a station (1), far upstream, to a station (2), far downstream, is considered. At both (1) and (2) the static pressures will be constant. The cascade acuator disc will provide a discontinuity in tangential velocity v and vorticity η, but there is no change in axial velocity and radial velocity across the disc. Since there are many blades, all derivatives in the y-direction vanish.

Ruden[7] originally made the two assumptions that the tangential velocity and vorticity changed little in the x-direction (*i.e.* $v,\ \eta=f(z)$) for a "small perturbation" flow. Hawthorne and Armstrong[8] (for two-dimensional cascades) have shown that these two assumptions are valid if $w/u,\ \eta,\ \partial\eta/\partial z,\ \partial v/\partial z$ are always small. In three-dimensional flow (*see* Fig. 2), these conditions become that $w/u,\ \eta,\ \partial\eta/\partial r,\ \partial(rv)/\partial r$ should be small[2].

Further, if the tangential vorticity is constant along lines of constant z or r, then a consideration of the axial velocity fields induced by the η-component of vorticity leads to the conclusion that in incompressible flow the axial velocity at the disc is the mean of the axial velocities (at the same z or r) far upstream and far downstream. In the notation of Figs. 1 and 2,

$$u_{01}=u_{02}=\tfrac{1}{2}(u_1+u_2).$$

These assumptions were found to be reasonable in an exact analysis for two particular examples considered by Bragg and Hawthorne[5].

NOTATION

x, y, z	co-ordinates	
u, v, w	velocities in x, y, z co-ordinate system	two-dimensional flow
ξ, η, ζ	vorticities in x, y, z co-ordinate system	

l length of actuator disc in z-direction

A_i, B_i, k_i constants

x, θ, r co-ordinates

u, v, w velocities in x, θ, r co-ordinate system } three-dimensional flow

ξ, η, ζ vorticities in x, θ, r co-ordinate system }

H stagnation enthalpy

α air angle

ρ density

p static pressure

a speed of sound

M_x axial component of Mach number

$\lambda = \sqrt{(1 - M_{x\infty}^2)}$

A area

$\chi = \frac{1}{2}(u_2 - u_{2m}) - \frac{1}{2}(u_1 - u_{1m})$

M_θ tangential component of Mach number

$$\lambda_x = \frac{1 - M_{x\infty}^2}{1 + M_{\theta\infty}^2}$$

$$\lambda_\theta = \frac{1}{1 + M_{\theta\infty}^2}$$

$q = \sqrt{(u^2 + v^2)}$

W flow rate

Subscripts

1 axial location far upstream of an actuator disc

2 axial location far downstream of an actuator disc

01 axial location immediately upstream of an actuator disc

02 axial location immediately downstream of an actuator disc

∞ axial location far upstream or downstream of an actuator disc

t tip

h hub

m mean

Superscripts

$'$ perturbation

$*$ relating to conditions where $M = 1$ (in Tables IV, V and VI).

1.2. Analysis for Two-Dimensional Incompressible Flow

The continuity equation for two-dimensional incompressible flow is

$$\frac{\partial u}{\partial x}+\frac{\partial v}{\partial y}+\frac{\partial w}{\partial z}=0, \qquad (1)$$

and, as derivatives with respect to y must vanish,

$$\frac{\partial u}{\partial x}+\frac{\partial \varrho}{\partial z}=0. \qquad (1a)$$

If the velocity u is made up of the velocity $u_\infty(z)$ at the location far away from the disc and a small perturbation u' ($u=u_\infty+u'$), then equation (1*a*) becomes

$$\frac{\partial u'}{\partial x}+\frac{\partial w}{\partial z}=0, \qquad (1b)$$

where u' and w are both small compared with u_∞.

The Ruden assumption for the vorticity,

$$\eta=\eta_\infty(z),$$

may be written $\dfrac{\partial u_\infty}{\partial z}+\dfrac{\partial u'}{\partial z}-\dfrac{\partial w}{\partial x}=\dfrac{\partial u_\infty}{\partial z}$,

or

$$\frac{\partial u'}{\partial z}=\frac{\partial w}{\partial x}. \qquad (2)$$

From equations (1) and (2),

$$\frac{\partial^2 w}{\partial x^2}+\frac{\partial^2 w}{\partial z^2}=0, \qquad (3)$$

a solution of which is

$$w=\sum_i e^{\pm k_i x}[A_i \sin k_i z+B_i \cos k_i z]. \qquad (4)$$

The boundary conditions for this equation are that w should vanish:—

(*i*) at the side walls ($z=0, l$).

(*ii*) far upstream of the disc (for the flow upstream).

(*iii*) far downstream of the disc (for the flow downstream).

With these restrictions

$$\left.\begin{aligned} w &= \sum_{n=1,2,3,\ldots} A_{nu} \sin(n\pi z/l)\, e^{n\pi x/l} \quad \text{upstream,} \\ w &= \sum_{n=1,2,3,\ldots} A_{nd} \sin(n\pi z/l)\, e^{-n\pi x/l} \quad \text{downstream.} \end{aligned}\right\} \quad . \quad . \quad (5)$$

Integrating (1*a*) with respect to x, from infinity to x, gives the solution for u',

$$\left.\begin{aligned} u' &= -\sum A_{nu} \cos(n\pi z/l)\, e^{n\pi x/l} \quad \text{upstream,} \\ u' &= +\sum A_{nd} \cos(n\pi z/l)\, e^{-n\pi x/l} \quad \text{downstream.} \end{aligned}\right\} \quad . \quad . \quad (6)$$

The second Ruden assumption, that $u_{01}=u_{02}=\frac{1}{2}(u_1+u_2)$, provides a boundary condition for u' at the disc

$$\left.\begin{aligned} u_{01}' &= \tfrac{1}{2}(u_2-u_1) = -\sum A_{nu} \cos(n\pi z/l), \\ u_{02}' &= -\tfrac{1}{2}(u_2-u_1) = +\sum A_{nd} \cos(n\pi z/l). \end{aligned}\right\} \quad . \quad . \quad . \quad (7)$$

If the distribution of u_2 and u_1 with z is known, then the coefficients A_n may be obtained from a Fourier analysis. For most cases met in turbo-machines, since $\frac{1}{2}(u_2-u_1)$ will be approximately zero at $z=l/2$, and approximately as much positive at one wall as negative at the other, the first Fourier coefficient is much larger than the later terms. For a linear variation of $\frac{1}{2}(u_2-u_1)$ with z, for example, the second term is one ninth of the first, and decays at the rate $e^{-3\pi x/l}$ away from the disc. Thus a solution using the first term only will be sufficient for most practical purposes and

$$\left.\begin{aligned} u' &\simeq \tfrac{1}{2}(u_2-u_1)\, e^{\pi x/l} \quad \text{upstream,} \\ u' &\simeq -\tfrac{1}{2}(u_2-u_1)\, e^{-\pi x/l} \quad \text{downstream.} \end{aligned}\right\} \quad . \quad . \quad . \quad (8)$$

This solution is exact if $\frac{1}{2}(u_2-u_1)=A_1 \cos(\pi z/l)$.

1.3. Analysis for Three-Dimensional Incompressible Flow

In three-dimensional flow, equations corresponding to equations (1*b*), (2), (3), (4), are

$$\frac{\partial}{\partial x}(ru') + \frac{\partial}{\partial r}(rw) = 0, \quad . \quad . \quad . \quad . \quad . \quad (9)$$

$$\frac{\partial u'}{\partial r} = \frac{\partial w}{\partial x}, \quad . \quad . \quad . \quad . \quad . \quad (10)$$

$$\frac{\partial^2 w}{\partial r^2} + \frac{1}{r}\frac{\partial w}{\partial r} - \frac{w}{r^2} + \frac{\partial^2 w}{\partial x^2} = 0, \quad . \quad . \quad . \quad . \quad (11)$$

$$w = \sum_i e^{\pm k_i x}[A_i J_1(k_i x) + B_i Y_1(k_i r)]. \quad . \quad . \quad . \quad (12)$$

The boundary conditions that $w=0$ at $r=r_h$, r_t give

$$J_1(k_i r_h)\, Y_1(k_i r_t) = J_1(k_i r_t)\, Y_1(k_i r_h), \quad . \quad . \quad . \quad . \quad (13)$$

Table I gives solutions obtained from Jahnke and Emde[13].

TABLE I

r_t/r_h	$k_1(r_t-r_h)$	$k_2(r_t-r_h)$
1·0	π	2π
1·5	3·1609	6·293
2·5	3·1966	6·312

Taking only the first term in the solution again, and using the Ruden assumption for the velocity at the disc

$$\left.\begin{aligned} u' &= \tfrac{1}{2}(u_2-u_1)\, e^{k_1 x} \quad \text{upstream,} \\ u' &= -\tfrac{1}{2}(u_2-u_1)\, e^{-k_1 x} \quad \text{downstream,} \end{aligned}\right\} \quad . \quad . \quad . \quad (14)$$

where k_1 is given in Table I, as a function of r_t/r_h.

1.4. The Direct and Indirect Problems in Incompressible Flow

So far only the indirect problem of the flow in turbo-machines has been considered—the flow in a field in which u_1, u_2 are specified far upstream and far downstream. In the direct problem the flow far upstream, and a distribution of outlet angle α_{02} at exit from the disc, may be specified (where $\tan \alpha_{02} = v_{02}/u_{02}$). It is required to find the velocity distribution far downstream and elsewhere in the field.

A solution to this problem is obtained by using the equation of motion in the r-direction (for three dimensions) in the form

$$\frac{\partial H}{\partial r} = \zeta v - \eta u, \quad . \quad . \quad . \quad . \quad . \quad (15)$$

where H is the stagnation enthalpy and

$$\zeta = \frac{1}{r}\frac{\partial}{\partial r}(rv).$$

For a stationary guide vane row, for example, accepting a uniform axial velocity profile far upstream, $H_{01}=H_{02}$,

$$\text{and} \qquad \frac{\partial H_{01}}{\partial r} = \frac{\partial H_{02}}{\partial r} = 0,$$

$$\frac{v_{02}}{r}\frac{\partial}{\partial r}(rv_{02}) - u_{02}\eta_{02} = 0.$$

Since $$\eta_{02}=\eta_2=-\frac{\partial u_2}{\partial r}=-\frac{du_2}{dr},$$

$$\frac{\partial u_2}{\partial r}+\frac{v_{02}}{ru_{02}}\frac{\partial}{\partial r}(rv_{02})=0.$$

But $$v_{02}=u_{02}\tan\alpha_{02}$$

and $$\frac{\partial u_2}{\partial r}+\frac{\tan\alpha_{02}}{r}\frac{\partial}{\partial r}(ru_{02}\tan\alpha_{02})=0.$$

For the particular case in which $\tan\alpha_{02}=$constant, using the Ruden expression for u_{02},

$$\frac{du_2}{dr}\left(1+\frac{\tan^2\alpha_{02}}{2}\right)+\frac{u_2\tan^2\alpha_{02}}{2r}=0,$$

and $$u_2 r^{\tan^2\alpha_{02}/(2+\tan^2\alpha_{02})}=\text{constant}. \quad . \quad . \quad . \quad . \quad . \quad (16)$$

It is of interest to note that the solution to this problem based on a "radial equilibrium" approach[9], by assuming there is no radial velocity at exit from the blades (*i.e.* that station (2) is at the trailing edge of the blade row where the angle distribution α_2 is constant), would give

$$\frac{\partial H_2}{\partial r}=\frac{v_2}{r}\frac{\partial}{\partial r}(rv_2)+u_2\frac{\partial u_2}{\partial r}=0,$$

and $$ur^{\sin^2\alpha_2}=\text{constant}. \quad . \quad . \quad . \quad . \quad . \quad . \quad . \quad (17)$$

Considering the flow through a set of guide vanes where the exit angle is 45° and $r_h/r_t=0{\cdot}4$, equations (16) and (17) become

$$u_2 r^{1/3}=\text{constant}, \quad . \quad . \quad . \quad . \quad . \quad (16a)$$

$$u_2 r^{1/2}=\text{constant}. \quad . \quad . \quad . \quad . \quad . \quad (17a)$$

Table II shows a comparison of root and tip axial velocities obtained from these two solutions.

TABLE II

	u_1	u_2 from (16*a*)	$u_2=u_{02}$ from (17*a*)	u_{02} from (16*a*)
$r_h=0{\cdot}4$	100	120·5	131·8	110·2
$r_t=1{\cdot}0$	100	88·5	83·2	94·2

To illustrate the indirect problem of specifying an angle distribution to produce a particular velocity distribution, the design of a guide vane row to produce a constant tangential velocity distribution v_2 may be considered.

Far downstream the axial velocity distribution is obtained from equation (15),

$$u_2 \frac{du_2}{dr} + \frac{v_2}{r} \frac{d}{dr}(rv_2) = 0,$$

$$\text{and} \qquad u_2 = \sqrt{(A - 2v_2^2 \log r)}, \qquad . \quad . \quad . \quad . \quad (18)$$

where A and v_2 are constants.

The angle distribution at a cascade actuator plane where the axial velocity is $\frac{1}{2}(u_1 + u_2)$ would be

$$\tan \alpha_{a2} = \frac{2v_{a2}}{u_1 + u_2} = \frac{2v^2}{u_1 + \sqrt{(A - 2v_2^2 \log r)}}, \qquad . \quad . \quad (19)$$

but the angle distribution at the trailing edge of a blade where the flow is in radial equilibrium would be

$$\tan \alpha_2 = \frac{v_2}{\sqrt{(A - 2v_2^2 \log r)}}. \qquad . \quad . \quad . \quad . \quad (20)$$

A comparison for a guide vane row producing a tangential velocity v_2 equal to the axial velocity u_1, far upstream, is given in Table III.

TABLE III

	u_1	u_2	v_2	α_2 from (20)	α_{a2} from (19)
$r_h = 0{\cdot}4$	100	146	100	34·4	39·1
$r_t = 1{\cdot}0$	100	53	100	62·05	52·55

1.5. Experimental Work in Incompressible Flow

Several experiments, on two-dimensional cascades and axial flow compressors have been made[8, 10], all at low speeds. These results confirm the accuracy of the analysis given in the previous section. For example, Figs. 3 and 4 show axial velocity profiles observed far upstream, at the leading edge, at the trailing edge, and far downstream of a single stator (Fig. 3) and a single rotor (Fig. 4). The exponential decay in axial velocity up to and away from the blade row is clearly seen in each case, and the velocities are compared with calculations made from the analysis outlined in the previous section, using cascade data to give the outlet angle distribution. In each case, for the purposes of calculation, the actuator disc was supposed to be located on the axial centre line of the blade row.

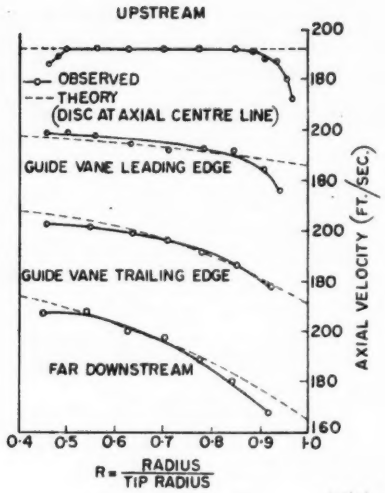

FIGURE 3. Stationary row.

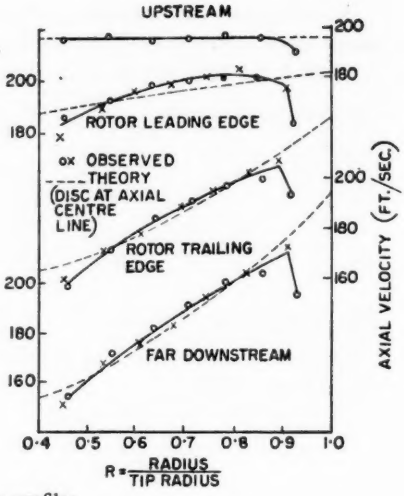

FIGURE 4. Rotating row.

Axial velocity profiles.

2. Compressible Flow

2.1. Analysis for Two-Dimensional Compressible Flow

A similar approach may be made to the problem of compressible flow through the two-dimensional system of Fig. 1.

The continuity equation is

$$\frac{\partial}{\partial x}(\rho u)+\frac{\partial}{\partial y}(\rho v)+\frac{\partial}{\partial z}(\rho w)=0, \qquad (21)$$

but, since the y derivatives vanish,

$$\frac{\partial}{\partial x}(\rho u)+\frac{\partial}{\partial z}(\rho w)=0. \qquad (21b)$$

The Euler equations of motion are

$$-\frac{1}{\rho}\frac{\partial p}{\partial x}=u\frac{\partial u}{\partial z}+v\frac{\partial u}{\partial y}+w\frac{\partial u}{\partial z}, \qquad (22)$$

$$-\frac{1}{\rho}\frac{\partial p}{\partial y}=u\frac{\partial v}{\partial x}+v\frac{\partial v}{\partial y}+w\frac{\partial v}{\partial z}, \qquad (23)$$

$$-\frac{1}{\rho}\frac{\partial p}{\partial z}=u\frac{\partial w}{\partial x}+v\frac{\partial w}{\partial y}+w\frac{\partial w}{\partial z}. \qquad (24)$$

Noting that the y derivatives again vanish, and that the velocity of sound $a=\sqrt{\{(dp/d\rho)_s\}}$, these equations may be rewritten

$$-\frac{a^2}{\rho}\frac{\partial \rho}{\partial x}=u\frac{\partial u}{\partial x}+w\frac{\partial u}{\partial z}, \qquad (22a)$$

$$0=u\frac{\partial v}{\partial x}+w\frac{\partial v}{\partial z}, \qquad (23a)$$

$$-\frac{a^2}{\rho}\frac{\partial \rho}{\partial z}=u\frac{\partial w}{\partial x}+w\frac{\partial w}{\partial z}. \qquad (24a)$$

Substituting in equation (21b) from equations (22a) and (24a),

$$\frac{\partial u}{\partial x}\left(1-\frac{u^2}{a^2}\right)+\frac{\partial w}{\partial z}\left(1-\frac{w^2}{a^2}\right)-\frac{uw}{a^2}\left(\frac{\partial u}{\partial z}+\frac{\partial w}{\partial x}\right)=0. \qquad (25)$$

If small perturbations from the flow at $\pm\infty$ are considered, then $u=u_\infty(z)+u'$, and u'/u_∞, w/u_∞ are both small. Further, if another of the assumptions of the incompressible analysis is made, that η_∞ is always small, then terms such as $\partial u/\partial z$, $\partial w/\partial x$ are small, and equation (25) becomes

$$\frac{\partial u'}{\partial x}\left(1-M_x^2\right)+\frac{\partial w}{\partial z}=0, \qquad (26)$$

where $M_x=u/a$ is the axial component of the Mach number of the flow.

The variation of v with x is seen to be of second order, from the second Euler equation, for $\partial v/\partial x=-(w/u)\,\partial v/\partial z$, and both w/u and $\partial v/\partial z$ are small.

The variation of η with x may also be shown to be of second order. The second Helmholtz equation may be written

$$u\frac{\partial \eta}{\partial x}+w\frac{\partial \eta}{\partial z}=\xi\frac{\partial v}{\partial x}+\zeta\frac{\partial v}{\partial z}-\eta\left(\frac{\partial u}{\partial x}+\frac{\partial w}{\partial z}\right). \qquad (27)$$

But $\xi=-\partial v/\partial z$ and $\zeta=\partial v/\partial x$, and equation (27) becomes

$$\frac{\partial \eta}{\partial x}=-\frac{w}{u}\frac{\partial \eta}{\partial z}-\frac{\eta}{u}\left(\frac{\partial u'}{\partial x}+\frac{\partial w}{\partial z}\right). \qquad (27a)$$

Since both η and $\partial\eta/\partial z$ are small, the variation of η with x may be neglected.

Using this result, $\eta_\infty=\eta$,

and $$\frac{\partial u_\infty}{\partial z}+\frac{\partial u'}{\partial z}-\frac{\partial w}{\partial x}=\frac{\partial u_\infty}{\partial z},$$

$$\frac{\partial u'}{\partial z}=\frac{\partial w}{\partial x}. \qquad (29)$$

From equations (26) and (29), the equation

$$\frac{\partial^2 w}{\partial x^2}(1-M_x^2)-2M_x\frac{\partial u'}{\partial x}\frac{\partial M_x}{\partial z}+\frac{\partial^2 w}{\partial z^2}=0 \qquad . \quad . \quad (30)$$

is obtained.

Writing the axial Mach number

$$M_x=M_{x\infty}(z)+M_x',$$

equation (30) becomes

$$\frac{\partial^2 w}{\partial x^2}(1-M_{x\infty}{}^2-2M_{x\infty}M_x')+2\frac{\partial u'}{\partial x}M_{x\infty}\frac{\partial M_x}{\partial z}+\frac{\partial^2 w}{\partial z^2}=0. \qquad . \quad (30a)$$

Since $\eta=\partial u_\infty/\partial z$ is small, $\partial u'/\partial x$ and $\partial M_x/\partial z$ will be small, and equation (30*a*) may be written

$$\frac{\partial^2 w}{\partial x^2}(1-M_{x\infty}{}^2)+\frac{\partial^2 w}{\partial z^2}=0. \qquad . \quad . \quad . \quad . \quad (30b)$$

A solution of this equation is

$$w=\sum_1^\infty e^{\pm k_n x}\left[A_n \sin\{k_n\sqrt{(1-M_{x\infty}{}^2)}\}\,z+B_n\cos\{k_n\sqrt{(1-M_{x\infty}{}^2)}\}z\right].$$

With the boundary conditions $w=0$ at $z=0, l$,

$$B_n=0, \qquad k_n=\frac{n\pi}{\lambda l},$$

where $\lambda=\sqrt{(1-M_{x\infty}{}^2)}$, and the solution becomes

$$\left.\begin{aligned} w&=\sum_1^\infty e^{+n\pi x/(\lambda_1 l)}A_{nu}\sin n\pi z/l \quad \text{upstream,}\\ w&=\sum_1^\infty e^{-n\pi x/(\lambda_2 l)}A_{nd}\sin(n\pi z/l) \quad \text{downstream.}\end{aligned}\right\} \quad . \quad . \quad (31)$$

Equation (26), which is $\qquad \lambda^2\dfrac{\partial u'}{\partial x}+\dfrac{\partial w}{\partial z}=0,$

may be integrated from the infinity station to x and

$$\left.\begin{aligned} u'&=-\sum e^{+n\pi x/(\lambda_1 l)}(A_{nu}/\lambda_1)\cos(n\pi z/l) \quad \text{upstream.}\\ u'&=+\sum e^{-n\pi x/(\lambda_2 l)}(A_{nd}/\lambda_2)\cos(n\pi z/l) \quad \text{downstream.}\end{aligned}\right\} \quad . \quad (32)$$

2.2. The Axial Velocity at the Disc in Compressible Flow

To find the boundary conditions on axial velocity at the disc, the Ruden assumption must be reconsidered for compressible flow.

The induced velocity due to a vortex field, $\eta_1(z)=du_1/dz$, stretching from $x=-\infty$ to $x=+\infty$ is u_1-u_{1m}, at any point x (including $x=0$) where u_{1m} is the mean axial velocity across the section from $z=0$ to l, *i.e.* $u_{1m}=(\int_0^l u_1 dz)/l$. The induced velocity at $x=0$ due to a vorticity field $\eta_1(z)=du_1/dz$, stretching from $x=-\infty$ to $x=0$ will be $\frac{1}{2}(u_1-u_{1m})$.

Similarly the induced velocity at $x=0$ due to a vortex field $\eta_2(z)=du_2/dz$, stretching from $x=0$ to $x=+\infty$ will be $\frac{1}{2}(u_2-u_{2m})$.

The total induced velocity at the disc ($x=0$) due to the combined fields $\eta_1(z)=du_1/dz$ $(-\infty<x<0)$ and $\eta_2(z)=du_2/dz$ $(0<x<\infty)$ will be $\frac{1}{2}(u_1+u_2)-\frac{1}{2}(u_{1m}+u_{2m})$.

Thus the axial velocity at station (01) is

$$u_{01}=u_{1m}+\tfrac{1}{2}(u_2+u_1)-\tfrac{1}{2}(u_{1m}+u_{2m})=\tfrac{1}{2}(u_2+u_1)+\tfrac{1}{2}(u_{1m}-u_{2m}). \quad . \quad (33)$$

and at station (02)

$$u_{02}=\tfrac{1}{2}(u_2+u_1)+\tfrac{1}{2}(u_{2m}-u_{1m}).$$

The change in axial velocity across the disc is

$$u_{02}-u_{01}=u_{2m}-u_{1m},$$

and is constant with z.

In incompressible flow $u_{01}=u_{02}$, since $u_{1m}=u_{2m}$, but in compressible flow u_{1m} will be greater or less than u_{2m} according to whether the row is a compressor or a turbine type row. The perturbation velocity at station (02) is

$$\begin{aligned} u_{01}'=u_{01}-u_1&=\tfrac{1}{2}(u_2+u_1)+\tfrac{1}{2}(u_{1m}-u_{2m})-u_1 \\ &=\tfrac{1}{2}(u_2-u_{2m})-\tfrac{1}{2}(u_1-u_{1m})=\chi. \quad . \quad . \quad . \quad (34) \end{aligned}$$

These boundary values may be used with the first term only of equation (32) to give

$$\left.\begin{aligned} u'&=\chi\, e^{\pi x/(\lambda_1 l)} \quad \text{upstream,} \\ u'&=-\chi\, e^{-\pi x/(\lambda_2 l)} \quad \text{downstream.} \end{aligned}\right\} \quad . \quad . \quad . \quad . \quad (35)$$

where $\lambda_1=\sqrt{(1-M_{x1\infty}{}^2)}$, $\lambda_2=\sqrt{(1-M_{x2\infty}{}^2)}$.

2.3. Density Variation in Compressible Flow

Writing the density $\rho = \rho_\infty(z) + \rho'$, and ignoring the cross products of small terms, equation (21*b*) becomes

$$u\frac{\partial \rho'}{\partial x} + \rho_\infty \frac{\partial u'}{\partial x} + \rho_\infty \frac{\partial w}{\partial z} + w\frac{\partial \rho_\infty}{\partial z} = 0. \quad . \quad . \quad . \quad (36)$$

For two-dimensional cascades, the pressure at the infinity station is constant, and $\partial\rho_\infty/\partial z$ will be zero if the static temperature is constant. However, even if small variations in the static temperature and density $\rho_\infty(z)$ are allowed, the last term of equation (36) is of second order of smallness, and the equation becomes

$$u_\infty \frac{\partial \rho'}{\partial x} + \rho_\infty\left(\frac{\partial u'}{\partial x} + \frac{\partial w}{\partial z}\right) = 0.$$

Substituting for $\partial u'/\partial x$ and $\partial w/\partial z$ from equations (31) and (35), and integrating from the infinity station to x,

$$\left.\begin{aligned} \rho' &= -\rho_\infty \frac{\chi}{u_1} M_1^2 \, e^{kx} \quad \text{upstream,} \\ \rho' &= +\rho_\infty \frac{\chi}{u_2} M_2^2 \, e^{-kx} \quad \text{downstream.} \end{aligned}\right\} \quad . \quad . \quad . \quad (37)$$

$$\left.\begin{aligned} \rho &= \rho_1\left(1 - \frac{\chi M_1^2}{u_1} e^{kx}\right) \text{upstream,} \\ \rho &= \rho_2\left(1 + \frac{\chi M_2^2}{u_2} e^{-kx}\right) \text{downstream.} \end{aligned}\right\} \quad . \quad . \quad . \quad (37a)$$

2.4. Examples of Two-Dimensional Compressible Flow

As one example of the compressible flow through a two-dimensional cascade, a uniform entry flow may be considered (u_1, v_1 = constant). If the cascade exit angle is also uniform, the exit velocities u_{02} and u_2 will be uniform. There will be no perturbation in axial velocity or density upstream or downstream of the disc, since $\chi = \frac{1}{2}(u_2 - u_{2m}) - \frac{1}{2}(u_1 - u_{1m}) = 0$. Solutions for u_{02} and u_2 based on actuator disc theory or "radial equilibrium" will be the same. For example if $M_1 = 0{\cdot}5$, $\alpha_1 = 0$, $\alpha_2 = 30°$, a solution may be obtained directly from gas tables[11]. Table IV (p. 126) gives such a solution, using the notation of Ref. 11.

As a second example of a two-dimensional compressible cascade flow, a linear variation of velocity and Mach number at entry to a cascade ($\alpha_1 = 0$, $\alpha_{02} = 30°$) is considered.

Writing the equations of motion in the z-direction,

$$\frac{\partial H_{02}}{\partial z} = \zeta_{02} v_{02} - \eta_{02} u_{02}$$

$$= v_{02} \frac{\partial v_{02}}{\partial z} + u_{02} \frac{\partial u_2}{\partial z}$$

$$\frac{\partial H_{01}}{\partial z} = u_{01} \frac{\partial u_1}{\partial z} ,$$

since $$\frac{\partial H_{02}}{\partial z} = \frac{\partial H_{01}}{\partial z} ,$$

it follows that

$$\frac{\partial u_2}{\partial z} [1 + \tfrac{1}{2} \tan^2 \alpha_{02}] = \frac{\partial u_1}{\partial z} \left[\frac{u_{01}}{u_{02}} - \tfrac{1}{2} \tan^2 \alpha_{02} \right]$$

and $$u_2 \simeq \frac{[2 (\rho_2/\rho_1) - \tan^2 \alpha_{02}]}{(2 + \tan^2 \alpha_{02})} u_1 + \text{constant}.$$

For the particular example,

$$\rho_2/\rho_1 \simeq 0{\cdot}936, \qquad u_2 = 0{\cdot}65 u_1 + \text{constant}. \quad . \quad . \quad . \quad (38)$$

using the solution of Table IV (p. 126) to give the density ratio ρ_2/ρ_1.

A trial and error solution gives the velocity distribution in the complete field, as in Table V (p. 126), in which the constant of equation (38) is taken as 41·1.

To check the analysis, values of u_{02} as calculated directly from $u_{02} = u_2 - \chi$ and as calculated from the density variation ρ_{02}/ρ_0 and from Ref. 11 are compared in the last two columns.

2.5. Analysis for Three-Dimensional-Compressible Flow

Equations corresponding to (21*b*), (22*a*), (23*a*) and (24*a*) in three-dimensional flow, in which the θ derivatives vanish, are

$$\frac{\partial}{\partial x} (\rho u r) + \frac{\partial}{\partial r} (\rho r w) = 0, \quad . \quad . \quad . \quad . \quad . \quad . \quad (39)$$

$$- \frac{a^2}{\rho} \frac{\partial \rho}{\partial x} = u \frac{\partial u}{\partial x} + w \frac{\partial u}{\partial r} , \quad . \quad . \quad . \quad . \quad (40)$$

$$0 = u\frac{\partial v}{\partial x} + w\frac{\partial v}{\partial r} + \frac{wv}{r} \quad . \quad . \quad . \quad . \quad (41)$$

$$-\frac{a^2}{\rho}\frac{\partial \rho}{\partial r} = w\frac{\partial w}{\partial r} + u\frac{\partial w}{\partial x} - \frac{v^2}{r} \quad . \quad . \quad . \quad (42)$$

Substituting in equation (39) from equations (40) and (42), the equation

$$\frac{\partial u}{\partial x}(1 - M_x^2) + \frac{\partial w}{\partial r}(1 - M_r^2) + \frac{w}{r}(1 + M_\theta^2) - \frac{uw}{a^2}\left(\frac{\partial u}{\partial r} + \frac{\partial w}{\partial x}\right) = 0. \quad . \quad (43)$$

is obtained.

As in the two-dimensional case, if η and $\partial\eta/\partial r$ are small then $\eta = \eta_\infty(r)$ and

$$\frac{\partial u'}{\partial r} = \frac{\partial w}{\partial x} \quad . \quad . \quad . \quad . \quad . \quad . \quad . \quad (44)$$

Also, since η is small, equation (43) becomes

$$\frac{\partial u'}{\partial x}(1 - M_x^2) + \frac{\partial w}{\partial r} + \frac{w}{r}(1 + M_\theta^2) = 0. \quad . \quad . \quad (43b)$$

Writing $\quad M_x = M_{x\infty}(r) + M_x' \quad$ and $\quad M_\theta = M_{\theta\infty}(r) + M_\theta'.$

and assuming $\partial M_{x\infty}/\partial r$, $\partial M_{\theta\infty}/\partial r$ are small, the equation

$$\lambda_x\frac{\partial^2 w}{\partial x^2} + \frac{1}{r}\frac{\partial w}{\partial r} - \frac{w}{r^2} + \lambda_\theta\frac{\partial^2 w}{\partial r^2} = 0 \quad . \quad . \quad . \quad (45)$$

may be obtained by cross-differentiation of equations (44) and (43*b*), where

$$\lambda_x = \frac{1 - M_{x\infty}^2}{1 + M_{\theta\infty}^2}, \qquad \lambda_\theta = \frac{1}{1 + M_{\theta\infty}^2}.$$

The solution* is $w = \Sigma\, e^{\pm k_n x}\, r^{\frac{M_{\theta\infty}^2}{2 + M_{\theta\infty}^2}}\, Z_{\left(\frac{2 + M_{\theta\infty}^2}{2 + 2M_{\theta\infty}^2}\right)}[k_n\sqrt{(1 - M_{x\infty}^2)}\, r]. \quad . \quad . \quad (46)$

The boundary conditions on this equation are $w = 0$ at $r = r_h$ and $r = r_t$. If $M_{\theta\infty} \longrightarrow 0$, this requirement is the same as that derived in the incompressible analysis,

$$J_1(k_n r_h)\, Y_1(k_n r_t) = J_1(k_n r_t)\, Y_1(k_n r_h) \quad . \quad . \quad . \quad (13)$$

and the solutions of Table I are valid.

*See Ref. 13, p. 146 for the general solution of Bessel type differential equations.

If $M_u \longrightarrow 1$, then the boundary condition requires that

$$J_{3/4}(k_n r_h)\, Y_{3/4}(k_n r_t) = J_{3/4}(k_n r_t)\, Y_{3/4}(k_n r_h). \quad . \quad . \quad . \quad (47)$$

Solutions to this equation are

r_t/r_h	1·0	2·0
$k_1(r_t - r_h)$	π	3·17

However, it should be noted here that the approximate solution is valid for low values of M_θ only. The assumption that $\partial\rho_\infty/\partial r$ is small has been made, and

$$\frac{\partial\rho_\infty}{\partial r} = \frac{1}{a^2}\frac{\partial p_\infty}{\partial r} = \frac{\rho_\infty}{r}\frac{v_\infty^2}{a^2} = \frac{\rho_\infty}{r} M_{\theta\infty}{}^2.$$

Thus if $\partial\rho_\infty/\partial r$ is small, then $M_{\theta\infty}{}^2$ must be small.

It is clear that the tangential Mach number makes but little difference to the axial decay factor. Taking the first term only

$$u' = \chi\, e^{-kx/\sqrt{(1 - M_{x\infty}{}^2)}}$$

where $l = r_t - r_h$ and $kl \simeq \pi$.

By writing $\rho = \rho_\infty(r) + \rho'$ and assuming $\partial\rho_\infty/\partial r$ is small, the perturbation density ρ' is obtained,

$$\left.\begin{aligned} \rho' &= -\chi M_{x\infty}{}^2 \frac{\rho_\infty}{u_\infty} e^{kx/\sqrt{(1 - M_{x\infty}{}^2)}} \quad \text{upstream,} \\ \rho' &= \chi M_{x\infty}{}^2 \frac{\rho_\infty}{u_\infty} e^{-kx/\sqrt{(1 - M_{x\infty}{}^2)}} \quad \text{downstream,} \end{aligned}\right\} \quad . \quad . \quad (37)$$

and

$$\left.\begin{aligned} \rho &= \rho_1\left(1 - \frac{\chi M_1{}^2}{u_1} e^{kx/\sqrt{(1 - M_1{}^2)}}\right) \text{upstream,} \\ \rho &= \rho_2\left(1 + \frac{\chi M_2{}^2}{u_2} e^{kx/\sqrt{(1 - M_2{}^2)}}\right) \text{downstream.} \end{aligned}\right\} \quad . \quad . \quad (37a)$$

2.6. Example of Three-Dimensional Compressible Flow

As an example of the three-dimensional case, the indirect problem of design of a guide vane row to produce a constant tangential velocity is again considered, but this time in a compressible flow of entry Mach number 0·5.

TABLE IV

$M_1 = 0{\cdot}5$, $A_1/A^* = 1{\cdot}339$ $M_1^* = 0{\cdot}534$, $\rho_1/\rho_0 = 0{\cdot}885$
$M_2 = 0{\cdot}625$, $A_2/A^* = 1{\cdot}339 \cos 30^\circ = 1{\cdot}161$, $M_2^* = 0{\cdot}659$, $\rho_2/\rho_0 = 0{\cdot}828$

$u_2 = u_1 \cos \varkappa \; (M_2^*/M_1^*) = 1{\cdot}068\, u_1$,
$\rho_2 = \rho_1 \; (0{\cdot}828/0{\cdot}885) = 0{\cdot}936\, \rho_1$.

TABLE V

z	u_1	M_1	M_1^*	$\frac{\rho_1}{\rho_0}$	$\frac{u_2}{\text{from (38)}}$	χ	$\frac{\chi M_2^2}{u_2}$	$\frac{\rho'}{\rho_2}$	$\frac{\rho_2}{\rho_1}$	$\frac{\rho_{02}}{\rho_1}$	$\frac{\rho_{02}}{\rho_0}$	M_{02}^*	u_{02}	$\frac{u_{02}}{\text{from (38)}}$
l	80	0·4	0·431	0·924	93·1	3·5	0·125	−0·012	0·936	0·948	0·876	0·554	89·1	89·6
$l/2$	100	0·5	0·534	0·885	106·1	0	0·125	0	0·936	0·936	0·828	0·659	106·1	106·1
0	120	0·6	0·635	0·840	119·1	−3·5	0·125	+0·012	0·936	0·924	0·778	0·757	123·5	122·6

TABLE VI

r	M_1	u_1	u_2	v_2	χ	u_{02}	$\sqrt{(u_2^2+v_2^2)}$	M_2^*	$\frac{\rho_2}{\rho_0}$	$\frac{\rho_{02}}{\rho_0}$	M_{02}^*	q_{02}	u_{02}	$\frac{u_{02}}{\text{from (18)}}$
1·0	0·5	100	92·4	100	−16·3	108·7	136·2	0·727	0·794	0·754	0·802	150·1	111·8	108·7
0·7	0·5	100	125	100	0	125	160·1	0·854	0·723	0·723	0·854	160	125	125
0·4	0·5	100	167·8	100	21·4	140·4	192·1	1·028	0·616	0·661	0·957	179·1	148·2	146·4

*An asterisk denotes conditions where $M = 1$.

The analysis for the incompressible flow is valid for the velocity u_2,

$$u_2 = \sqrt{(A - 2v_2^2 \log r)}, \quad . \quad . \quad . \quad . \quad . \quad (18)$$

but if $v_2 = 100$, as before, the constant A must be altered because of the drop in density through the guide vanes. Table VI shows an approximate solution; again values of u_{02} obtained from direct calculation and from the density calculation and from Ref. 11 are compared.

3. Discussion

The approximate solution for compressible flow should be limited to flows in which the axial Mach numbers do not approach unity, and the tangential Mach numbers are small. However, even in the example considered, of the compressible flow through a row of guide vanes, where the maximum tangential Mach number at exit is approximately 0·5, the density perturbations given by the analysis appear to be consistent with the velocity perturbations predicted. (It is of interest to note that the pressure variations may be transmitted axially upstream if the axial Mach number is less than unity, even if the absolute Mach number exceeds unity; but as the solution given has been derived for axial Mach numbers less than unity and small tangential Mach numbers, it would not be expected that the solution would be accurate in the example given in Table VI).

The particular case of irrotational flow through a "free vortex" guide vane row is interesting, since it illustrates further the restriction of low tangential Mach number and small values of $\partial\rho_\infty/\partial r = d\rho_\infty/dr$. The solution given suggests that there will be no perturbations in axial velocity on either side of the actuator disc, since $u_1 = u_{1m}$, $u_2 = u_{2m}$ and $\chi = \frac{1}{2}(u_2 - u_1) - \frac{1}{2}(u_{2m} - u_{1m}) = 0$. This is understandable for there is no tangential vorticity in a "free vortex" flow. Further the density perturbation $\rho' = \pm(\chi M_{z\infty}^2/u_\infty)\rho_\infty$ must also vanish. Since there is a pressure gradient with radius $d\rho_\infty/dr = \rho_\infty v_\infty^2/r$ far downstream, there must be a density variation also, and this will be the same as the density variation immediately downstream of the disc. This argument suggests that a radial displacement of the streamlines must take place at the disc, but not upstream and not downstream; since the disc is infinitesimally thin, there is a discontinuity in the streamline at the disc. However, it should be remembered that it was assumed in the analysis that $d\rho_\infty/dr$ was small, and any discontinuity in the streamlines at the disc must vanish under such restrictions.

The continuity equation is satisfied at the disc by equations (35) and (37). Upstream of the disc, the flow rate W is given by

$$W = \int_{r_h}^{r_t} u_{01}\rho_{01} r\, dr = \int_{r_h}^{r_t} (u_1 + \chi)\left(\rho_1 - \frac{\chi M_{z1}^2}{u_1}\rho_1\right) r\, dr$$

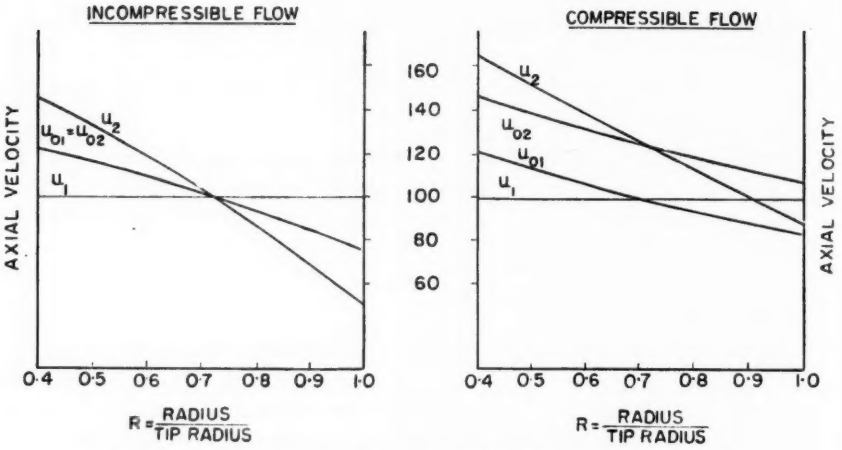

FIGURE 5. Axial velocity profiles. Example of flow through guide vanes.

and, since the term involving χ^2 is small compared with the other terms, this becomes

$$W = \int_{r_h}^{r_t} u_1 \rho_1 r \, dr + \int_{r_h}^{r_t} \rho_1 (1 - M_{x1}^2) \chi r \, dr.$$

Since $d\rho_\infty/dr$ and $dM_{x\infty}/dr$ are small; the second integral may be written in terms of ρ_{1m} and M_{1m}, the mean values of ρ_1 and M_{x1}

$$\rho_{1m}(1 - M_{1m}^2) \int_{r_h}^{r_t} \chi r \, dr = \rho_{1m}(1 - M_{1m}^2) \left[u_{2m} \int_{r_h}^{r_t} r \, dr - \int_{r_h}^{r_t} u_2 r \, dr - u_{1m} \int_{r_h}^{r_t} r \, dr + \int_{r_h}^{r_t} u_1 r \, dr \right]$$

$$= 0,$$

since, by definition, $u_{2m} = \dfrac{\int_{r_h}^{r_t} u_2 r \, dr}{\int_{r_h}^{r_t} r \, dr}$, $\quad u_{1m} = \dfrac{\int_{r_h}^{r_t} u_1 r \, dr}{\int_{r_h}^{r_t} r \, dr}$.

Thus $$W = \int_{r_h}^{r_t} \rho_1 u_1 r \, dr = \int_{r_h}^{r_t} \rho_{01} u_{01} r \, dr$$

and similarly $$W = \int_{r_h}^{r_t} \rho_2 u_2 r \, dr = \int_{r_h}^{r_t} \rho_{02} u_{02} r \, dr.$$

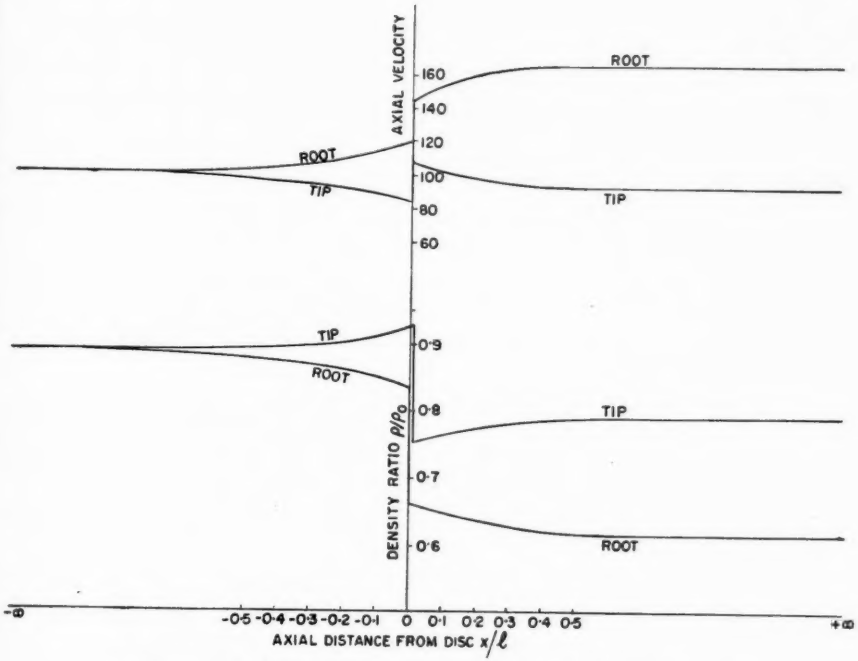

FIGURE 6. Flow through guide vanes. Axial velocity and density changes.

Finally it is of interest to compare the axial velocity profiles calculated in Tables III and VI, for the incompressible and compressible flows through guide vanes giving a constant tangential velocity at exit (Fig. 5). In the incompressible case there is axial acceleration at the root and axial deceleration at the tip, on both sides of the disc. In the compressible flow there is acceleration at the root up to the disc, across the disc and downstream of the disc. At the tip there is deceleration up to the disc, acceleration across the disc, and deceleration downstream of the disc. The compressible flow will result in less radial shift of the streamline, because of the increase in pressure and density towards the tip at exit from the row. The changes in axial velocity and density with axial distance x/l are shown in Fig. 6, for the example of Table V.

4. Conclusions

An analysis to determine the "axially" subsonic compressible flow through cascade actuator discs has been outlined. The decay effects on axial velocity observed in incompressible flow should be slightly less in compressible flow, since the exponential exponent of such decays is increased by the factor $1/\sqrt{(1-M_{z\infty}^2)}$, where $M_{z\infty}$ is the axial Mach number of the flow. Interference effects between

several rows may be calculated as in the incompressible theory, using the modified exponents given, and a design method similar to that of Ref. 12 may be used.

The density changes up to and away from the disc may be a considerable percentage of the overall density change from far upstream to far downstream (up to 50 per cent in the example considered).

REFERENCES

1. MERCHANT, W., HANSFORD, J. T. and HARRISON, P. M. The Flow of an Ideal Fluid in an Annulus. Metropolitan-Vickers Internal Report (unpublished), 1946.
2. MARBLE, F. E. The Flow of a Perfect Fluid through an Axial Flow Turbo Machine with Pre-described Blade Loading. *Journal of the Aeronautical Sciences*, Vol. 15, August 1948.
3. HAWTHORNE, W. R. Three Dimensional Flow in Compressors. Westinghouse Internal Report (unpublished), 1950.
4. RAILLY, J. W. The Flow of an Incompressible Fluid through an Axial Turbo-Machine with Any Number of Rows. *The Aeronautical Quarterly*, Vol. III, September 1951.
5. BRAGG, S. L. and HAWTHORNE, W. R. Some Exact Solutions of the Flow through Annular Cascade Actuator Discs. *Journal of the Aeronautical Sciences*, Vol. 17, April 1950.
6. HORLOCK, J. H. Some Actuator Disc Theories for the Flow of Air through Axial Turbo-Machines. R. & M. 3030, 1952.
7. RUDEN, P. Investigation of Single Stage Axial Flow Fans. N.A.C.A. T.M. 1062, 1944.
8. HAWTHORNE, W. R. and ARMSTRONG, W. D. Shear Flow through a Cascade. *The Aeronautical Quarterly*, Vol. VII, November 1956.
9. COHEN, H. and WHITE, E. M. The Theoretical Determination of the Three-Dimensional Flow in an Axial Compressor, with Special Reference to Constant Reaction Blading. A.R.C. 6842, 1943.
10. HORLOCK, J. H. Experimental and Theoretical Investigations of the Flow of Air through Two Single Stage Compressors. R. & M. 3031, 1955.
11. KEENAN, J. H. and KAYE, J. *Gas Tables*. John Wiley, New York, 1948.
12. HORLOCK, J. H. and CARMICHAEL, A. D. Actuator Disc Theories Applied to the Design of Axial Compressors. A.R.C. Current Paper 315, 1957.
13. JAHNKE, E. and EMDE, F. *Tables of Functions*. Dover Publications, New York, 1946.

The Relation between Zero Errors and Bandwidths for Different Types of Rate-of-Turn Meters

H. SUTCLIFFE

(University of Bristol)

SUMMARY: In a conventional rate-of-turn measuring gyroscope the necessity to use a displacement transducer results in an appreciable zero error when a rapid response is required. Other types of instrument, employing alternating forces and force transducers, are also shown to have a relation between error and response time. An assessment is made of these relations and conclusions are reached concerning the relative merits of the different types. The results are given in terms of the estimated rate errors as functions of bandwidth.

1. Introduction

A rate-of-turn meter is an instrument which is mounted in a vehicle for the purpose of measuring the angular velocity of the vehicle about some axis. The instrument produces a signal which is normally used in connection with the mechanism which controls the vehicle. This present discussion is restricted to cases where the signal is proportional to the rate of turn. The signal is usually required to be electrical, and it follows that a rate-of-turn meter in its entirety must consist of all the sections shown in the schematic diagram of Fig. 1. The rate of turn is Ω and the output quantity of the instrument is v_{out}. For an ideal instrument $v_{out}=k\Omega$, where k is a constant for the particular design. In a real instrument there will be four major deviations from this ideal state of affairs. Two of these, the variations in sensitivity due to variations in k and the phenomenon of saturation or non-linearity for large values of Ω, will not be considered here. The two limitations to be discussed are the zero error of the instrument and the sluggishness of the response.

The zero error is defined in terms of the indicated response to a constant applied value of Ω. If $v_{out}=k(\Omega+\Omega_e)$, then the rate error is Ω_e and is the indicated rate when Ω is zero.

The sluggishness of the instrument is difficult to define in terms which are of general application to a variety of different instruments, and precision in the

Received April 1957.

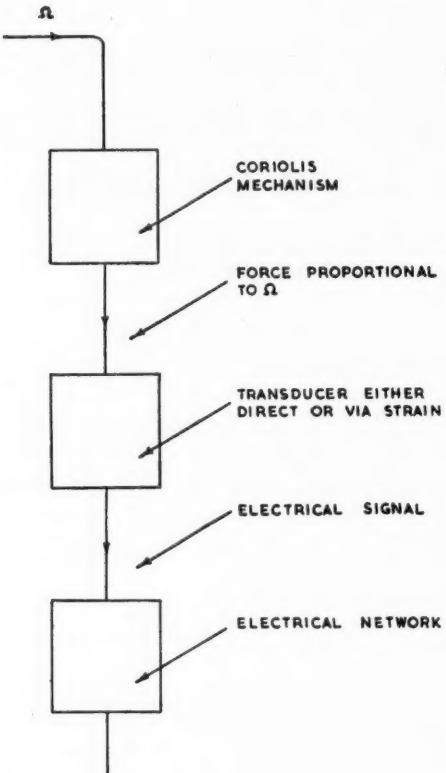

FIGURE 1. The components of a rate-of-turn meter.

definition must be sacrificed to make comparison possible. Assume that a test is made in which the input rate is given by

$$\Omega = \Omega_{max} \cos qt.$$

The output indication, neglecting any zero error, will be

$$v_{out} = V_{max} \cos (qt - \phi).$$

When q is small, V_{max} will be $k\Omega_{max}$ and ϕ will be zero. As q is increased it will pass through a value B at which the reduction of V_{max} below the value $k\Omega_{max}$, or the value of ϕ, or both, will be significant. This value of B will be taken to be the bandwidth of the instrument and the response of the instrument to a step function

$\Omega 1\,(t)$ will be similar to that of a single time-lagging network. That is to say the output will approximate to the shape $v_{out} = k\Omega\,(1 - e^{-Bt})$. The response time may be defined as $1/B$. The particular value of B to be allocated to different types of instrument is discussed later.

The conventional rate gyroscope described in Section 2.1 is in common use and its limitations are well known to arise because the force produced is constant for a constant applied rate of turn. The transducer which converts this force into an electrical signal must therefore be of the displacement type used in connection with a mechanical strain[1]. Zero errors are associated with the transducer and bandwidth is restricted by the necessity to displace mass. These difficulties are removed when the force produced by the rate of turn is alternating, since piezo-electric transducers can be used which operate directly from the applied force. The principle has been adopted in the design of several instruments[2]-[9] and, if no other source of error had been found to occur in these, the conventional rate gyroscope would now be of historical interest only.

Instruments which use an alternating force may be classified into two types, the dumb-bell gyroscope and the vibrating gyroscope. It is found in practice that in both these types, as in the conventional rate gyroscope, there is a rate error which is related to bandwidth. The nature of this relation is discussed in the following sections and an attempt is made to assess the relative merits of the three types on a quantitive basis.

All three types of instrument also have errors which are independent of bandwidth. A conventional rate gyroscope, for instance, will have errors due to mass unbalance and friction, while the other two types produce spurious forces at the transducer which are functions of the position of the moving parts. Errors arising from effects such as these become dominant only when a small bandwidth is adequate. A discussion of the situation under this condition is excluded from this paper, not because the subject lacks interest and importance, but because sufficient information about the relevant effects is not available.

NOTATION

a	radius of locus of point mass amplitude of vibration of point mass
b	distance from centre line
B	bandwidth in radians/second
I_x, etc.	moments of inertia about OX, etc.
J	rotor moment of inertia
k	sensitivity constant
K	spring angular stiffness
m	mass

q angular frequency of test signal

T_y, etc. torque about OY, etc.

T_e torque produced by error in instrument

T_s torque component which produces a signal

v_{out} output signal from instrument

V_{max} peak amplitude of electrical signal

x, y, z co-ordinates

α acceleration

θ, θ_e, etc. angle, angular misalignment, etc.

ϕ phase angle of overall response

ω angular frequency of spin or vibration

Ω_x, etc. rate of turn of instrument about OX, etc.

Ω_e error in measurement of Ω

The suffix "max" denotes a peak value.

2. Analysis of Errors and Bandwidths for Three Types of Instrument

2.1. The Conventional Rate-Measuring Gyroscope

Figure 2 shows the instrument in one of the many possible mechanical arrangements. The rotor R has moment of inertia J and spin ω about the OX-axis. The outer gimbal OG is fixed to the vehicle whose rate of turn Ω_y about the OY-axis is to be measured. Gyroscopic forces produce a torque T_z about the OZ-axis, given by

$$T_z = J\omega\Omega_y.$$

The spring system S is displaced such that the angular displacement of the inner gimbal about OZ is θ, where θ is a small angle. Then if the angular stiffness of the spring system is K, the following relation holds.

$$\theta = \frac{T_z}{K} = \frac{J\omega\Omega_y}{K}. \quad . \quad . \quad . \quad . \quad . \quad (1)$$

The mechanism for transmitting the angle θ will include a displacement transducer such as an E and I-bar electromagnetic pick-off. A quantity θ_e is postulated which is a measure of the misalignment of the instrument. It may be caused by imperfections in either the mechanical construction and assembly or in the transducer and its associated electrical circuits. The corresponding rate error Ω_e is given by

$$\Omega_e = \theta_e K/(J\omega). \quad . \quad . \quad . \quad . \quad . \quad (2)$$

The bandwidth of the response is limited by the moment of inertia I of the inner gimbal and rotor about OZ. The amplitude response is dependent on the amount of viscous damping, but a representative figure for the bandwidth can be

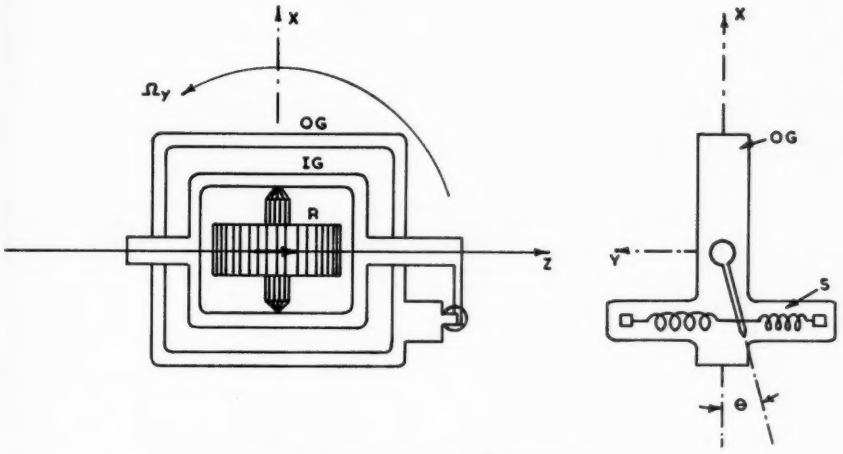

FIGURE 2. Conventional rate gyroscope.

taken to be the frequency at which the phase of the response lags by 90°. This will be the case at the natural resonant frequency which is determined by spring stiffness and inertia only, and the bandwidth is given by

$$B^2 = K/I. \quad . \quad . \quad . \quad . \quad . \quad . \quad (3)$$

It will be appreciated that a large value of K is required in order to provide a sufficiently large bandwidth, that is a stiffly sprung system must be used. It follows that for a given value of misalignment the rate error is correspondingly great. Quantitatively, by combining (2) and (3),

$$\Omega_e = \theta_e B^2 I/(J\omega). \quad . \quad . \quad . \quad . \quad . \quad (4)$$

The smallest possible ratio I/J would be attained with a disc rotor and a massless inner gimbal, when the value would be 1/2. A representative value which is obtainable in practice is unity, in which case equation (4) becomes

$$\Omega_e = \theta_e B^2/\omega. \quad . \quad . \quad . \quad . \quad . \quad . \quad (5)$$

2.2. THE DUMB-BELL GYROSCOPE

One possible form of this instrument is shown in Fig. 3. The rotor R spins with angular frequency ω about the OZ-axis and may be considered, so far as the basic operation is concerned, to consist of two point masses m at radius a. The rotor is carried on an inner gimbal IG which is fixed in position by a pair of force transducers TT to an outer gimbal OG. This outer frame is fixed to the vehicle. The whole structure experiences rates of turn Ω_x and Ω_y about the OX- and OY-axes.

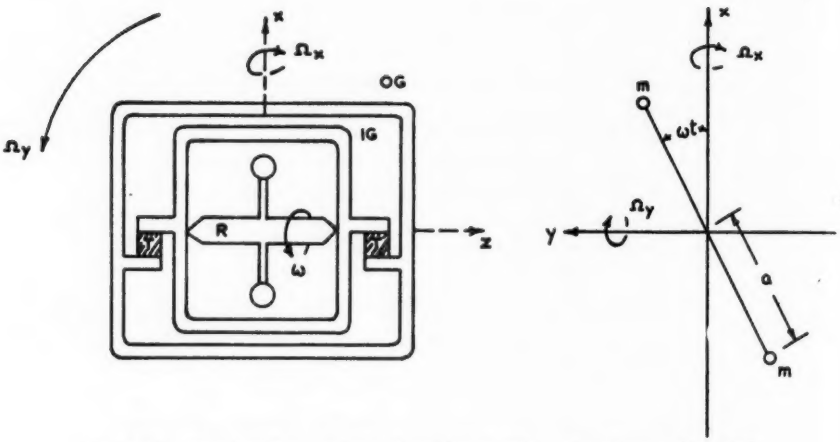

FIGURE 3. Dumb-bell gyroscope. Transducers TT measure torque about OY.

Coriolis forces are transmitted between the vehicle and the spinning masses through the transducers, which are connected in such a way as to produce a signal which is a measure of the fluctuating component of the torque T_y about the OY-axis.

The acceleration of the top mass in the OZ-direction is α_z, given by

$$\alpha_z = 2a\omega\,[\Omega_x \cos\omega t + \Omega_y \sin\omega t].$$

Thus the total torque about the OY-axis is given by

$$T_y = 2m\alpha_z a \cos\omega t$$

$$= 2ma^2\omega\,[\Omega_x(1+\cos 2\omega t) + \Omega_y \sin 2\omega t].$$

The constant component is not measured by the transducers and the signal torque is given by

$$T_s = 2ma^2\omega\,[\Omega_x \cos 2\omega t + \Omega_y \sin 2\omega t]. \quad . \quad . \quad . \quad (6)$$

The corresponding electrical signal from the transducers is amplified and passed to two demodulators (phase-sensitive rectifiers) in order to obtain two output signals proportional to Ω_x and Ω_y. The carriers which are also required at the demodulators must have the form $\cos 2\omega t$ and $\sin 2\omega t$ and can be derived from a pick-off operated by the angular position of the rotor.

This analysis is concerned with magnitudes of error and it is convenient to note that Ω_x and Ω_y are components of an angular rate Ω about some line in the XY-plane.

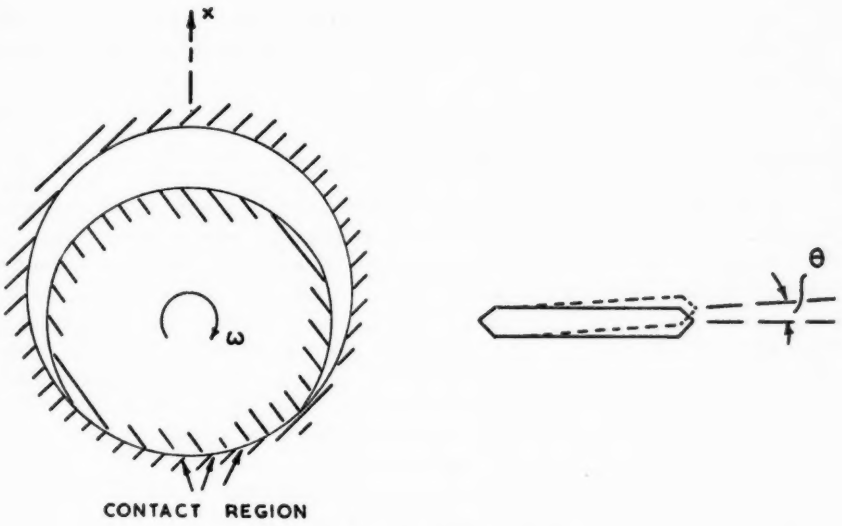

FIGURE 4. One source of error in a dumb-bell gyroscope.

Then, if T_{max} is the peak amplitude of the signal torque T_s in (6), the following simple result is obtained

$$T_{max} = 2ma^2\omega\Omega. \quad . \quad . \quad . \quad . \quad . \quad (7)$$

The instrument will have an error when a spurious signal coherent with the carrier frequency 2ω is present in the signal amplifier. Such a signal may be caused by electrical interference and its elimination may present practical difficulties, but a more fundamental source of error is in the mechanical portion of the instrument. Imperfections in the rotor bearings can cause the rotor axis to deviate from the OZ-axis though small angles θ_x and θ_y in the OX- and OY-planes. If θ_x or θ_y has a component at 2ω, then the torque T_y also has a component at 2ω. Figure 4 shows one of the more obvious sources of error. One of the rotor bearings is slightly elliptical, so that one end of the rotor axis shifts to and fro at twice the rotational frequency.

Consider first the deviation θ_x. Then, if the peak value of the component at 2ω is $\theta_{x\,max}$, the peak value of the angular acceleration of the rotor about OY is $4\omega^2\theta_{x\,max}$. Let I_y be a representative figure for the moment of inertia of the rotor about OY. Then the peak amplitude of the component at 2ω of the torque is given by

$$T_{e1\,max} = 4\omega^2\theta_{x\,max}I_y. \quad . \quad . \quad . \quad . \quad . \quad (8)$$

Now consider the effect of a similar deviation $\theta_{y\,max}$. Torque about the OY-axis is now produced by gyroscopic action of the rotor, and the peak value at 2ω is given by

$$T_{e2\,max}=2\omega^2\theta_{y\,max}J, \quad . \quad . \quad . \quad . \quad . \quad . \quad (9)$$

where J is the moment of inertia of the rotor about OZ.

Equations (8) and (9) ignore the fact that the rotor has a dumb-bell distribution of mass and are therefore simplifications of a somewhat more complex result. It will be realised, however, that in a practical instrument there will be a considerable amount of mass, with radial symmetry about the rotor axis, for which (8) and (9) are valid in an elementary manner. An example of a more detailed analysis is provided in the Appendix. The main purpose of this paper will be served by noting that, if the rotor structure approximates to a disc, then J in (9) will be nearly equal to $2I_y$ in (8), and that a good approximation for I_y is to take the value $2ma^2$. The phase of the error signal is of no significance, since the signals representing Ω_x and Ω_y exist in the same circuit as vectors which are mutually at 90°. There is thus no possibility of eliminating errors by phase discrimination and it is reasonable to drop the suffixes and replace (8) and (9) by

$$T_{e\,max}=4\omega^2\theta_{e\,max}2ma^2 \quad . \quad . \quad . \quad . \quad . \quad . \quad (10)$$

where T_e is the peak magnitude of the error signal.

The corresponding rate error Ω_e is obtained by combining (10) and (7): —

$$\Omega_e=4\omega\theta_{e\,max}. \quad . \quad . \quad . \quad . \quad . \quad . \quad (11)$$

The available bandwidth is determined in practice by the presence of a signal in the transducer at frequency ω, caused by rotor unbalance, by the desirability of arithmetical symmetry in the response of the signal amplifier about the frequency 2ω, and by the necessity to filter out the carrier component after demodulation. It has been found that $B=\omega/2$ is representative of the highest practical value for the bandwidth. Then the equation which relates rate error, bandwidth and mechanical imperfections is

$$\Omega_e=8B\theta_{e\,max} \quad . \quad . \quad . \quad . \quad . \quad . \quad (12)$$

2.3. The Vibrating Gyroscope

Figure 5 shows the mechanical construction in one type of instrument, in which a pair of tines vibrates in the same way as a tuning fork. The situation is similar to the case of two masses oscillating sinusoidally along lines which in the ideal case pass through the axis OY about which torque is measured. Then if the amplitude of oscillation a is appreciably less than the distance b, the signal torque is given by

$$T_y=2b\times 2ma\omega\cos\omega t\Omega_y. \quad . \quad . \quad . \quad . \quad (13)$$

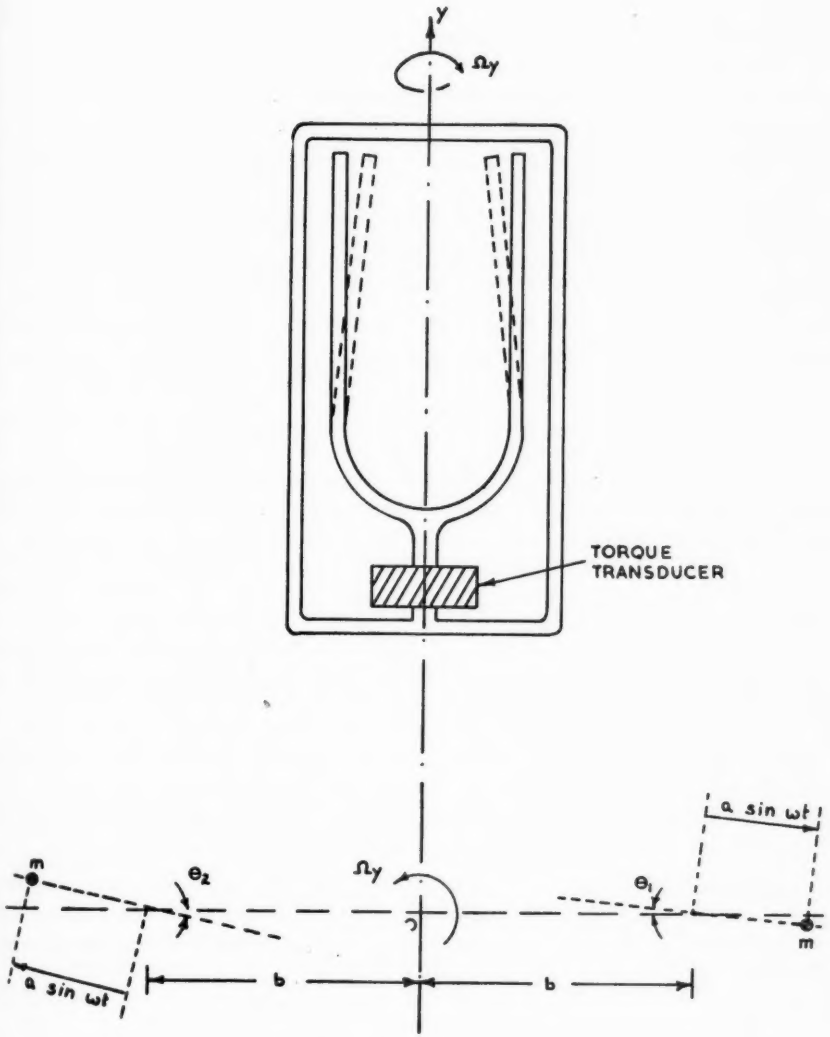

FIGURE 5. One form of a vibrating gyroscope.

This signal torque is converted by the transducer, amplified and demodulated in a phase-sensitive rectifier for which the carrier is $\cos \omega t$ and is derived from tine velocity. The output of the demodulator is then proportional to Ω_y.

One way in which an error torque can arise is shown in Fig. 5, where the lines of travel of the masses are displaced through angles θ_1 and θ_2 from their

correct orientation. The large acceleration of the masses along their lines of travel will produce an error torque T_{ey} given by

$$T_{ey} = bma\omega^2 (\theta_1 + \theta_2) \sin \omega t. \quad . \quad . \quad . \quad . \quad (14)$$

T_{ey} and T_y differ in that they are sine and cosine functions of ωt respectively. If, then, the control of phase angles throughout the whole instrument were perfect, the output signal after demodulation would contain no error. Phasing errors can arise, however, in every section of the instrument and their effect can be taken into account by adding a small angle θ_{ep} to the ωt in (14). Then the component of T_{ey} which is in phase with T_y will have a magnitude $T_{e\,max}$ given by

$$T_{e\,max} = bma\omega^2 (\theta_1 + \theta_2)\, \theta_{ep}. \quad . \quad . \quad . \quad . \quad (15)$$

The rate error Ω_e, obtained from (13) and (15), is thus given by

$$\Omega_e = \frac{\omega}{4} (\theta_1 + \theta_2)\, \theta_{ep}. \quad . \quad . \quad . \quad . \quad . \quad (16)$$

A more general summary, not restricted to any particular mechanical configuration, can be given, which leads to a similar conclusion. Any oscillating mass will have two accelerations, a wanted one due to the applied rate of turn, and an unwanted one due to its oscillation. The ratio of the amplitudes of these two accelerations, wanted to unwanted, is $2\Omega_y/\omega$. The two accelerations are each sinusoidal with time at angular frequency ω, but in both relative direction and in relative phase angle they differ by 90°. The reduction of rate error depends on the success with which these two right angles can be maintained and, if they are in error by amounts θ_{em} and θ_{ep}, the rate error is

$$\Omega_e = \frac{\omega}{2} \theta_{em} \theta_{ep}. \quad . \quad . \quad . \quad . \quad . \quad (17)$$

The suffixes "m" and "p" are reminders of the mechanical and phasing sources of error.

The bandwidth of the instrument is restricted by the carrier frequency and the necessity for filtering after demodulation. A value $B = \omega/2$ will be taken as the largest bandwidth which will be practicable. Then the relation between rate error, bandwidth and imperfections is

$$\Omega_e = B\theta_{em}\theta_{ep}. \quad . \quad . \quad . \quad . \quad . \quad (18)$$

3. The Nature and Magnitude of the Sources of Error

The three significant equations, (5), (12) and (18), are reproduced here for convenience.

Type	*Equation of performance*
Conventional rate gyroscope	$\Omega_e = \theta_e B^2/\omega$
Dumb-bell gyroscope	$\Omega_e = \theta_e 8B$
Vibrating gyroscope	$\Omega_e = \theta_{em}\theta_{ep}B$

Each factor θ_e represents an error in alignment and it is necessary to define the nature of these errors before any conclusions can be drawn concerning the relative excellence of the three types, or of different designs of the same type. Suppose a batch of one design is being manufactured, tested and put into service. At the final stage of assembly, and before testing, each model will be aligned and adjusted to make Ω_e equal to zero, or very nearly so. The significant appearance of θ_e and Ω_e will arise later when the model is subjected to changes of temperature, variations in "g," wear of bearings, fatigue of highly strained metal, ageing of components and many other ill effects. A knowledge of θ_e and Ω_e for the design is thus derived partly from tests after assembly and partly from service trials. The errors have a correlation with the environment to which the instrument is subjected and the figure quoted for the design is that which can be achieved in the most trying environment. Any comparison between designs must be done in relation to the same environment.

Within any one type it is clear that a smaller value of θ_e and consequently of Ω_e may be obtained for a particular design by a combination of ingenuity in conception, by the use of materials with suitable properties and by precision of workmanship. These requirements may be summed up in the word "cost." It will be assumed here that different designs within one type will have the same value of θ_e if they have the same cost.

To compare the relative excellence of different types, it is desirable to compare the performance of designs which have the same cost. The difficulties in the assessment of cost are obvious and it must be emphasised that the quantitative comparison which follows is based entirely on the author's restricted experience and intuition. The figures for rate errors may well be incorrect by a large factor for the dumb-bell and vibrating gyroscope, since the techniques involved in their design are in their infancy and conclusions must be drawn from one or two samples. This proviso, however, does not detract from the significance of the way in which rate error varies with bandwidth in the different types. The quantitative comparison relies on the use of arguments such as the following.

The thermal coefficient of expansion of most metals[10] is in the region of 10^{-5} per °C. Thus a structure of uniform material with a square cross section, with one pair of opposite faces differing in temperature by 5°C, will experience a tilting of the relative angle of the other two faces through an angle 1/20,000. In a similar shaped structure whose opposite sides are made of materials whose coefficients of expansion differ by 10^{-6} per °C, the same tilt is reached for a temperature change, uniform in the whole structure, of 50°C.

The construction of two separate parts of a mechanism to limits of half of one ten thousandth of an inch, at a radius of one inch, represents very precise workmanship. The corresponding angle is 1/20,000.

It may be expected then that the maintenance of the alignment of angles to better than 1/20,000 in any instrument will be achieved only by a considerable increase in cost. This will be particularly true for the vibrating gyroscope, where

the error angle θ_{em} arises in a part of the mechanism which must be free to vibrate. At equivalent cost, then, a prediction for θ_e for the conventional gyroscope is 1/20,000 and the value θ_{em} for the vibrating gyroscope may be expected to be somewhat larger. For the dumb-bell gyroscope a prediction of θ_e is rather difficult, since there is no general information about the second harmonic motion of high-speed bearings. A very approximate estimation can be made by assuming that the running clearance in the bearings will be in the region of 0·0001 in. Then, with bearings two inches apart, the rotor axis cannot change through an angle greater than 1/10,000. Thus θ_e cannot be greater than $2/\pi$ times this and is likely to be appreciably smaller.

Turning now to specific instruments, from which conclusions can be drawn, a conventional rate gyroscope is considered first. A typical design has a wheel speed of 12,000 r.p.m. and a resonant undamped frequency of 100 c./s. It passes a severe environmental test for which a rate error of 1° per second is allowed. The corresponding value of θ_e is 1/18,000.

Model dumb-bell gyroscopes have been built and tested. Values of θ_e were measured both directly and by inference from rate errors. Good correlation was obtained over a range of wheel speeds and a figure of $3{\cdot}5 \times 10^{-6}$ was arrived at for θ_e for the same conditions of cost and environment as in the previous case.

Experimental vibrating gyroscopes have been built and tested. A typical value of rate error was found to be 2° per second when the vibrational frequency was 100° c./s., so the value of $(\theta_{em}\theta_{ep})$ in the models was in the region of 1/9,000. The models, however, had a low cost in the sense which has been defined, the sources of error were well established, and it is believed that designs whose cost was equivalent to the other two examples would have values of $(\theta_{em}\theta_{ep})$ in the region of 1/30,000.

The result of these considerations is to suggest the following values for the error quantities in equations (5), (12) and (18).

Conventional rate gyroscope: $\theta_e = 1/20{,}000$

Dumb-bell gyroscope: $\theta_e = 1/300{,}000$

Vibrating gyroscope: $\theta_{em}\theta_{ep} = 1/30{,}000.$

It is now possible to make a direct comparison between the three types of instrument. Figure 6 shows the minimum rate error available in the three types, assuming equivalent cost and environment, plotted against bandwidth. Logarithmic scales are convenient for the presentation. For the conventional rate gyroscope a rotor speed of 24,000 r.p.m. (400 c./s.) is assumed whatever bandwidth is required, whereas in the other two cases it is assumed that rotor speed or vibrational frequency is as low as is consistent with obtaining the required bandwidth. The highest rotor speed for the dumb-bell gyroscope is taken to be 24,000 r.p.m., which implies an upper limit of 200 c./s. for the bandwidth.

RATE ERROR IN DEGREE / SECOND

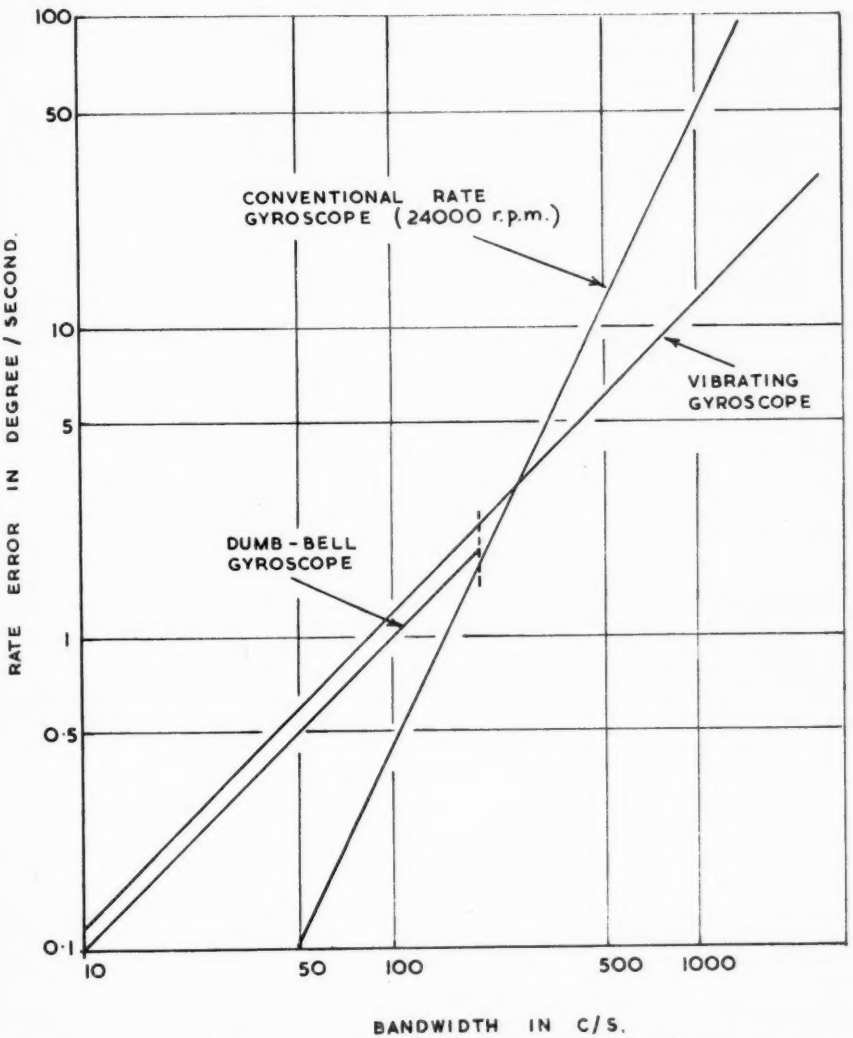

FIGURE 6. Relation between rate errors and bandwidth in comparable designs of the three types of instrument.

4. Conclusions

The first point arising from the results shown in Fig. 6 is that the dumb-bell gyroscope appears to be outclassed by the conventional type, although the situation could be modified by a fortunate discovery in the subject of elimination of

second harmonic play in high-speed bearings. The dumb-bell gyroscope would then be the best type for applications which require bandwidths up to the region of half the upper limit of wheel frequency.

At present the two main contestants are the conventional and vibrating types of instrument. The conventional type is superior for bandwidths up to the region of 300 c./s., while the vibrating type would be superior if wider bandwidths were required. The increase of error with bandwidth is an inexorable feature of all the instruments.

The results become invalid for small bandwidths. Fig. 6 suggests that the zero error in all three types decreases continuously, whereas each type of instrument has a zero error, independent of bandwidth, which becomes dominant at small bandwidths. With regard to the conventional rate gyroscope, quantitative information about the performance under these conditions is in existence. An investigation of the performance of the other two types, using models in which the moving parts had low rotational or vibrating frequencies, could yield some interesting and perhaps valuable results.

ACKNOWLEDGMENTS

The experimental work in connection with this paper was done in the Research Laboratories of Smith's Aircraft Instruments Ltd. The author is indebted to the management for permission to publish this article and to many of his former colleagues for their assistance and for stimulating discussions. However, in view of the controversial nature of some of the conclusions, it must be stated that these reflect the personal opinion of the author and not necessarily the policy of the firm.

Appendix

Angular Vibration of the Dumb-Bell Gyroscope at Twice Rotor Speed

The practical case will be considered in which there is a concentration of mass towards the dumb-bell axis, instead of the simpler case of two point masses. Suppose that mass is concentrated towards an axis OX_0 referred to the rotor. The rotor will be assumed to spin about an axis OZ_0 and to have symmetry about the X_0Z_0- and Y_0Z_0-planes. Let the rotor spin at angular frequency ω with respect to axes OX, OY, OZ referred to the frame or gimbal, such that OZ coincides with OZ_0 at all times and that $x=x_0$, $y=y_0$ at $t=0$. Then the position and velocity of an element of mass δm, with respect to the frame, is given by

$$z=z_0$$

$$x=x_0\cos\omega t-y_0\sin\omega t,\quad \dot{x}=\omega\left[-x_0\sin\omega t-y_0\cos\omega t\right]$$

$$y=x_0\sin\omega t+y_0\cos\omega t,\quad \dot{y}=\omega\left[x_0\cos\omega t-y_0\sin\omega t\right].$$

The transducer is constructed so that it measures the torque T_y about the OY-axis.

(*i*) *The Effects of Rates of Turn Ω_y and Ω_x*

$$T_y=\Sigma\delta mx\,(2\Omega_y\dot{x})-\Sigma\delta mx\,(2\Omega_x\dot{y}).$$

Now $\Sigma\delta m x_o y_o$ is zero, by the symmetry of construction of the rotor.

Therefore
$$T_y = -\Omega_y\omega\Sigma\delta m\,(x_o^2 - y_o^2)\sin 2\omega t - \Omega_x\omega\Sigma\delta m\,(x_o^2 + y_o^2) - \\ -\Omega_x\omega\Sigma\delta m\,(x_o^2 - y_o^2)\cos 2\omega t. \qquad (19)$$

Let J be the rotor moment of inertia about OZ_o and let I_d, the effective dumb-bell, be
$$\Sigma\delta m\,(x_o^2 - y_o^2).$$

Then
$$T_y = -\omega I_d\,[\Omega_x\cos 2\omega t + \Omega_y \sin 2\omega t] - J\omega\Omega_x. \quad . \quad . \quad . \qquad (20)$$

Consider an oscillation of the rotor axis through an angle θ_e at an angular frequency 2ω such that $\Omega_x = 2\omega\theta_{e\,max}\sin 2\omega t$. Then the component of T_y at 2ω will have an amplitude given by

$$T_{e1\,max} = 2J\omega^2\theta_{e\,max}. \quad . \quad . \quad . \quad . \quad . \qquad (21)$$

(*ii*) *The Effect of Angular Acceleration about OY*

Let the angular acceleration be $\dot{\Omega}_y$.

Then
$$T_y = \dot{\Omega}_y\Sigma\delta m\,(z^2 + x^2)$$
$$= \dot{\Omega}_y\Sigma\delta m\,[z_o^2 + x_o^2\cos^2\omega t + y_o^2\sin^2\omega t]$$
$$= \dot{\Omega}_y\Sigma\delta m\,[\tfrac{1}{2}(z_o^2 + x_o^2) + \tfrac{1}{2}(z_o^2 + y_o^2)] + \tfrac{1}{2}\dot{\Omega}_y\Sigma\delta m\,(x_o^2 - y_o^2)\cos 2\omega t, \qquad (22)$$

Then, if the moments of inertia of the rotor about its axes OX_o and OY_o are I_{xo} and amplitude given by
I_{yo} respectively,

$$T_y = \tfrac{1}{2}\dot{\Omega}_y\,[I_{xo} + I_{yo}] + \tfrac{1}{2}\dot{\Omega}_y I_d\cos 2\omega t. \quad . \quad . \quad . \quad . \qquad (23)$$

Consider an oscillation about OY of peak value $\theta_{e\,max}$ such that $\dot{\Omega}_y = 4\omega^2\theta_{e\,max}\sin 2\omega t$. The component of T_y at 2ω will have an amplitude given by

$$T_{e2\,max} = 2\,[I_{xo} + I_{yo}]\,\omega^2\theta_{e\,max}. \quad . \quad . \quad . \quad . \qquad (24)$$

(*iii*) *Rate Errors*

Let rate errors Ω_{e1} and Ω_{e2} correspond to torques T_{e1} and T_{e2}.

Then
$$\Omega_{e1} = 2\omega\theta_{e\,max}\,J/I_d \quad \text{and} \quad \Omega_{e2} = 2\omega\theta_{e\,max}\,(I_{xo} + I_{yo})/I_d.$$

In the ideal case there will be mass only along OX_o, and both J/I_d and $(I_{xo} + I_{yo})/I_d$ will be unity. They cannot be smaller. Then the limiting value of rate error is $2\omega\theta_{e\,max}$. A practical case had values as follows:—

$$J = 2325,\ I_{yo} = 1680,\ I_{xo} = 770\text{ gm. cm.}^2,$$

from which
$$I_d = 910\text{ gm. cm.}^2$$

Then $$J/I_d = 2{\cdot}55, \quad (I_{xo} + I_{yo})/I_d = 2{\cdot}69.$$

It will be seen that the numerical factor 4 in equation (11) is representative of what can be achieved in practice.

It will be seen from (23) that any angular acceleration of the vehicle appears as a rate error. This feature is common to all three types of instrument.

REFERENCES

1. SPRATT, H. M. G. Transducer Characteristics. *Electronic and Radio Engineering*, Vol. 34, No. 1, p. 2, January 1957.
2. LYMAN, J. A New Space Rate Sensing Instrument. *Aeronautical Engineering Review*, Vol. 12, No. 11, p. 24, November 1955.
3. BARNABY, R. E., *et al.* General Theory and Operational Characteristics of the Gyratron Angular Rate Tachometer. *Aeronautical Engineering Review*, Vol. 12, No. 11, p. 31, November 1955.
4. MERIDITH, F. W. Improvements in or relating to Devices for Detecting or Measuring Rate of Turn. British Patent No. 611,005, October 1948 and British Patent No. 611,021, October 1948.
5. LYMAN, J. Rate and Attitude Indicating Instrument. U.S. Patent 2,309,853, February 1943.
6. LIVERSEDGE, J. H. Improvements in and relating to Turn-Sensitive Devices. British Patent No. 865,113, December 1952.
7. JAFREE, H. Improved Means for Measuring Angular Velocities and Displacements. British Patent No. 685,369, January 1953.
8. MASON, *et al.* Rate of Turn Instrument. U.S. Patent No. 2,683,596, July 1956.
9. ARREA, E. Gyroscope Compass and Latitude Indicator. U.S. Patent No. 1,801,619, April 1931.
10. KAYE, G. W. C. and LABY, T. H. *Tables of Physical and Chemical Constants*, 11th Edition, Longmans Green, London, p. 53, 1956.
11. CHATTERTON, J. B. Some General Comparisons between the Vibrating and Conventional Rate Gyro. *Journal of the Aeronautical Sciences*, Vol. 22, p. 633, September 1955.
12. FEARNSIDE, K. and BRIGGS, P. A. N. The Mathematical Theory of Vibrating Rate Tachometers. *Proceedings of the Institution of Electrical Engineers*. Monograph 264M, November 1957.

Photoelastic Investigation on Plates with Single Interference-Fit Pins with Load Applied (a) to Pin only and (b) to Pin and Plate Simultaneously

H. T. JESSOP, C. SNELL and G. S. HOLISTER

(Department of Civil and Municipal Engineering, University College, London)

SUMMARY: The reduction in stress concentration factors resulting from the introduction of an interference-fit pin in a circular hole in a flat plate to which a simple tension is applied has already been recorded[4]. The same result is found to occur to an equally marked extent, and qualitatively in a very similar way, when the load is applied to the pin itself. When varying loads are applied to the pin or the plate, the effect of the interference is to produce a rise in the mean stress level at critical points on the hole boundary with a marked fall in the oscillatory stress. There appears to be an optimum value for the "interference stress" for given applied loading conditions at which the endurance of the plate will have its highest value.

When loads are applied simultaneously to pin and plate the critical stress on the hole boundary is found to be the mean of the stresses which would be produced by the total load applied separately to the pin and to the plate.

1. Introduction

This is the fourth stage of the photoelastic tests in the programme of research initiated by the Royal Aeronautical Society and outlined in Ref. 1, and it concludes the investigation of the "single hole" case. Previous results have been published in Refs. 2, 3 and 4. This investigation deals with plates with circular holes filled by interference-fit pins with loads applied (*a*) to the pin only, and (*b*) to pin and plate simultaneously.

In this investigation a series of tests was first carried out on plates with loads applied to the pin only, the intention being at that time to make a few "spot" observations with loads on pin and plate simultaneously. It was decided, however, to carry out in the second stage a series of tests covering the whole range of combined loads. In this series, the previous observations under pin load only and

Received October 1957

plate load only were repeated, and were found to give very good agreement with those of the earlier tests. In this report the results are all taken from the combined load observations.

NOTATION

E Young's modulus of plate

E_1 Young's modulus of pin

D width of plate

d, d' diameters of hole and pin respectively

$(d' - d)/d$ degree of interference

t mean tensile stress in undrilled plate due to applied tension

t' nominal mean tensile stress across section through hole centre, due to applied tension, $= Dt/(D - d)$

t_m = maximum tensile stress on hole boundary

s_m = maximum shear stress on hole boundary

The stress concentration factors derived here are given in terms of the *increase* in peak tensile or shear stress produced by the applied tension.

Thus:—

S.C.F. for tensile stresses $= \delta t_m/t'$

S.C.F. for shear stresses $= \delta s_m/t'$

2. Conditions of Tests

As in previous tests, the models were Araldite bars, 1 in. wide and $\frac{1}{8}$ in. thick.

The pin load was applied through two thin steel strips which passed over the projecting ends of the pin and were attached to a skeleton box frame. These strips can be seen in the photographs of Fig. 1. The ends of the pin were turned down, in order that the strips should obscure as little of the hole boundary as possible.

The tests in this series were confined to plates with two sizes of hole, namely $\frac{1}{4}$ in. and $\frac{3}{8}$ in. diameter—these representing the ratios of hole diameter to plate width most frequently used in practice. The pins used throughout the test were of Bakelite B.166, a paper base Bakelite giving a modular ratio E_1/E of 2·15, the nearest obtainable to the 3/1 ratio required to represent a steel pin in a light alloy plate. (In previous tests no significant difference in stresses was observed for different ratios of E_1/E).

Three degrees of fit were investigated; push fit and two degrees of interference, namely 0·003 and 0·006, corresponding approximately to maximum *elastic* shear stresses in a light alloy bar of 20,000 lb./in.² and 40,000 lb./in.² respectively. These are specified as "low" and "high" interference respectively.

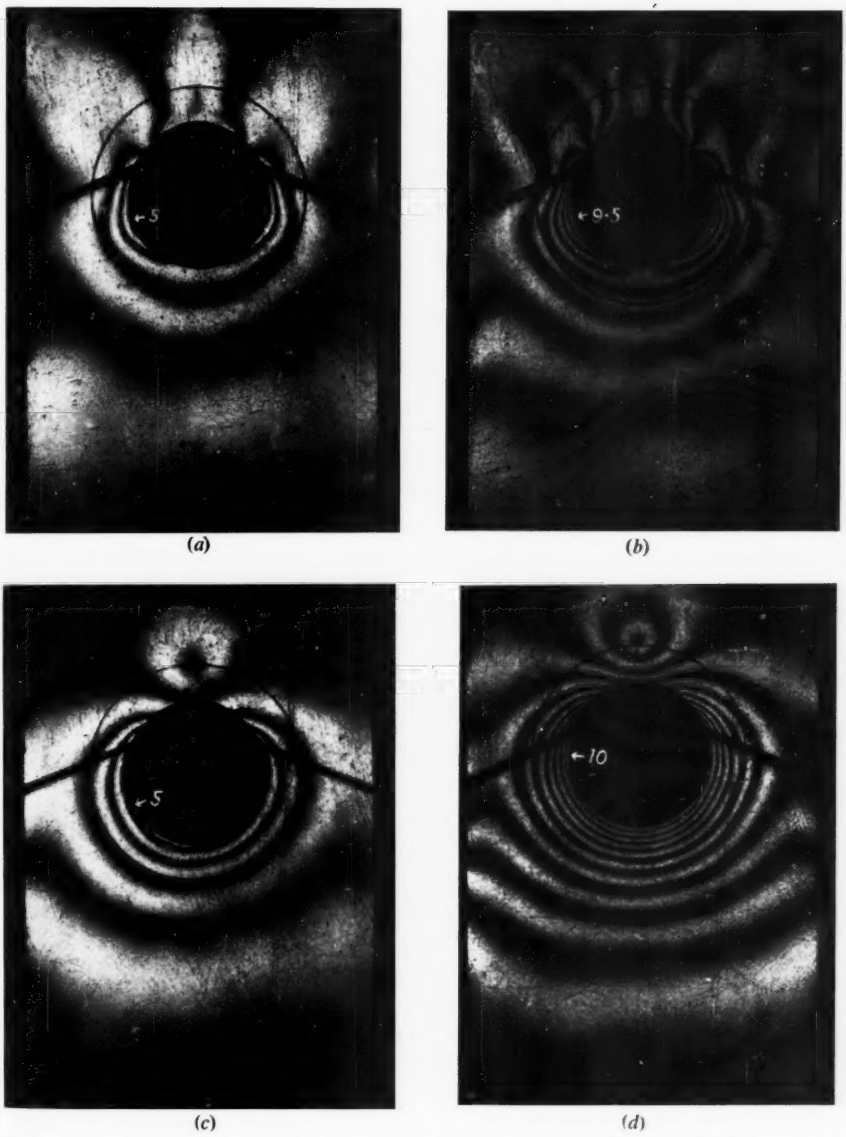

FIGURE 1. Typical fringe patterns in a plate with a $\frac{1}{8}$ in. diameter pin. The actual hole boundary is masked by the pin. The fringe numbers indicated are those on the boundary obtained by extrapolation along a normal to the boundary, the scribed $\frac{1}{2}$ in. diameter circle giving reference points for measurements.

(*a*) Push-fit, load 16×10^3 lb./in.^{2}
(*b*) Push-fit, load 32×10^3 lb./in.^{2}
(*c*) Low interference (0·003), load 16×10^3 lb./in.^{2}
(*d*) High interference (0·006), load 32×10^3 lb./in.^{2}

Facing page 148

For each degree of interference, a series of progressively increasing pin loads was applied, firstly with zero plate load and then with superimposed plate loads of three different magnitudes.

For each loading and pin-fit condition, the stresses at three points on the hole boundary were analysed. These points were: (*a*) on the horizontal diameter of the hole; (*b*) on the vertical diameter directly below the pin load, and (*c*) at the lower end of a diameter inclined at approximately 45° to the vertical.

The results of these tests are given in Tables I to V. The loads applied to the photoelastic model have been converted in these tables to loads which would produce the same strains in a light alloy plate, and the stresses in the model have been scaled up in proportion. Thus the tables give loads and stresses for a light alloy plate in which the degree of interference in the pin is the same as that in the photoelastic model.

3. The Stresses due to Pin Load Only

3.1. The Stress Distribution Around the Hole Boundary

Figure 1 shows photographs of typical fringe patterns, while Figs. 2 and 3 show respectively the distributions of shear stress and tensile stress around the hole boundary for two different loads at each degree of interference. The only separations of stresses carried out for the upper half of the hole boundary were those for the point on the vertical diameter in the cases of push-fit and high interference. The tensile stresses indicated by the dotted broken curves around the upper half of the hole boundary in Fig. 3, therefore, are only approximate, except for the four points indicated in Figs. 3(*a*) and 3(*c*). In the push-fit case lift from the pin occurs and the boundary stress (a compression one) is given directly by the fringe pattern. An examination of these figures gives the following results.

(*i*) *In the push-fit case* the maximum shear stress occurs at a point about 30° below the horizontal diameter, while the tensile stress has a much more pronounced maximum on the horizontal diameter. Thus the conditions at the point of maximum shear stress under the smaller of the two loads illustrated are

Shear stress	25×10^3 lb./in.^{2}
Circumferential tensile stress	37×10^3 lb./in.^{2}
Radial compressive stress	13×10^3 lb./in.^{2}

while at the horizontal diameter they are

Shear stress	23×10^3 lb./in.^{2}
Circumferential tensile stress	46×10^3 lb./in.^{2}
Radial stress (approximately)	0 lb./in.^{2}

Since in practice such a loaded lug never fails at a point below the horizontal section, it would appear that the small (8 per cent) decrease in shear stress at that section is more than offset by the 25 per cent increase in tensile stress.

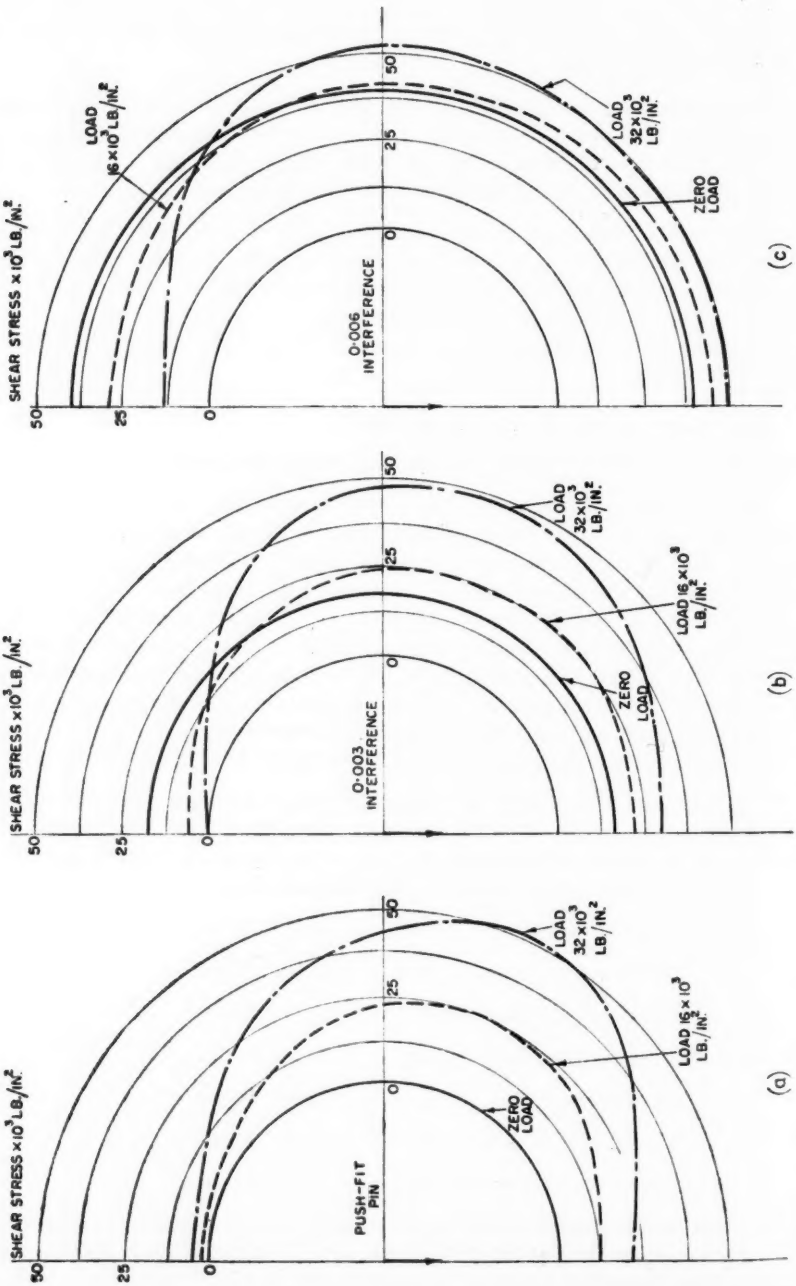

FIGURE 2. Distribution of shear stress around the hole boundary under loads applied to the pin. (4 in. diameter hole in 1 in. wide plate)

FIGURE 2. Distribution of shear stress around the hole boundary under loads applied to the pin. ($\frac{1}{2}$ in. diameter hole in 1 in. wide plate)

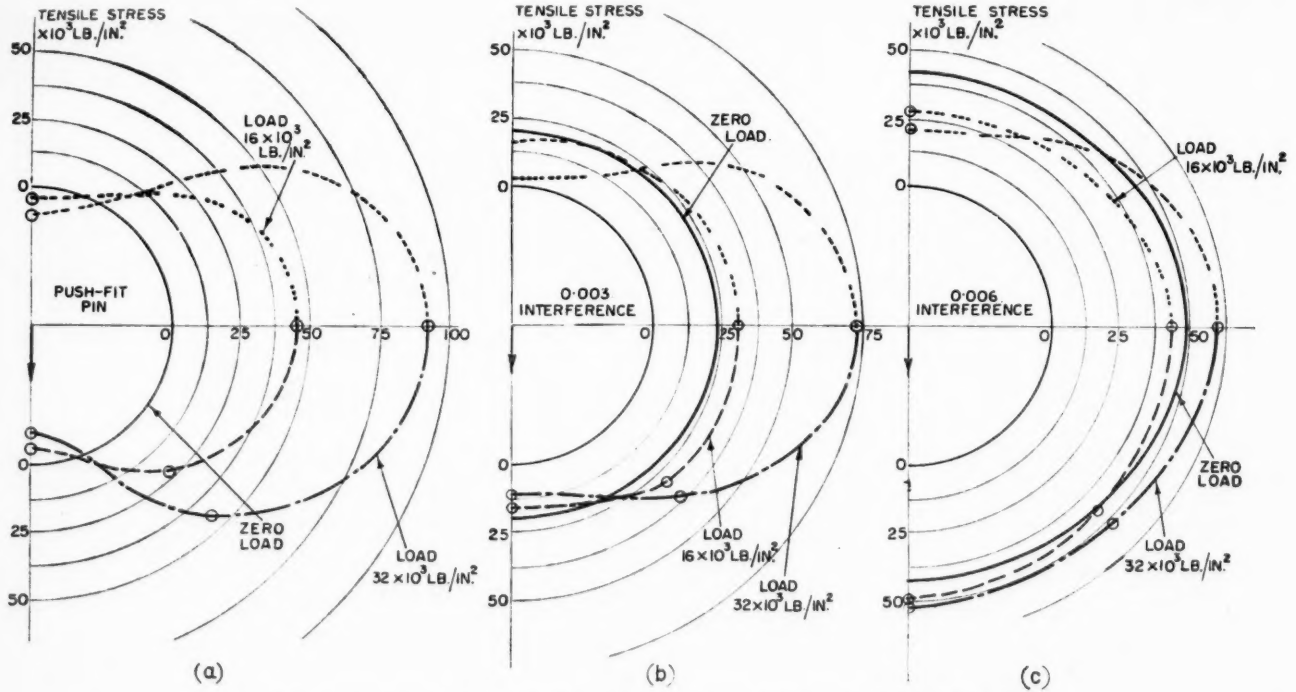

FIGURE 3. Approximate distribution of tensile stress around hole boundary under loads applied to the pin.
($\frac{1}{2}$ in. diameter hole in 1 in. wide plate. ○ signifies value calculated from photoelastic data)

(*ii*) *With low interference* and high load the stress distribution characteristics are similar to those in the push-fit case, but under low load both tensile and shear stresses tend to maintain almost constant values around a large section of the hole boundary, the maximum shear stresses having nearly the same values as in the push-fit case (*see* Figs. 1(*a*) and 1(*c*)), while the tensile stresses are considerably lower. With the two loads illustrated, the circumferential stresses remain tensile all round the boundary.

(*iii*) *With high interference* under both high and low loads the stresses, both shear and tensile, are very nearly constant around the greater part of the circumference, only falling towards the top of the hole. At the extremity of the horizontal diameter the shear stresses are somewhat higher than in the push-fit case, but the tensile stresses are lower, the differences in each case being greater under the lower load. The relative magnitudes of the shear stresses are shown by the fringe numbers in Figs. 1(*b*) and 1(*d*).

3.2. The Effect of Interference upon the Shear Stresses

Tables I, II and III give the shear stresses at the three points investigated for the whole range of loading for the two pin sizes. The results for pin load only have been taken from the appropriate columns of these tables.

It may be noted that, in this case, the circumferential stress becomes compressive at both the top and bottom of the hole. At the top of the hole "lift" of the plate from the pin will occur at all loads and there will be regions of very small radial contact pressure in the upper half of the periphery at which slip and consequent fretting will occur.

TABLE I

SHEAR STRESSES ON HORIZONTAL SECTION
(Unit = 10^3 lb./in.^{2})

$\frac{1}{4}$ *in. Diameter Hole*

Pin Load	*Push-Fit Pin*				*Low Interference* (0·003)				*High Interference* (0·006)			
	Plate Load				*Plate Load*				*Plate Load*			
	0	13·3	26·7	40·0	0	13·3	26·7	40·0	0	13·3	26·7	40·0
0	0	17	34	50	20	25	36	53	40	41	50	63
6·7	13	28	44	62	21	33	51	66	40	44	56	77
13·3	26	40	55	75	28	45	65	80	41	50	65	90
20·0	40	50	69	90	39	60	78	96	44	58	78	100
26·7	53	60	85	105	54	78	90	110	50	70	95	110

$\frac{3}{8}$ *in. Diameter Hole*

Pin Load		*Plate Load*				*Plate Load*				*Plate Load*		
	0	16·0	32·0	48·0	0	16·0	32·0	48·0	0	16·0	32·0	48·0
0	0	19	38	55	20	25	40	50	40	42	50	57
8·0	11·5	30	50	66	21	31	47	65	41	44	55	67
16·0	23	43	60	78	25	41	62	80	43	46	60	77
24·0	34	55	72	89	34	55	75	94	47	54	70	88
32·0	46	65	84	100	48	68	88	106	53	68	80	100

TABLE II

SHEAR STRESSES ON 45° SECTION

(Unit = 10^3 lb./in.^{2})

¼ in. Diameter Hole

Pin Load	Push-Fit Pin				Low Interference (0·003)				High Interference (0·006)			
	Plate Load				Plate Load				Plate Load			
	0	13·3	26·7	40·0	0	13·3	26·7	40·0	0	13·3	26·7	40·0
0	0	7	14	20	20	20	24	28	40	39	40	41
6·7	15	19	23	30	23	22	35	40	42	40	43	48
13·3	30	31	32	40	30	31	48	53	45	45	48	55
20·0	45	43	43	48	38	47	61	65	50	52	55	64
26·7	60	50	55	55	49	60	70	78	52	62	62	73

⅜ in. Diameter Hole

Pin Load	Plate Load				Plate Load				Plate Load			
	0	16·0	32·0	48·0	0	16·0	32·0	48·0	0	16·0	32·0	48·0
0	0	6	12	18	20	20	20	28	40	40	40	40
8·0	11	18	20	26	22	22	22	34	42	41	41	43
16·0	23	25	28	35	26	25	30	40	45	44	43	48
24·0	35	35	38	43	33	34	40	45	47	46	46	54
32·0	46	47	48	52	43	45	50	51	50	50	50	60

TABLE III

SHEAR STRESSES ON VERTICAL SECTION

(Unit = 10^3 lb./in.^{2})

¼ in. Diameter Hole

Pin Load	Push-Fit Pin				Low Interference (0·003)				High Interference (0·006)			
	Plate Load				Plate Load				Plate Load			
	0	13·3	26·7	40·0	0	13·3	26·7	40·0	0	13·3	26·7	40·0
0	0	−6	−13	−19	20	15	8	4	40	34	25	18
6·7	9	3	2	1	22	17	19	14	43	35	30	23
13·3	18	12	13	12	27	24	30	24	46	40	36	30
20·0	27	21	22	18	33	36	39	33	50	47	43	39
26·7	36	28	30	24	41	55	48	42	52	55	52	51

⅜ in. Diameter Hole

Pin Load	Plate Load				Plate Load				Plate Load			
	0	16·0	32·0	48·0	0	16·0	32·0	48·0	0	16·0	32·0	48·0
0	0	−5	−10	−15	20	12	7	4	40	35	25	16
8·0	6	4	2	0	21	15	9	8	42	36	27	18
16·0	11	12	9	8	22	19	14	13	45	37	30	22
24·0	17	20	14	14	25	24	21	17	48	40	33	26
32·0	23	26	20	20	30	29	26	22	50	43	37	30

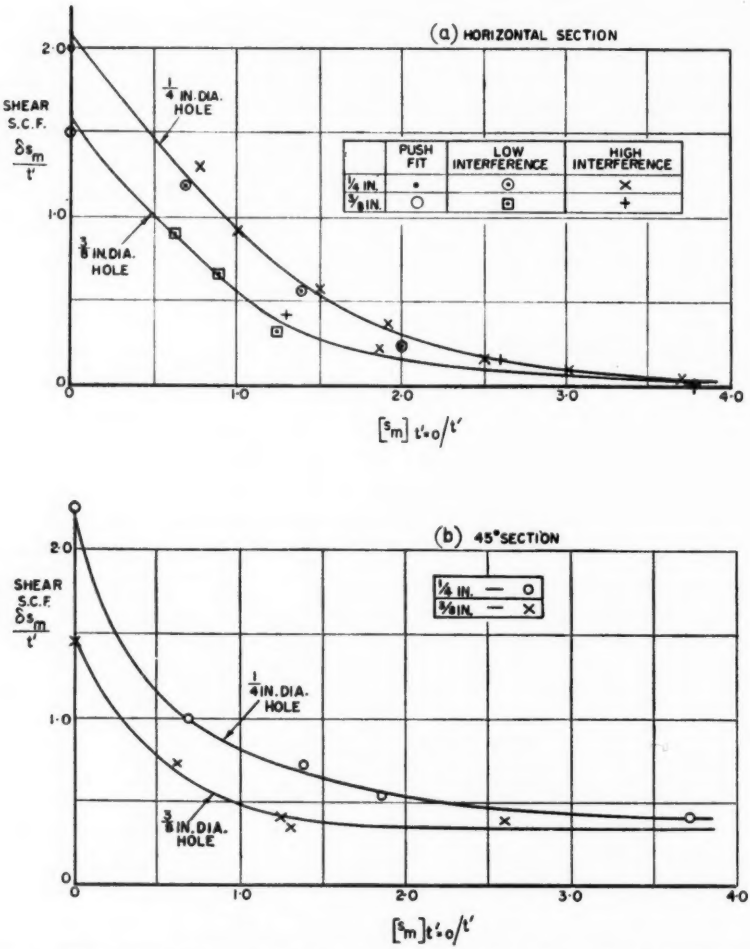

FIGURE 4. Shear stress concentration factors under pin load, (*a*) on the horizontal section, (*b*) on the 45° section, for $\frac{1}{4}$ in. and $\frac{3}{8}$ in. diameter holes.

As for the plate load[4], the effect of the interference is found to be directly related to the ratio of interference stress to applied tension, and can best be illustrated by graphs of the stress concentration factor plotted against this ratio. Figure 4 shows such graphs for the shear stresses, (*a*) on the horizontal section, and (*b*) on the 45° section.

The reduction in S.C.F. is, of course, offset to some extent by the initial interference stresses, but the net result may be shown on a graph of maximum total stress as a function of applied tension. Figure 5 shows this graph for the $\frac{1}{4}$ in.

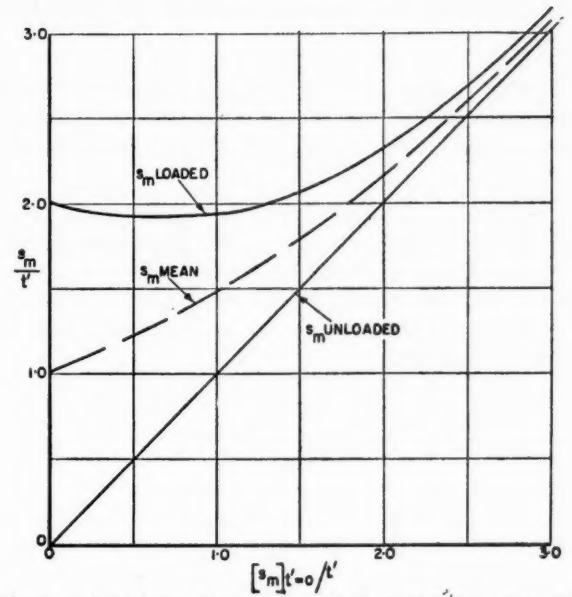

FIGURE 5. Maximum and minimum shear stresses on the horizontal section when the applied pin load alternates between zero and a given value t'. Hole diameter $\frac{1}{4}$ in.

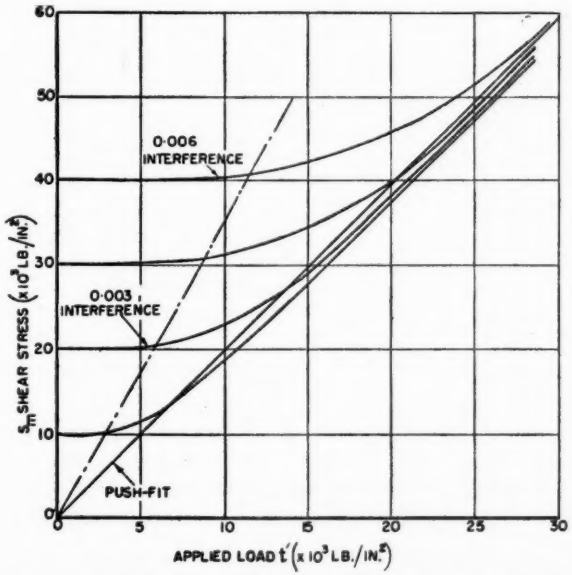

FIGURE 6. Peak shear stresses on the horizontal section for various degrees of interference under pin load. Hole diameter $\frac{1}{4}$ in. The broken line denotes the estimated limits of load for which the stress concentration factors under reversed load will have the same values as for positive load. (*See* Section 5 (*iii*).)

(The interference figures given are those for a steel pin in a light alloy plate. For a light alloy pin the interference to give the same initial stress will be approximately 4/3 of that in a steel pin)

diameter hole. The straight line in this figure represents the initial interference stress, and the graph is designed to show the mean stress level and the amplitude of stress oscillations when the load on the pin alternates between zero and a given fixed value.

For the general case in which there is a mean tensile load on which an alternating load is superimposed, a more useful way of presenting the results is illustrated in Fig. 6. Using one of the S.C.F. curves of Fig. 4, curves of peak stress against applied tension are deduced for various values of interference and, from these, it is a simple matter to read the mean value and the amplitude of the stress for any given loading conditions.

TABLE IV

TENSILE STRESSES ON HORIZONTAL SECTION

(Unit = 10^3 lb./in.^{2})

¼ in. Diameter Hole

Pin Load	*Push-Fit Pin*			*Low Interference* (0·003)			*High Interference* (0·006)		
	Plate Load			*Plate Load*			*Plate Load*		
	0	13·3	26·7	0	13·3	26·7	0	13·3	26·7
0	0	26	52	23	32	49	44	46	51
13·3	53	75	—	32	70	—	39	60	—
26·7	106	—	145	81	—	160	36	—	150

⅜ in. Diameter Hole

Pin Load	*Plate Load*			*Plate Load*			*Plate Load*		
	0	16·0	32·0	0	16·0	32·0	0	16·0	32·0
0	0	26	52	23	27	40	48	48	51
16·0	46	74	—	27	57	—	43	54	—
32·0	92	—	150	67	—	115	57	—	120

TABLE V

TENSILE STRESSES ON 45° SECTION

(Unit = 10^3 lb./in.^{2})

¼ in. Diameter Hole

Pin Load	*Push-Fit Pin*			*Low Interference* (0·003)			*High Interference* (0·006)		
	Plate Load			*Plate Load*			*Plate Load*		
	0	13·3	26·7	0	13·3	26·7	0	13·3	26·7
0	0	3	6	20	20	19	40	40	40
13·3	28	15	—	28	20	—	42	40	—
26·7	56	—	30	39	—	35	41	—	40

⅜ in. Diameter Hole

Pin Load	*Plate Load*			*Plate Load*			*Plate Load*		
	0	16·0	32·0	0	16·0	32·0	0	16·0	32·0
0	0	2	5	20	20	20	40	40	40
16·0	21	15	—	29	20	—	43	40	—
32·0	42	—	30	36	—	30	53	—	40

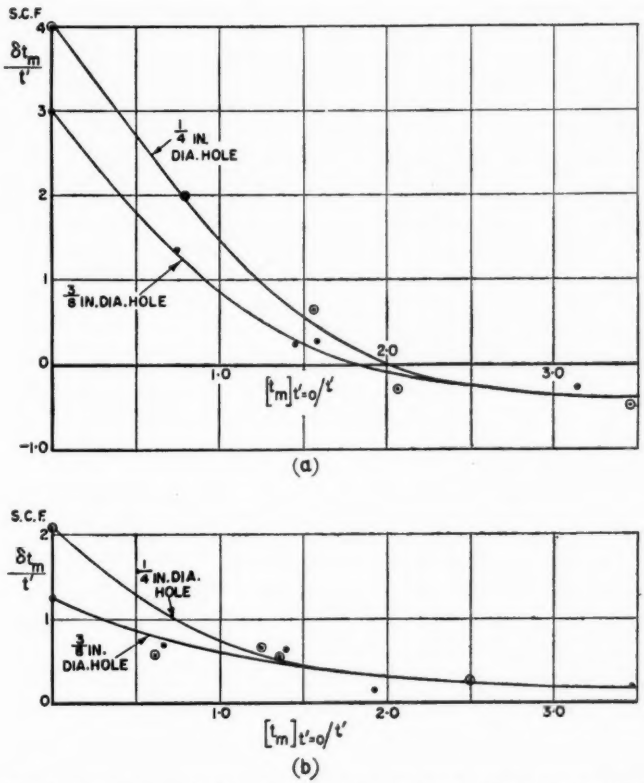

FIGURE 7. Tensile stress concentration factors under pin load, (*a*) on the horizontal section, (*b*) on the 45° section, for $\frac{1}{4}$ in. and $\frac{3}{8}$ in. diameter holes.

3.3. THE EFFECT OF INTERFERENCE ON THE TENSILE STRESSES

Separation of the stresses was carried out for a limited number of load conditions and the tensile stresses obtained on the horizontal and 45° sections are given in Tables IV and V.

The accuracy of these results is not as high as that of the shear stresses, especially for the 45° section, where the isoclinic fringes in the photoelastic model were frequently not well defined. The scatter in the S.C.F. graphs of Figs. 7(*a*) and 7(*b*) indicates, however, maximum divergences of the order of 15 per cent of the highest stress.

Figure 8 shows the graphs of maximum and minimum tensile stress on the horizontal section for a $\frac{3}{8}$ in. diameter hole under application and removal of load. A reversal of sign of the S.C.F. for a high ratio of interference to load is indicated by the crossing over of the two curves. This reversal, which indicates a reduction in tensile stress on the boundary with the addition of a tensile load, might appear

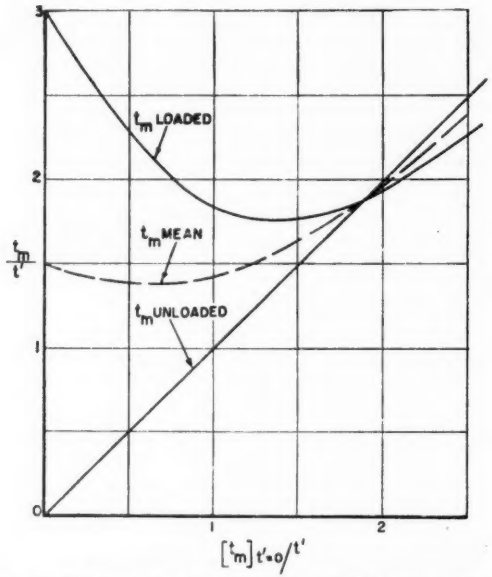

FIGURE 8. Maximum and minimum tensile stresses on the horizontal section when the applied pin load alternates between zero and a given value t'. Hole diameter $\frac{3}{8}$ in.

at first sight to be impossible, but if we postulate an interference great enough to prevent relative motion of the pin and plate surfaces, then it can be seen that either a small vertical compressive strain in the pin at this point or a small increase in the normal pressure between the surfaces will require a vertical compressive strain in the plate to maintain the contact conditions.

4. The Stresses under Combined Pin and Plate Loads

The figures of Tables I, II, IV and V, deduced from the individual photoelastic observations, were first analysed to check their consistency. The stresses were plotted against load (*a*) for varying pin loads at each plate load, and (*b*) for varying plate loads at each pin load. Smooth curves were then drawn which gave the best "fits" to the plotted points, while keeping the readings of corresponding points on the two sets of curves identical.

All the shear stresses on the horizontal section gave equally good curves, with divergencies of the same order as in Fig. 9. The divergencies of the shear stresses on the 45° section and the tensile stresses on both sections were somewhat greater than these.

Figure 10 shows maximum shear stress values on the horizontal section for various proportions of pin and plate load. The greatest number of observations was available for the case of equal pin and plate loads, and these are found to lie sensibly mid-way between the pin and plate load curves. To the same degree of

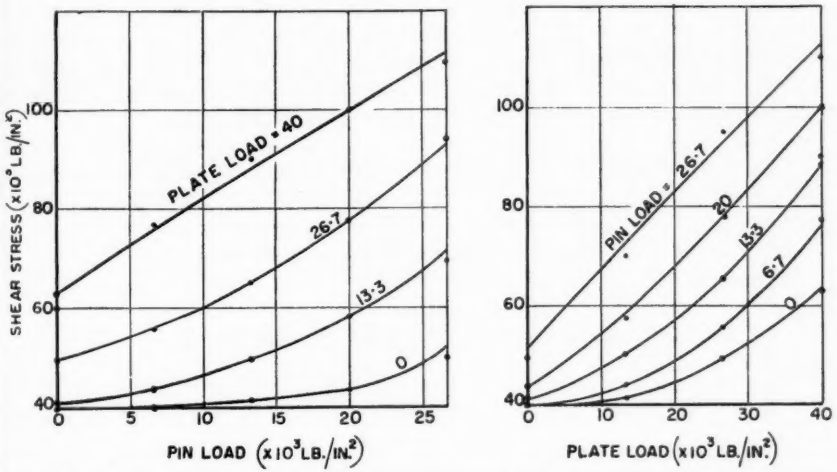

FIGURE 9. Graphs of shear stress on the horizontal section under increasing pin and plate loads, showing the small adjustments needed to produce smooth curves giving consistent values of the stress under all load conditions.
(Taken from Table I for $\frac{1}{4}$ in. diameter hole and 0·006 interference)

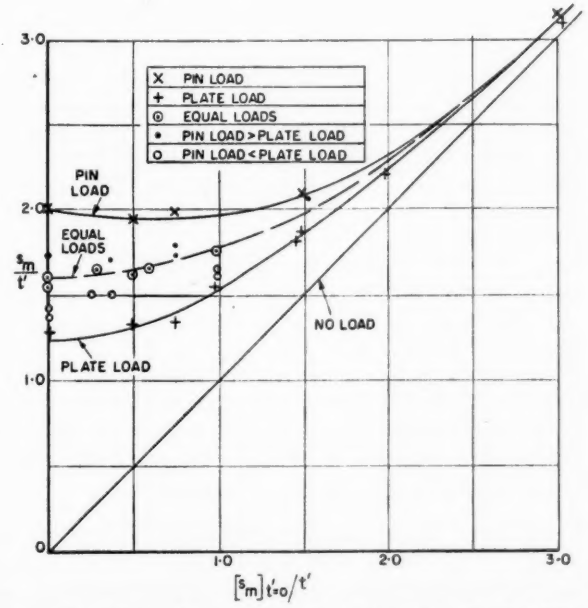

FIGURE 10. Values of maximum shear stress on the horizontal section for different proportions of pin and plate load. Hole diameter $\frac{1}{4}$ in.

accuracy the other observations divide the range in the inverse ratio of the proportions of pin to plate load. This proportional sharing of the total stress is found for both shear and tensile stresses on the horizontal section. Thus, under equal pin and plate loads t', the stresses with any degree of interference will be the means of those for pin and plate loads each of $2t'$ with the same interference.

The stresses on the 45° section do not follow this pattern. The curve for equal pin and plate loads lies much nearer to the plate load curve, and this effect is even more marked in the tensile stresses. Thus the effect of superposing a plate load is to reduce the effective S.C.F. of the pin load for the 45° section.

5. Applicability of Results to Practical Problems

(*i*) All the results obtained relate to an elastic distribution of stress. In cases where the elastic limit of the material is exceeded, the peak stresses indicated in these tests may not be reached, but the assumption is made that endurance under fatigue is dependent upon the peak stresses which would have been reached if local plastic yield had not occurred.

(*ii*) No account is taken of the effect of fretting, which may be an important factor, especially in cases of low interference-load ratios.

(*iii*) The results are not necessarily directly applicable in cases of reversal of sign in the applied load. It seems probable that, so long as the interference-load ratio is high, the contact conditions will not alter seriously with reversed loading and there will always be a reserve of radial compression allowing of the transmission of tensions across the hole boundary. In that case the stress-concentration factors under reversed loading should be the same, leading to load stresses of the same magnitude but opposite sign. For low interference-load ratios, however, where "lift" from the pin tends to occur under tension, the S.C.F.'s under reversed loads will be entirely different.

Thus in the graphs of peak stress shown in Fig. 6, the curves may be continued beyond the vertical axis in inverted form for a limited distance. The broken line represents an estimate of the range within which the interference-load ratio is high enough to justify this.

(*iv*) Within the limitations imposed by the factors mentioned in (*ii*) and (*iii*), the results obtained should help the designer to estimate the endurance of joints containing interference-fit pins, or to determine the degree of interference which will give maximum endurance under given loading conditions.

(*v*) It is hoped also that these results will be of value in investigations into the basic causes of fatigue failure at bolt and rivet holes. With much more precise information than has hitherto been available on the peak stresses in such features, it should be possible to devise fatigue tests to explore systematically the separate effects of the various factors affecting fatigue failure.

ACKNOWLEDGMENTS

The authors wish to express their indebtedness to Professor H. John Collins of the Department of Civil and Municipal Engineering at University College, London, for providing facilities for the photoelastic investigation, and to the staff of the Technical Department of the Royal Aeronautical Society for help in the preparation of the diagrams.

Appendix

Another method of presenting the results on interference fits has been proposed by H. L. Cox. In this method, charts are drawn which show the ratios of mean stress and stress range with different degrees of interference to the corresponding stresses with a push fit. These charts enable the designer to predict the fatigue endurance of interference-fit joints from fatigue data on similar joints with push-fit pins.

Separate charts are needed for plate load and pin load, and each chart applies strictly only to a given ratio of mean load to load range. The variation of the stress ratios with the load ratios, however, is very small over a considerable range, and charts for three different values of load ratio should be sufficient to cover the range of loading conditions normally occurring in aircraft practice.

Two such charts are shown in Figs. 11 and 12. These were prepared at the National Physical Laboratory, Ph.(E) Division, by A. F. C. Brown and A. G. Cole, who also carried out the additional photoelastic tests to provide data for the $\frac{1}{8}$ in. and $\frac{1}{2}$ in. diameter holes under pin load. The authors are indebted to Messrs. Cox, Brown and Cole for permission to include the charts in this paper.

The notation used in the charts is as follows:—

t plate thickness (in.)

D plate width (in.)

d pin diameter (in.)

P tensile load applied to plate (lb.)

P_{max} maximum tensile load applied to plate (lb.)

P_{min} minimum tensile load applied to plate (lb.)

M mean tensile load applied to plate, $=\frac{1}{2}(P_{max}+P_{min})$ (lb.)

R stress ratio, $=(P_{min}/P_{max})$

f average tensile stress across net area of plate due to mean tensile load, $=M/\{(D-d)\,t\}$ (lb./in.^{2})

q shear stress at transverse boundary of hole caused by applied load P with push-fit pin (lb./in.^{2})

q' shear stress at transverse boundary of hole caused by applied load P with interference-fit pin (lb./in.^{2})

q_0' shear stress at transverse boundary of hole caused by interference only (lb./in.^{2})

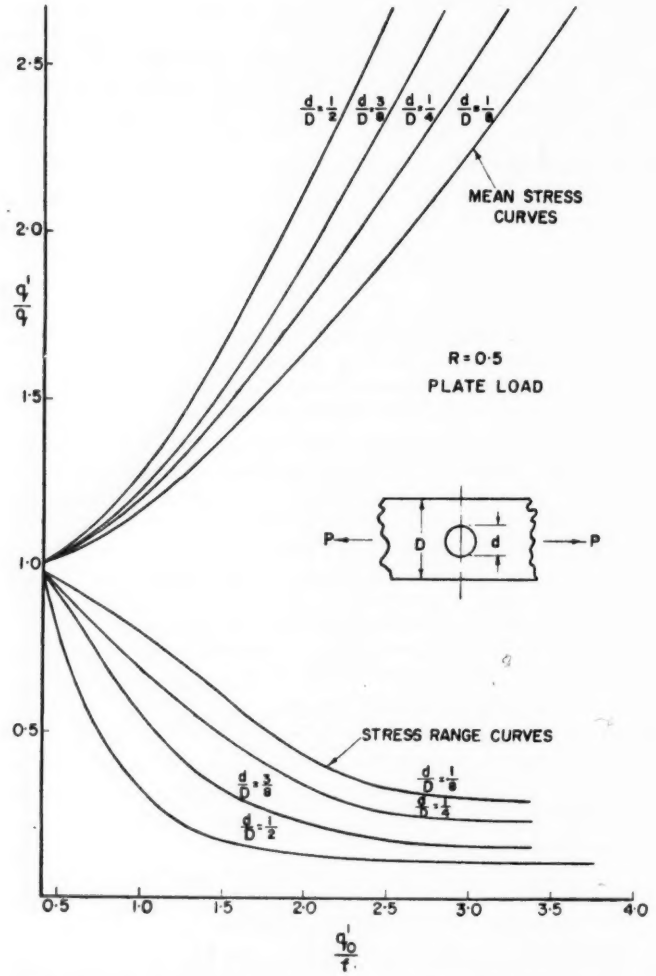

FIGURE 11. Ratios of mean stress and stress range on the horizontal section with different degrees of interference to corresponding stresses with a push-fit pin, under an oscillatory plate load whose minimum value is 0·5 of its maximum.

REFERENCES

1. WILKINS, E. W. C. and JESSOP, H. T. A Photoelastic-Fatigue Programme of Experimental Research in Connection with Bolted Joints. *Journal of the Royal Aeronautical Society*. June 1954.

2. JESSOP, H. T., SNELL, C. and JONES, I. Results of Photoelastic Investigation of Stresses in a Tension Bar with Unfilled Hole. *Journal of the Royal Aeronautical Society*, January 1955.

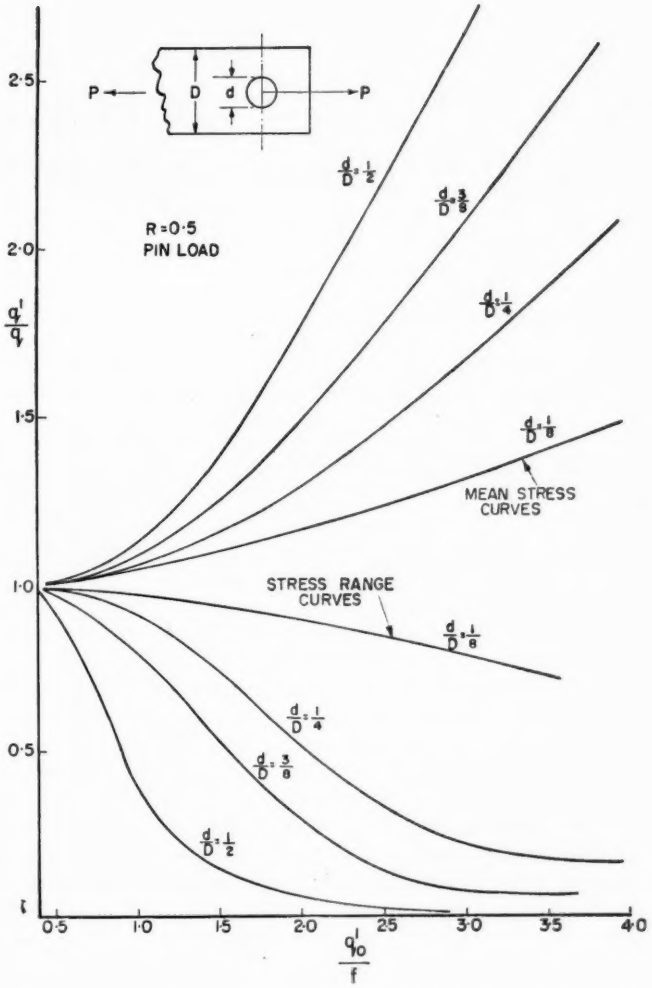

FIGURE 12. Ratios of mean stress and stress range on the horizontal section under oscillatory pin load.

3. JESSOP, H. T., SNELL, C. and HOLISTER, G. S. Photoelastic Investigation in Connection with the Fatigue Strength of Bolted Joints (Tension Bar with Hole having a Push-Fit Pin with Load applied to Plate only). *The Aeronautical Quarterly*, August 1955.

4. JESSOP, H. T., SNELL, C. and HOLISTER, G. S. Photoelastic Investigations on Plates with Single Interference-Fit Pins with Load Applied to Plate Only. *The Aeronautical Quarterly*, November 1956.

The Shock Pattern of a Wing-Body Combination, Far from the Flight Path

F. WALKDEN

(*The University, Manchester*)

SUMMARY: The position and strength of the front shock wave at large distances from a wing-body combination, are deduced from the linear theory for the combination, using a method developed by Whitham. The combination consists of a body of revolution and a wing which has thickness and is lifting. The effects of interference between the flow over the body and the flow over the wing are included. In any direction the flow far from the wing-body combination is equivalent to the flow past a body of revolution determined from the configuration of the combination. The modified formulae for unsteady flow are given and some results are evaluated for the combination of a body of revolution and a delta wing with subsonic leading edges.

1. Introduction

This paper is a contribution to the theory of the shocks produced by aircraft and missiles in supersonic flight. In recent papers by Whitham[1,2] a method has been developed for deducing this information in certain cases from the linear theory of the disturbance produced in the air. In Whitham's first paper this method is applied in detail to a body of revolution in uniform motion, and the second paper includes the extension to a thin symmetrical wing in uniform motion. Rao[3] has shown how the method can be extended to deal with the non-uniform motion of a body of revolution.

Here it is intended to investigate the flow far from a general wing-body combination which is moving with supersonic speed. It is assumed that the body is axi-symmetric, with the main stream direction as axis of symmetry; the wing may be inclined at a small angle to the main stream. In the first instance uniform motion is assumed, so that the problem can be treated in the steady state. However, the further extension used by Rao to obtain the results for non-uniform motion from those for steady motion can still be applied. For the sake of simplicity, attention is concentrated on the flow at large distances, but it should be noted that for some body shapes the theory gives results at all distances from the body surface.

Received March 1957.

For the steady-flow problem, cylindrical polar co-ordinates (r, θ, x) are introduced, with origin at the intersection of the leading edge of the wing and the axis of symmetry of the body; the axis of symmetry of the body is also the axis of x.

Let $U_\infty \phi$ be the velocity potential of the disturbance. From the linear theory it is found that, far from the body, ϕ takes the approximate form

$$\phi = \frac{f(x - Br, \theta)}{\sqrt{(2Br)}} \quad . \quad . \quad . \quad . \quad . \quad . \quad (1)$$

In equation (1), $B = \sqrt{(M_\infty^2 - 1)}$, where M_∞ is the Mach number of the main stream.

This potential is made up of contributions from the body alone, the wing alone, and the interference potential. All these contributions take the same form at large distances. This is in accordance with the theory of geometrical acoustics; as the disturbance spreads out from the body the total energy flux remains constant and, since the area is increasing proportionally to r, the amplitude falls off like $1/\sqrt{r}$, as for cylindrical waves.

The function f gives the initial profile of these waves and it is determined by the shape of the body.

The method of finding the shocks from equation (1) follows the standard procedure explained by Whitham. Briefly, the flow in each plane $\theta =$ constant is treated separately; the flow in such a plane may be interpreted as being due to an equivalent body of revolution and the theory can be developed as for a body of revolution. A more involved treatment is necessary to determine the shocks at all distances; the simplification applies only at large distances.

Rao[3] verified that, for a body of revolution, the function f for unsteady motion is the same as the function for uniform motion. The effect of non-uniform motion of the body appears in the amplitude factor, which governs the way in which the disturbance decays with distance from the body.

Whitham found the dependence of f on θ for a thin symmetrical wing. The investigation will be completed here by finding f for general wing-body combinations and then applying it to a study of the shock waves.

For a body of revolution f is determined as a certain integral involving $S(x)$, the area distribution of the body. For the symmetrical wing f depends in the same way upon a function $S(x)$, which is found by integrating the thickness distribution of the wing plan form; the choice of lines depends upon the direction being considered.

For the anti-symmetrical problem, it will be shown that f is a similar integral involving the lift distribution over the wing plan form. The lift distribution can be obtained in terms of the wing shape by standard methods[4].

For a winged body the perturbation potential in the linear theory is the sum of the potentials of the wing and body considered separately, together with an interference potential; this interference potential arises from the effects of the interaction between the two flows.

Chester[5] has studied the problem of interference. At large distances the main contribution is from a term which is equivalent to a distribution of sources along the axis of the body; the strength of this source distribution is proportional to the mean of $\partial\phi_w/\partial r$ taken over the body surface. $U_\infty\phi_w$ is the perturbation potential of a two-dimensional wing whose profile is equal to the profile of the centre section of the given wing. The derivation of this term is different from Chester's method and is included in Section 2.

In a private communication, Warren has considered the effect of lift on shock waves. He represents the effect of lift as that of a distribution of doublets along the axis; he chooses the strength of the doublet distribution to get a realistic total lift (although this leads to an impossibly large incidence for the body of revolution which is his model) and obtains plausible results for the shock wave behaviour.

The method used in this paper gives the same kind of result, except that the variation of shock strength with direction is not the $\sin\theta$ variation which Warren is forced to get as a result of his choosing to represent the lift as a distribution of doublets along the axis.

If the aircraft or missile is accelerating along a straight path, the amplitude factor in equation (1) is modified and, further, if the path is not straight this modification to the amplitude factor will also depend upon θ. Rao[3] studied this and a brief account of his work, together with its application to a general winged body, is contained in Section 4.

NOTATION

r, θ, x cylindrical polar co-ordinates

x, y, z Cartesian co-ordinates

U_∞ main stream velocity

M_∞ Mach number of the main stream

M local Mach number. In Section 4, M represents the flight Mach number of the body

μ Mach angle

$U_\infty\mu$ perturbation to the main stream velocity in the main stream direction

$B = \sqrt{(M_\infty^2 - 1)}$

a_∞ sound speed in the main stream

ε local direction of flow

γ ratio of specific heats

$H_1(x)$ Heaviside unit function

$R(x)$	radius distribution of the body of revolution
$S(x)$	area distribution of the body of revolution
S_1, S_2, S_3, S_4	area distributions of certain "equivalent" bodies of revolution
d	distance of the wing behind the body of revolution
$Z(x, y)$	thickness distribution of the wing
$h(x) = Z(x, 0)$	
$Z_x(x, y) = \partial Z(x, y)/\partial x$	
α	angle of incidence of the wing
$K_0, K_1, \ldots K_n \ldots$	Bessel functions of the second kind with imaginary argument
p	Heaviside operator; p also represents the local pressure
p_∞	main stream pressure
ρ_∞	density of the main stream
$(p - p_\infty)/p_\infty$	excess pressure ratio
$H(p)$	Heaviside operational representation of $h(x)$
$U_\infty\phi$	a perturbation potential
$U_\infty\phi_w$	the perturbation potential of a two-dimensional wing
$U\Phi_I$	the perturbation potential of interference effects
f, F	functions used to describe the disturbance generated by the wing-body combination
G	function defined by equation (38)
$\tau(x, r)$	describes the characteristic curves
$T(x, r)$	describes the front shock wave
$(l(\eta), \eta)$	the parametric representation of a point on the supersonic leading edge of the wing
χ	the angle between the plane of the wing and the plane through $(l(\eta), \eta)$ which is normal to the wave front
s	In Section 3, s measures distance from the wing in the plane through $(l(\eta), \eta)$ which is normal to the wave front In Section 4, s represents the distance along a ray
α, β	distance in the x-, y-directions measured from $(l(\eta), \eta)$
$\Delta p/(\frac{1}{2}\rho_\infty U_\infty^2)$	local lift coefficient
κ	curvature of the path described by the body (Section 4)
x', y', t	variables of integration. In Section 4, t also represents time
K, E	complete elliptic functions of the first and second kind.
a, b, c	used to describe the shape of the wing plan forms in Section 5
$m = c/a$	

2. The Linear Theory

As explained in Section 1, we start with the steady-flow problem; these results will be extended to non-uniform motion later. First the body and wing are treated separately, then these results are added, and finally the interference effects are included.

Let the main stream velocity be U_∞ in the x-direction, and let $U_\infty \phi(x, y, z)$ be the potential of small perturbations to the main stream. The function ϕ must satisfy the partial differential equation

$$\nabla^2 \phi = M_\infty^2 \phi_{xx}, \qquad (2)$$

ϕ also satisfies appropriate boundary conditions on the body.

For a body of revolution which has an area distribution $S(x)$, and which is at zero incidence to the stream, the appropriate solution of (2) is

$$\phi(x, r) = \frac{-1}{2\pi} \int_0^{x-Br} \frac{S'(t)}{\sqrt{[(x-t)^2 - B^2 r^2]}}\, dt, \qquad (3)$$

where the dash denotes differentiation with respect to t. This expression can be interpreted as giving the perturbation potential of a distribution of supersonic sources of strength $U_\infty S'(t)$ which lie along the axis of the body of revolution. That the strength of the source distribution is $U_\infty S'(t)$ can be deduced directly from the boundary condition at the body surface. This condition is $(\partial\phi/\partial r)_{r=R} = R'(x)$, where $R(x)$ is the body radius.

Alternatively, the total change in flux due to the presence of the body must be $U_\infty \delta S$, where δS is the change in cross-sectional area. Hence $U_\infty \delta S/\delta x = 2\pi U_\infty RR'$ must be the source strength which satisfies the boundary condition at the body surface.

The velocity potential for small perturbations due to a thin wing is the sum of the perturbation potential for a certain thickness problem and the perturbation potential for the problem of a flat plate at incidence to the stream. The thickness problem is symmetrical and the solution can be represented as being the potential due to a distribution of sources over the wing plan form; as for a body of revolution, the source strength is determined from the boundary conditions at the wing surface.

For a symmetrical wing, whose plan form lies in the x, y-plane, the potential of the appropriate source distribution is

$$U_\infty \phi(x, y, z) = -\frac{U_\infty}{\pi} \iint \frac{Z_x(x', y')}{\{\sqrt{(x-x')^2 - B^2(y-y')^2 - B^2 z^2}\}^{\frac{1}{2}}}\, dx'dy'. \qquad (4)$$

The source strength is $2U_\infty Z_x(x, y)$, where $Z(x, y)$ is the thickness distribution of the wing and $Z_x(x, y) = \partial Z(x, y)/\partial x$. (x, y, z) is a right-handed system of Cartesian

co-ordinates. The double integration is over the part of the wing plan form which lies within the region $(x-x')^2 \geqslant B^2(y-y')^2 + B^2z^2$.

The flat plate at incidence is equivalent to a certain distribution of elementary horseshoe vortices over the wing plan form. The perturbation potential due to this vortex distribution is

$$U_\infty \phi(x, y, z) = \frac{U_\infty}{4\pi} \int\int \frac{z(x-x')}{(y-y')^2 + z^2} \frac{1}{\sqrt{[(x-x')^2 - B^2(y-y')^2 - B^2z^2]}} \frac{\Delta p(x', y')}{\frac{1}{2}\rho_\infty U_\infty^2} dx'dy' \quad (5)$$

The strength of an elementary horseshoe vortex depends upon the local lift coefficient $\Delta p/(\frac{1}{2}\rho_\infty U_\infty^2)$. The range of integration is that part of the wing plan form which lies within the region $(x-x')^2 \geqslant B^2(y-y')^2 + B^2z^2$.

The perturbation potential for a thick lifting wing is the sum of expressions (4) and (5).

If the combination of a body of revolution and a thick symmetrical wing at an angle of incidence is considered, the perturbation potential of the combination is the sum of the potentials due to the wing and body when separated, together with an interference potential. The interference potential corrects for the effect of either component at the boundary of the other. The interference effects of the body on the wing are $O(R^2h \log R)$, where h is the wing thickness and R the body radius. This contribution to the interference potential is small and will be neglected. The effects of interference will be localised; they arise mainly from the interaction between the flow over that part of the wing close to the body and the flow over the body.

In this region the wing is effectively two-dimensional. For a symmetrical wing the central section of the wing is given by $z = -\alpha x \pm h(x)$, where α is the angle of incidence of the wing. The contribution of the incidence part to the potential can be shown to be at most $O(\alpha R^2)$, which is small. Thus the main contribution to the interference potential arises from correcting for the effect of the flow over the wing at zero incidence at the surface of the body.

In the upper half-plane the potential field for the two-dimensional wing is given by

$$\phi_w = -\frac{1h}{B}(x - Bz).$$

The component of velocity normal to the surface of the body due to this potential field is given by

$$\sin\theta h'(x - BR\sin\theta).$$

The wings lie in the planes $\theta = 0$ and $\theta = \pi$. Here $R = R(x)$ describes the surface of the body and $h'(x) = dh(x)/dx$. It is now necessary to find an interference potential Φ_I which will cancel this normal component of velocity on the body.

In cylindrical polar co-ordinates equation (2), which Φ_I must satisfy, becomes

$$\frac{\partial^2\Phi_I}{\partial r^2}+\frac{1}{r}\frac{\partial\Phi_I}{\partial r}+\frac{1}{r^2}\frac{\partial^2\Phi_I}{\partial\theta^2}=\frac{B^2\partial^2\Phi_I}{\partial x^2}. \quad . \quad . \quad . \quad . \quad (6)$$

This equation has the operational form

$$\frac{\partial^2\Phi_I}{\partial r^2}+\frac{1}{r}\frac{\partial\Phi_I}{\partial r}+\frac{1}{r^2}\frac{\partial^2\Phi_I}{\partial\theta^2}=B^2p^2\Phi_I. \quad . \quad . \quad . \quad (7)$$

It is known that a solution of (7) is

$$\Phi_I=A_0K_0(Bpr)+\sum_{n=1}^{\infty}A_nK_n(Bpr)\cos n\theta. \quad . \quad . \quad . \quad (8)$$

As the interference potential is symmetric about $\theta=\frac{1}{2}\pi$, only the terms for which n is even need be retained in (8). In equation (8) the A's must be chosen so that

$$A_0K_0'(BpR)+\sum_{n=1}^{\infty}A_{2n}K_{2n}'(BpR)\cos 2n\theta=-\frac{1}{B}H(p)\sin\theta\,e^{-BpR\sin\theta}. \quad (9)$$

$H(p)$ is the operational representation of $h(x)$. From (9),

$$\left.\begin{aligned} A_0&=\frac{-H(p)}{B\pi K_0'(BpR)}\int_0^{\pi}\sin\theta\,e^{-BpR\sin\theta}d\theta \\ \text{and}\quad A_{2n}&=\frac{-2H(p)}{B\pi K_{2n}'(BpR)}\int_0^{\pi}\sin\theta\cos 2n\theta\,e^{-BpR\sin\theta}d\theta \end{aligned}\right\} \quad . \quad . \quad (10)$$

BpR is small and, since $K_{2n}(x)$ is $O(x^{-2n})$ as $x\longrightarrow 0$, it follows from (10) that A_{2n} is $O(R^{2n+1}h)$ for all n.

Because all the K_{2n}'s have the same order of magnitude and the A_{2n}'s are of decreasing order of magnitude at large distances, the most significant term in the expansion must be the first; thus

$$\Phi_I=\frac{2R(x)}{\pi}h'(x)K_0(Bpr)+O(R^2h\log R). \quad . \quad . \quad . \quad (11)$$

When interpreted, the expression for Φ_I becomes

$$\Phi_I(x,r)=\frac{4}{2\pi}\int_0^{x-Br}\frac{R(t)h'(t)}{\sqrt{[(x-t)^2-B^2r^2]}}dt. \quad . \quad . \quad . \quad (12)$$

This interference potential is similar to the perturbation potential for a body of revolution.

In combining the results which have been obtained, the axis of symmetry of the body of revolution is taken to be the x-axis, the y-axis to lie in the plane of the wing perpendicular to the x-axis, and the z-axis to be perpendicular to the x- and y-axes. The origin O of this system of axes is to be the intersection of the leading edge of the wing with the axis of symmetry of the body of revolution. O is a distance d behind the nose of the axi-symmetric body. The body of revolution has radius $R(x)$, where $R(-d)=0$; the area distribution of this body of revolution is $S(x)=\pi R^2(x)$.

Then the potential field of the wing-body combination is given by

$$\phi(x,y,z)=-\frac{1}{2\pi}\int_{-d}^{x-Br}\frac{S'(t)}{\sqrt{[(x-t)^2-B^2r^2]}}\,dt-\frac{1}{\pi}\int\int\frac{Z_x(x',y')\,dx'dy'}{\sqrt{[(x-x')^2-B^2(y-y')^2-B^2z^2]}}+$$

$$+\frac{1}{4\pi}\int\int\frac{z(x-x')}{[(y-y')^2+z^2]}\,\frac{1}{\sqrt{[(x-x')^2-B^2(y-y')^2-B^2z^2]}}\,\frac{\Delta p(x',y')}{\frac{1}{2}\rho_\infty U_\infty^2}\,dx'dy'+$$

$$+\frac{4}{2\pi}\int_{0}^{x-Br}\frac{R(t)\,h'(t)}{\sqrt{[(x-t)^2-B^2r^2]}}\,dt. \qquad . \quad . \quad (13)$$

In equation (12), if $-4R(t)\,h'(t)$ is replaced by $S_1'(t)$, $S_1(t)$ represents the area distribution of a body of revolution which, at large distances, has a potential field equivalent to the potential field of the interference effects.

3. Correction of the Linear Theory

3.1. Body of Revolution

For a body of revolution which has an area distribution $S(x)$, linear theory predicts

$$u=\frac{\partial\phi}{\partial x}=-\frac{1}{2\pi}\int_{0}^{x-Br}\frac{S''(t)}{\sqrt{[(x-t)^2-B^2r^2]}}\,dt. \qquad . \quad . \quad . \quad (14)$$

Here $U_\infty u$ is the perturbation to the main stream in the direction of the main stream, r is the distance from the axis of symmetry and x is the distance along the axis of symmetry. In this case the origin of the system of axes is the nose of the body of revolution.

The detailed correction of the linear theory is contained in Whitham's paper[2]. However, the main points required in treating the flow far from a general wing-body combination are repeated here.

Correction of the linear theory requires that, in equation (14), $x-Br$ be replaced by $\tau(x, r)$, where $\tau=$constant is a more accurate representation of the characteristic curves, which in linear theory are the straight lines $x-Br=$constant. The new characteristics are curves because non-linear theory takes account of the effect of local fluid velocity and changes in pressure upon the speed with which disturbances propagate. In linear theory these effects are neglected and the speed with which disturbances are propagated is assumed to be constant.

If now the result of replacing $x-Br$ by τ in (14) is approximated for r large compared with τ, we get

$$u=-\frac{F(\tau)}{\sqrt{(2Br)}}, \qquad (15)$$

where $$F(\tau)=\frac{1}{2\pi}\int_0^{\tau}\frac{S''(t)}{\sqrt{(\tau-t)}}\,dt.$$

Further, because $(p-p_\infty)/p_\infty=-\gamma M_\infty^2 u$, we get

$$\frac{p-p_\infty}{p_\infty}=\frac{\gamma M_\infty^2 F(\tau)}{\sqrt{(2Br)}} \qquad (16)$$

Now along $\tau(x, r)=$constant, $dx/dr=\cot(\mu+\varepsilon)$ where $\mu=\sin^{-1}(1/M)$ is the local Mach angle and ε is the local direction of flow. But

$$\cot(\mu+\varepsilon)=B+\frac{\gamma+1}{2B}M_\infty^4 u-M_\infty^2(v+Bu)+O(u^2+v^2),$$

where $v=\partial\phi/\partial r$; hence when $dx/dr=\cot(\mu+\varepsilon)$ is integrated, and the arbitrary constant chosen so that for small distances the corrected characteristic becomes the linear characteristic $x-Br=$constant, τ is given by

$$\tau=x-Br+\frac{(\gamma+1)M_\infty^4 F(\tau)\,r^{1/2}}{2^{1/2}B^{3/2}}. \qquad (17)$$

3.2. Symmetrical Wing at Zero Incidence

The problem of a thick symmetric wing has been considered by Whitham[2]. At large distances we expect a solution of the form

$$\phi=-\frac{f(\tau,\theta)}{\sqrt{(2Br)}}.$$

$f(\tau, \theta)$ will depend upon the shape and thickness of the wing in a way which is made apparent by a study of the full linear theory.

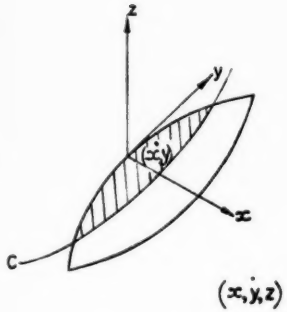

FIGURE 1.

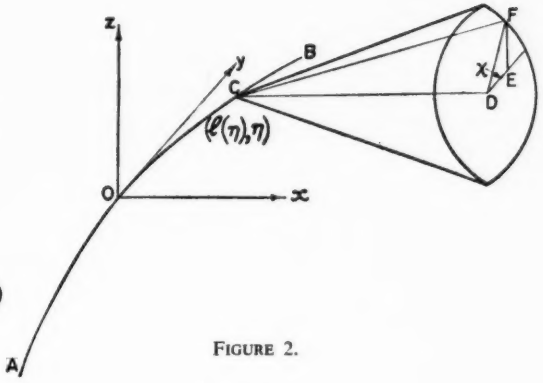

FIGURE 2.

In linear theory the perturbation potential for a symmetric wing which has a thickness distribution $Z=Z(x, y)$ is given by

$$\phi(x, y, z) = -\frac{1}{\pi}\int\int \frac{Z_{x'}(x', y')\,dx'dy'}{\sqrt{[(x-x')^2 - B^2(y-y')^2 - B^2z^2]}}. \qquad (18)$$

The integration is over that part of the wing plan form in the region $(x-x')^2 \geqslant B^2(y-y')^2 + B^2z^2$.

The shaded portion of Fig. 1 is the range of integration of the double integral in equation (18). The curve C is part of the curve of intersection of the forward Mach cone from (x, y, z) with the plane $z=0$.

The parametric equations for the supersonic leading edge of the wing are $x=l(\eta)$, $y=\eta$. A point lies on the supersonic part of the wing leading edge if the tangent to the leading edge, at that point, lies outside the Mach cone from the point.

In Fig. 2, *AOCB* is the leading edge of the wing, *D* and *E* lie in the *xy*-plane, *i.e.* the plane through *A*, *O*, *C* and *B*. *CD* lies in the main stream direction; *CF* is the intersection of the Mach cone through *C* and the wave front which is the envelope of all the Mach cones from points on that part of the wing leading edge which is supersonic. s measures the distance from the wing in the plane *CFD*, which is normal to the wave front and passes through the point $(l(\eta), \eta)$. This plane makes an angle $\chi=\cos^{-1}\{l'(\eta)/B\}$ with the *xy*-plane.

Whitham[2] replaced $x-l(\eta)-Bs$ by τ and the Cartesian co-ordinates y and z by $\eta+s\cos\chi$ and $s\sin\chi$. A set of co-ordinates (x, η, s) can be associated with every field point (x, y, z); η determines a point $(l(\eta), \eta)$ on that part of the wing plan form which is a supersonic leading edge.

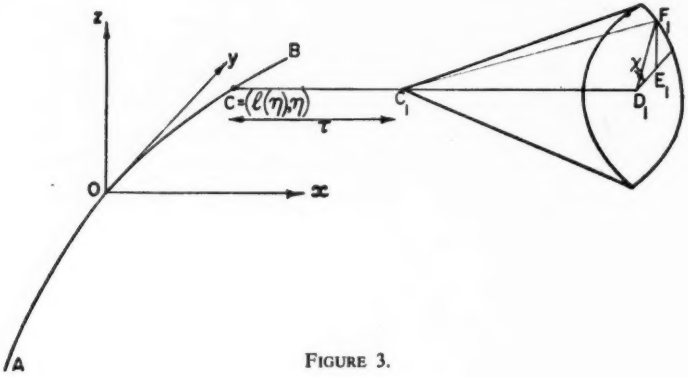

FIGURE 3.

If the origin of co-ordinates is moved to the point $(l(\eta), \eta)$, and the substitutions indicated are made, relation (18) becomes

$$\phi(\tau, s, \chi) = -\frac{1}{\pi}\int\int \frac{Z_\alpha \, d\alpha \, d\beta}{\sqrt{[(Bs+\tau-\alpha)^2 - B^2(s\cos\chi-\beta)^2 - B^2 s^2 \sin^2\chi]}}, \qquad (19)$$

where $\alpha = x' - l(\eta)$ and $\beta = y' - \eta$.

If (19) is approximated for τ/s small, it becomes

$$\phi(\tau, s, \chi) = -\frac{1}{\sqrt{(2Bs)}}\frac{1}{\pi}\int\int \frac{Z_\alpha \, d\alpha \, d\beta}{\sqrt{[\tau-(\alpha-l'\beta)]}}. \qquad (20)$$

In (20) the range of integration is that part of the wing plan form which lies in the region $\alpha - l'\beta \leqslant \tau$; this region is shaded in Fig. 4. As $\tau/s \longrightarrow 0$, $\alpha - l'\beta = \tau$ is the limiting shape of the curve of intersection of the forward Mach cone from (x, y, z) and the plane $z = 0$.

For a wing with a subsonic leading edge the wave front is a Mach cone. The planes which are normal to the wave front all pass through the axis of this cone and the point $(l(\eta), \eta)$ is the vertex of this cone for all values of χ, which, in this case, is equal to θ.

Now (20) can be written

$$\phi = -\frac{f(\tau, \chi)}{\sqrt{(2Bs)}}.$$

Here $$f(\tau, \chi) = \frac{1}{2\pi}\int_0^\tau \frac{S_2'(t)}{\sqrt{(\tau - t)}}\, dt,$$

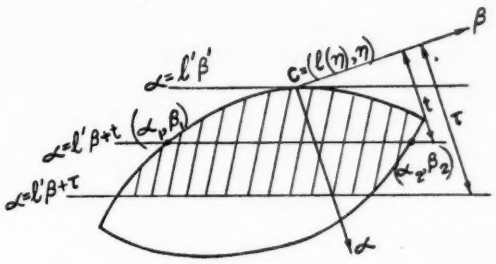

FIGURE 4.

where the dash denotes differentiation with respect to t and

$$S_2'(t) = 2\int_{\beta_1}^{\beta_2} Z_\alpha \, d\beta. \qquad (21)$$

This integral is taken along the line $\alpha - l'\beta = t$; β_1 and β_2 are the ordinates of the points of intersection of the line $\alpha - l'\beta = t$ and the boundary of the wing plan form.

It follows that $$u = \frac{\partial \phi}{\partial x} = -\frac{f'(\tau, \chi)}{\sqrt{(2Bs)}},$$

where a dash denotes differentiation with respect to τ. The expression for u can be written

$$u = -\frac{F(\tau, \chi)}{\sqrt{(2Bs)}}, \qquad (22)$$

where $$F(\tau, \chi) = \frac{1}{2\pi}\int_0^{\tau} \frac{S_2''(t)}{\sqrt{(\tau - t)}}\, dt$$

and the dashes denote differentiation with respect to t.

Hence $$\frac{p - p_\infty}{p_\infty} = \frac{\gamma M_\infty^2 F(\tau, \chi)}{\sqrt{(2Bs)}} \qquad (23)$$

and τ, the corrected expression for the characteristics, is given by

$$\tau = x - l(\eta) - Bs + \frac{(\gamma + 1) M_\infty^4}{2^{1/2} B^{3/2}} F(\tau, \chi)\, s^{1/2}. \qquad (24)$$

From equations (23) and (24) and the form of the function $F(\tau, \chi)$ it is plain that it is possible to find a body of revolution which at large distances produces the same disturbance as the wing. This equivalent body of revolution is centred on a line which passes through the point $(l(\eta), \eta)$ and is parallel to the x-axis; it has an area distribution

$$S_2(t) = 2\int_{\beta_1}^{\beta_2} Z(\alpha, \beta)\, d\beta.$$

The integral is that of (21) with $Z(\alpha, \beta)$ as integrand instead of $\partial Z(\alpha, \beta)/\partial\alpha$.

For very large r. $\chi \longrightarrow \theta$ and $s \longrightarrow r$. Hence ϕ becomes

$$\phi = -\frac{f(\tau, \theta)}{\sqrt{(2Br)}}.$$

The expressions (22), (23) and (24) become

$$\left.\begin{aligned} u &= \frac{\partial\phi}{\partial x} = -\frac{F(\tau, \theta)}{\sqrt{(2Br)}}, \\ \frac{p - p_\infty}{p_\infty} &= \gamma M_\infty{}^2 \frac{F(\tau, \theta)}{\sqrt{(2Br)}} \\ \text{and} \qquad \tau &= x - l(\eta) - Br + \frac{(\gamma+1) M_\infty{}^4}{2^{1/2} B^{3/2}} F(\tau, \theta)\, r^{1/2} \end{aligned}\right\} \quad . \quad . \quad . \quad (25)$$

Here η is chosen so that $l'(\eta) = B\cos\theta$, and the equivalent body of revolution is assumed to be centred on the x-axis.

The shock wave cuts off the characteristics before they intersect. If the shock wave is given by $\tau = T(r, \theta)$, the slope of the shock wave is given by

$$\frac{dx}{dr} = B - \frac{(\gamma+1) M_\infty{}^4}{2^{3/2} B^{3/2}} \frac{F(T, \theta)}{r^{1/2}} + \frac{dT}{dr}\left(1 - \frac{(\gamma+1) M_\infty{}^4}{2^{1/2} B^{3/2}} F'(T, \theta)\, r^{1/2}\right),$$

where the dash denotes differentiation with respect to T.

By introducing a further condition, namely that to the first order in the shock strength the shock wave bisects two intersecting characteristics, it can be shown that

$$\frac{dx}{dr} = B - \frac{(\gamma+1) M_\infty{}^4}{2^{5/2} B^{3/2}} \frac{F(T, \theta)}{r^{1/2}}.$$

Hence $$\frac{dT}{dr} = \frac{(\gamma+1)M_\infty^4}{2^{1/2}B^{3/2}} F'(T,\theta)\, r^{1/2} \frac{dT}{dr} + \frac{(\gamma+1)M_\infty^4}{2^{5/2}B^{3/2}} \frac{F(T,\theta)}{r^{1/2}}.$$

Multiplying both sides of this equation by $2F(T)$ and integrating yields

$$r^{1/2} = \frac{(2B)^{3/2}}{(\gamma+1)M_\infty^4} \frac{\int_0^T F(\tau,\theta)\, d\tau}{F^2(T,\theta)}. \quad . \quad . \quad . \quad (26)$$

Since $F(T,\theta)$ is known from the shape of the wing, (26) and the last two expressions of (25) give the strength and position of the shock for large values of r.

It is seen from (26) that, for very large r, T is near T_0, where $F(T_0,\theta)=0$. It follows that $F(T,\theta)$ will be given approximately by

$$F^2(T,\theta) = \frac{(2B)^{3/2}}{M_\infty^4(\gamma+1)r^{1/2}} \int_0^{T_0} F(\tau,\theta)\, d\tau. \quad . \quad . \quad . \quad (27)$$

Thus, for large r, an asymptotic value of the shock strength is

$$\frac{p-p_\infty}{p_\infty} = \gamma M_\infty^2 \left\{ \frac{(2B)^{1/2}}{(\gamma+1)M_\infty^4} \int_0^{T_0} F(\tau,\theta)\, d\tau \right\}^{1/2} \frac{1}{r^{3/4}}. \quad . \quad . \quad . \quad (28)$$

For distances of this order of magnitude the position of the shock relative to the linear characteristic $x-l(\eta)-Br=T_0$ is given by

$$T_0 = x - l(\eta) - Br + \frac{(\gamma+1)M_\infty^4}{2^{1/2}B^{3/2}} \left\{ \frac{(2B)^{3/2}\int_0^{T_0} F(\tau,\theta)\, d\tau}{(\gamma+1)M_\infty^4} \right\}^{1/2} r^{1/4} \quad . \quad (29)$$

Whenever the part of the boundary of the wing plan form which is a supersonic leading edge contains a straight section within its length, the large-distance approximation (which involves approximating to a straight line the curve of intersection of the forward Mach cone from the field point and the wing plan form) does not yield an estimate of $F(\tau,\theta)$ for small τ. However, the range of τ over which it is impossible to find $F(\tau,\theta)$ in a simple way can be made arbitrarily small by confining the investigation to regions sufficiently far from the wing. In these regions τ must be near T_0, the first zero of $F(\tau,\theta)$. Hence, for large distances, the values for the shock strength and its position which are obtained by applying the theory in the ordinary way will be all right provided that the straight section is not too long.

To find $F(\tau, \theta)$ when θ is given by $l'(\eta) = B\cos\theta = m$, where m is constant, we integrate $Z_n = \partial Z(\alpha, \beta)/\partial\alpha$ along lines which are parallel to the straight edge. This gives

$$S_2'(t) \quad \text{and} \quad F(\tau, \theta) = \frac{1}{2\pi}\int_0^{\tau} \frac{S_2''(t)}{\sqrt{(\tau - t)}}\, dt.$$

3.3. Wing Without Thickness at Incidence

A flat plate of the same shape and size as the wing plan form is inclined at a small angle to the main stream. At large distances from the wing the solution will take the form

$$\phi = -\frac{f(\tau, \theta)}{\sqrt{(2Br)}}.$$

In this case $f(\tau, \theta)$ depends upon the distribution of lift over the wing plan form. The connection between $f(\tau, \theta)$ and the lift distribution is made apparent by a study of the detailed linear theory.

For a flat plate at incidence, linear theory gives

$$\phi(x, y, z) = \frac{1}{4\pi}\int\int \frac{z(x - x')}{(y - y')^2 + z^2} \frac{1}{\sqrt{[(x - x')^2 - B^2(y - y')^2 - B^2z^2]}} \frac{\Delta p}{\tfrac{1}{2}\rho_\infty{}^2 U_\infty{}^2}\, dx'dy'. \quad (30)$$

If the Cartesian co-ordinates are changed, as they were for the problem of the thick wing at zero incidence [$(x = \tau + l(\eta) + Bs$, $y = \eta + s\cos\chi$, $z = s\sin\chi$, where $B\cos\chi = l'(\eta)$] relation (30) becomes

$$\phi = \frac{1}{4\pi}\int\int \frac{s\sin\chi\,(\tau + Bs - \alpha)}{(\cos\chi - \beta)^2 + s^2\sin^2\chi} \frac{1}{\sqrt{[(Bs + \tau - \alpha)^2 - B^2(s\cos\chi - \beta)^2 - B^2s^2\sin^2\chi]}} \times \frac{\Delta p(\alpha, \beta)}{\tfrac{1}{2}\rho_\infty{}^2 U_\infty{}^2}\, d\alpha d\beta. \quad (31)$$

Again $\alpha = x' - l(\eta)$, $\beta = y' - \eta$, and s and χ have the same meaning as before.

If s is large compared with τ, (31) becomes

$$\phi = \frac{B\sin\chi}{4\pi\sqrt{(2Bs)}}\int\int \frac{\Delta p(\alpha, \beta)}{\tfrac{1}{2}\rho_\infty U_\infty{}^2} \frac{1}{\sqrt{[\tau - (\alpha - l'\beta)]}}\, d\alpha d\beta. \quad (32)$$

The double integration is over the part of the wing plan form which lies within the region $\alpha - l'\beta \leqslant \tau$.

Equation (32) can be written in the form

$$\phi = -\frac{f(\tau, \chi)}{\sqrt{(2Bs)}}$$

Here $$f(\tau, \chi) = \left[\frac{1}{2\pi}\int_0^{\tau} \frac{S_3'(t)}{\sqrt{(\tau - t)}}\, dt\right]\left[-\frac{B \sin \chi}{2}\right], \quad . \quad . \quad (33)$$

where $$S_3'(t) = \int_{\beta_1}^{\beta_2} \frac{\Delta p(\alpha, \beta)}{\frac{1}{2}\rho_\infty U_\infty^2}\, d\beta. \quad . \quad . \quad . \quad . \quad . \quad . \quad (34)$$

The integral for $S_3'(t)$ is taken along the line $x - l'\beta = t$; the ordinates of the intersection of this line and the boundary of the wing plan form are β_1 and β_2.

Because $$\phi = -\frac{f(\tau, \chi)}{\sqrt{(2Bs)}},$$

we can write $$u = \frac{\partial \phi}{\partial x} = -\frac{F(\tau, \chi)}{\sqrt{(2Bs)}}, \quad . \quad . \quad . \quad . \quad (35)$$

where $$F(\tau, \chi) = \frac{\partial f(\tau, \chi)}{\partial \tau}.$$

Further, $$\frac{p - p_\infty}{p_\infty} = \frac{\gamma M_\infty^2 F(\tau, \chi)}{\sqrt{(2Bs)}}, \quad . \quad . \quad . \quad . \quad . \quad (36)$$

where $$F(\tau, \chi) = -G(\tau, \chi)\left[\frac{B \sin \chi}{2}\right] \quad . \quad . \quad . \quad . \quad (37)$$

and $$G(\tau, \chi) = \frac{1}{2\pi}\int_0^{\tau} \frac{S_3''(t)}{\sqrt{(\tau - t)}}\, dt. \quad . \quad . \quad . \quad . \quad (38)$$

As for the thickness problem, the improved equation for the characteristics is

$$\tau = x - l(\eta) - Bs + \frac{(\gamma + 1) M_\infty^4}{2^{1/2} B^{3/2}} F(\tau, \chi)\, s^{1/2}. \quad . \quad . \quad . \quad (39)$$

Because of the form of $G(\tau, \chi)$, it is evident that (36), (37) and (39) bear a close resemblance to similar relations for a certain body of revolution. The axis of this body of revolution is parallel to the x-axis, and it passes through the point $(l(\eta), \eta)$ where $l'(\eta) = B \cos \chi$. This means that for a flat plate at incidence the perturbation potential at large distances is equivalent to the perturbation potential at large distances from a certain body of revolution. However, it should be noted that the

equivalent body depends upon direction; there is a different equivalent body for each direction. The area distribution of the equivalent body is $S_4(x)$ where

$$S_4(x) = S_3(x)\left|\frac{B\sin\chi}{2}\right|;$$

$S_3(x)$ is given by (34).

For $0 < \chi < \pi$, the perturbation potential of the inclined flat plate is minus one times that for the equivalent body. For $-\pi < \chi < 0$ the perturbation potential of the plate is equal to that for the equivalent body.

Now, again as for the thickness problem, if the shock wave is given by $\tau = T(s, \chi)$, then at large distances from the wing the relation between T and s for any particular value of χ is given by

$$s^{1/2} = \frac{(2B)^{3/2}}{(\gamma+1)M_\infty{}^4}\frac{\int_0^T F(\tau,\chi)\,d\tau}{F^2(T,\chi)} \quad . \quad . \quad . \quad . \quad . \quad (40)$$

For very large s, $\chi \longrightarrow \theta$ and $s \longrightarrow r$ and (36), (39) and (40) become

$$\frac{p-p_\infty}{p_\infty} = \gamma M_\infty{}^2 \frac{F(\tau,\theta)}{\sqrt{(2Br)}} \quad . \quad . \quad . \quad . \quad . \quad . \quad . \quad . \quad (41)$$

$$\tau = x - l(\eta) - Br + \frac{(\gamma+1)M_\infty{}^4}{2^{1/2}B^{3/2}} F(\tau,\theta)\, r^{1/2} \quad . \quad . \quad . \quad (42)$$

and

$$r^{1/2} = \frac{(2B)^{3/2}}{(\gamma+1)M_\infty{}^4}\frac{\int_0^T F(\tau,\theta)\,d\tau}{F^2(T,\theta)} \quad . \quad . \quad . \quad . \quad . \quad . \quad (43)$$

$F(\tau,\theta)$ is known from the lift distribution, so (41), (42) and (43) give the strength and position of the shock for large values of r.

It is seen from (43) that, for very large values of r, T must be near T_0, where $F(T_0,\theta)$ is zero. From (43) it follows that $F(T,\theta)$ will be given approximately by

$$F^2(T,\theta) = \frac{(2B)^{3/2}}{M_\infty{}^4(\gamma+1)r^{1/2}}\int_0^{T_0} F(\tau,\theta)\,d\tau. \quad . \quad . \quad . \quad . \quad (44)$$

Thus for large r an asymptotic value for the shock strength is

$$\frac{p-p_\infty}{p_\infty} = \gamma M_\infty{}^2 \left\{\frac{(2B)^{1/2}}{(\gamma+1)M_\infty{}^4}\int_0^{T_0} F(\tau,\theta)\,d\tau\right\}^{1/2}\frac{1}{r^{3/4}}. \quad . \quad . \quad (45)$$

The position of the shock relative to the linear characteristic $x-l(\eta)-Br=T_0$ is given by

$$T_0=x-l(\eta)-Br+\frac{(\gamma+1)M_\infty{}^4}{2^{1/2}B^{3/2}}\left\{\frac{(2B)^{3/2}\int_0^{T_0}F(\tau,\theta)\,d\tau}{(\gamma+1)M_\infty{}^4}\right\}^{1/2}r^{1/4}. \quad . \quad (46)$$

In (45) and (46),

$$F(\tau,\theta)=-G(\tau,\theta)[\tfrac{1}{2}B\sin\theta], \quad . \quad . \quad . \quad . \quad (47)$$

$$\text{where} \quad G(\tau,\theta)=\frac{1}{2\pi}\int_0^\tau\frac{S_3''(t)}{\sqrt{(\tau-t)}}. \quad . \quad . \quad . \quad . \quad (48)$$

Now η is determined from $l'(\eta)=B\cos\theta$ and the equivalent bodies are assumed to be centred upon the x-axis.

For $-\pi<\theta<0$, substituting (47) and (48) in (45) and (46) gives

$$\frac{p-p_\infty}{p_\infty}=\left\{\frac{\gamma^2B^{3/2}}{2^{1/2}(\gamma+1)}\int_0^{T_0}G(\tau,\theta)\,d\tau\right\}^{1/2}\frac{|\sin\theta|^{1/2}}{r^{3/4}}$$

$$\text{and} \quad T_0=x-l(\eta)-Br+\left\{\frac{(\gamma+1)M_\infty{}^4\int_0^{T_0}G(\tau,\theta)\,d\tau}{B^{1/2}}\right\}^{1/2}|\sin\theta|^{1/2}r^{1/4}. \quad . \quad . \quad . \quad (49)$$

When the supersonic leading edge has a straight section within its length, for which $l'(\eta)=m=B\cos\theta$, then $F(\tau,\theta)$ cannot be found for small τ. However, as for the thick wing at zero incidence, at very large distances from the wing the range of τ over which $F(\tau,\theta)$ cannot be found is small. Over this range $F(\tau,\theta)$ is taken to be the value obtained by applying the theory as if the edge were not straight; the error in doing this will be small if the distances involved are large enough.

To find $F(\tau,\theta)$ when $B\cos\theta=m$, we integrate $\Delta p/(\frac{1}{2}\rho U_\infty{}^2)$ along lines parallel to the straight edge; this gives $S_3'(t)$ and

$$F(\tau,\theta)=-\left[\frac{1}{2\pi}\int_0^\tau\frac{S_3''(t)}{\sqrt{(\tau-t)}}\,dt\right]\left[\frac{B\sin\theta}{2}\right].$$

3.4. Wing-Body Combination

In linearised theory the expression for the perturbation potential of a winged body is given by equation (13) in Section 2. When this expression is corrected and

the large-distance approximation is made, it is found that

$$\frac{p-p_\infty}{p_\infty}=\gamma M_\infty{}^2\frac{F(\tau,\theta)}{\sqrt{(2Br)}}, \qquad (50)$$

where $$F(\tau,\theta)=\frac{H_1(\tau+d)}{2\pi}\int_{-d}^{\tau}\frac{S''(t)}{\sqrt{(\tau-t)}}\,dt-\frac{H_1(\tau)}{2\pi}\int_{0}^{\tau}\frac{S_1''(t)}{\sqrt{(\tau-t)}}\,dt+$$

$$+H_1(\tau-l(\eta))\left\{\frac{1}{2\pi}\int_{l(\eta)}^{\tau}\frac{S_2''(t)}{\sqrt{(\tau-t)}}\,dt-\frac{B\sin\theta}{2}\,\frac{1}{2\pi}\int_{l(\eta)}^{\tau}\frac{S_3''(t)}{\sqrt{(\tau-t)}}\,dt\right\} \qquad (51)$$

$H_1(t)$ is the Heaviside unit function and $l'(\eta)=B\cos\theta$.

At large distances, if the shock is $\tau=T(r,\theta)$,

$$\left.\begin{aligned}&\frac{p-p_\infty}{p_\infty}=\gamma M_\infty{}^2\frac{F(\tau,\theta)}{\sqrt{(2Br)}},\\&r^{1/2}=\frac{(2B)^{3/2}}{(\gamma+1)M_\infty{}^4}\,\frac{\int_0^T F(\tau,\theta)\,d\tau}{F^2(T,\theta)}\\&\text{and}\qquad \tau=x-l(\eta)-Br+(\gamma+1)M_\infty{}^4F(\tau,\theta)\,r^{1/2}/(2^{1/2}B^{3/2})\end{aligned}\right\}. \qquad (52)$$

The relations numbered (52) locate the shock and give its strength. From the form of $F(\tau,\theta)$ and these relations it is evident that in every direction the wing-body combination can be associated with some body of revolution. Further, the flow at large distances from this body of revolution will be the same as the flow at large distances from the wing-body combination. Because of its complex shape it is impossible to say very much about what happens near to a general wing-body combination. However, it is not necessary to use this theory up to the body for, in the regions close to the body, linear theory does not require correction.

As $r\longrightarrow\infty$, it follows from (52) that asymptotic values for the shock strength and its position are given by

$$\left.\begin{aligned}&\frac{p-p_\infty}{p_\infty}=\frac{\gamma M_\infty{}^2}{r^{3/4}}\left\{\frac{(2B)^{3/2}\int_0^{T_0}F(\tau,\theta)\,d\tau}{2B(\gamma+1)M_\infty{}^4}\right\}^{1/2}\\&\text{and}\qquad x-l(\eta)-Br=T_0-\frac{(\gamma+1)M_\infty{}^4}{2^{1/2}B^{3/2}}\left\{\frac{(2B)^{3/2}\int_0^{T_0}F(\tau,\theta)\,d\tau}{(\gamma+1)M_\infty{}^4}\right\}^{1/2}r^{1/4}\end{aligned}\right\}. \qquad (53)$$

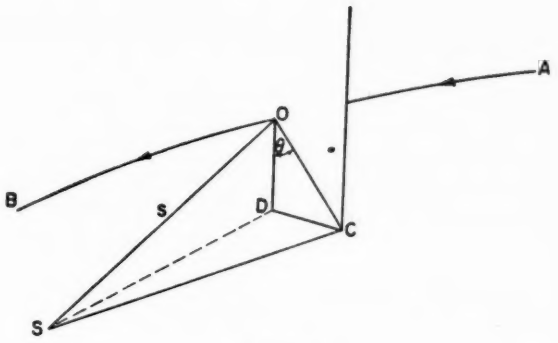

FIGURE 5.

4. Non-Uniform Motion

When an asymmetric body accelerates along a curved path, further directional effects must be included. These directional effects are due to non-uniform motion, which alters the way in which the disturbance decays as it propagates outwards from the body. If the body is axi-symmetric, there are no initial directional effects; all the asymmetry is a result of the non-uniform motion. In this case Rao[3] found the excess pressure ratio to be

$$\frac{p-p_\infty}{p_\infty} = \frac{\gamma M^{5/2} F(\tau)}{\{2(M^2-1)\}^{1/2} s^{1/2}(1-s/\lambda)^{1/2}}, \quad . \quad . \quad . \quad . \quad . \quad (54)$$

where
$$\lambda = \frac{a_\infty{}^2(M^2-1)}{a_\infty{}^2(M^2-1)^{1/2} M\kappa\cos\theta + (a_\infty/M)(dM/dt)_{t=t_0}} \quad . \quad . \quad (55)$$

In regions of compression, where $F(\tau) > 0$, shock waves are formed; using body surface and are the orthogonal trajectories of the wave front. As for geometrical acoustics, the disturbance propagates along these rays. κ is the curvature of the flight path. θ is the polar angle in a plane perpendicular to the flight path, and $a_0 dM/dt$ is the acceleration along the flight path. $Ma_\infty{}^2\kappa$ is the component of acceleration perpendicular to the flight path. $s(1-s/\lambda)$ is proportional to the cross-sectional area of a bundle of neighbouring rays. t_0 is the time at which the ray set out from the body.

Figure 5 illustrates the co-ordinate system used in this section. AB is the flight path, COD is a plane perpendicular to the flight path, where O is the position of the body at time $t=t_0$. SCO is a plane inclined at an angle θ to the instantaneous plane of motion of the body at the time $t=t_0$. s is measured along OS, which is a ray. OS is inclined at an angle $\frac{1}{2}\pi-\mu_0$ to OB, where $\mu_0=\sin^{-1}\{1/M(t_0)\}$ and $M(t)$ is the flight Mach number of the body.

$F(\tau)$ gives the initial "wave" profile of the disturbance. Rao verified that, for an axi-symmetric body, the function $F(\tau)$ in non-uniform motion is exactly that used to describe the flow pattern for the same body moving uniformly.

If a is the local sound speed and u the local fluid velocity along a ray, the correct speed of propagation of disturbance is

$$\left(\frac{ds}{dt}\right)_{\tau=\text{constant}} = a+u.$$

In view of expression (54) for the excess pressure, this relation, when integrated, gives

$$\tau = U(t_0)(t-t_0-s/a_\infty) + \frac{(\gamma+1)M^{7/2}}{\{8(M^2-1)\}^{1/2}} F(\tau)\, b(s), \quad . \quad . \quad (56)$$

$$\text{where} \qquad b(s) = \int_0^s \frac{ds}{s^{1/2}(1-s/\lambda)^{1/2}}.$$

When this integral is evaluated, we get

$$b(s) = 2\lambda^{1/2} \sin^{-1}(s/\lambda)^{1/2}, \qquad \text{if} \quad \lambda > 0,$$

$$\text{and} \qquad b(s) = 2(-\lambda)^{1/2} \sinh^{-1}\{s/(-\lambda)\}^{1/2}, \quad \text{if} \quad \lambda < 0.$$

In (56), the arbitrary function of τ which occurs in the integration has been chosen so that near the body the improved expression for the characteristics becomes $U(t_0)(t-t_0-s/a_\infty)$.

In regions of compression, where $F(\tau) > 0$, shock waves are formed; using the Rankine-Hugoniot shock conditions, with the further condition that at the shock the disturbance propagates with the speed of the shock, it is found that, if the shock is given by $\tau = T(s)$, the relation between T and s is

$$\frac{(\gamma+1)M^{7/2}}{\{32(M^2-1)\}^{1/2}} b(s) = \frac{\int_0^T F(\tau)\, d\tau}{F^2(T)} \quad . \quad . \quad . \quad . \quad (57)$$

From (57) it follows that, if s is to be large, T must be near to T_0, where $F(T_0)=0$. Then, for large s, (54) and (56) become approximately

$$\left.\begin{aligned} \frac{p-p_\infty}{p_\infty} &= \frac{2^{3/4}M^{3/4}\gamma}{(\gamma+1)^{1/2}(M^2-1)^{1/4}} \left\{ \frac{\int_0^{T_0} F(\tau)\, d\tau}{b(s)\, s\,(1-s/\lambda)} \right\}^{1/2} \\ \text{and} \qquad T_0 &= U(t_0)(t-t_0-s/a_\infty) + \frac{2(\gamma+1)^{1/2}M^{7/4}}{(M^2-1)^{1/4}} \left\{ b(s) \int_0^{T_0} F(\tau)\, d\tau \right\}^{1/2} \end{aligned}\right\} \quad . \quad (58)$$

The second expression of (58) locates the shock relative to the linear characteristic

$$T_0 = U(t_0)(t - t_0 - s/a_\infty).$$

In view of Rao's work, and the form of $F(\tau, \theta)$ for a particular value of θ, it follows that the $F(\tau, \theta)$ used to describe the shock pattern at large distances from the wing-body combination in the steady case can be used to describe the shock pattern in the unsteady case.

Thus the position and strength of the front shock for the wing-body combination moving non-uniformly along a curved path are given by

$$\left.\begin{aligned} \frac{p - p_\infty}{p_\infty} &= \frac{2^{3/4} M^{3/4} \gamma}{(\gamma+1)^{1/2} (M^2-1)^{1/4}} \left\{ \frac{\int_0^{T_0} F(\tau, \theta)\, d\tau}{b(s)\, s\,(1 - s/\lambda)} \right\}^{1/2} \\ \text{and} \quad T_0 &= U(t_0)(t - t_0 - s/a_\infty) + \frac{2(\gamma+1)^{1/2} M^{7/4}}{(M^2-1)^{1/4}} \left\{ b(s) \int_0^{T_0} F(\tau, \theta)\, d\tau \right\}^{1/2} \end{aligned}\right\}. \quad (59)$$

$F(\tau, \theta)$ is given by

$$F(\tau, \theta) = \frac{H_1(\tau + d)}{2\pi} \int_{-d}^{\tau} \frac{S''(t)}{\sqrt{(\tau - t)}}\, dt - \frac{H_1(\tau)}{2\pi} \int_0^{\tau} \frac{S_1''(t)}{\sqrt{(\tau - t)}} + \\ + \frac{H_1(\tau - l(\eta))}{2\pi} \left[\int_{l(\eta)}^{\tau} \frac{S_2''(t)}{\sqrt{(\tau - t)}}\, dt - \frac{B \sin\theta}{2} \int_0^{\tau} \frac{S_3''(t)}{\sqrt{(\tau - t)}}\, dt \right], \quad (60)$$

where $H_1(t)$ is the Heaviside unit function.

In (60), η is chosen so that $l'(\eta) = B \cos\theta$. $(l(\eta), \eta)$ is the parametric representation of the supersonic leading edge of the wing part of the wing-body combination.

5. Examples

5.1. A Symmetrical Wing

In this example we find the variation with direction of the asymptotic value of the shock strength at large distances from a symmetrical wing, which has an elliptic plan form and a thickness distribution given by

$$Z(x, y) = \delta \left(1 - \frac{(x-a)^2}{a^2} - \frac{y^2}{b^2} \right).$$

The thickness is zero on the boundary of the wing plan form.

From the theory, the disturbance at large distances is

$$\frac{p-p_\infty}{p_\infty}=\gamma M_\infty{}^2\frac{F(\tau,\theta)}{\sqrt{(2Br)}}.$$

Here $$F(\tau,\theta)=\frac{1}{2\pi}\int_0^\tau\frac{S''(t)}{\sqrt{(\tau-t)}}$$

and $$S'(t)=2\int_{\beta_1}^{\beta_2}\frac{\partial Z}{\partial\alpha}\,d\beta.$$

In the integral for $S'(t)$, $\alpha=x-l(\eta)$ and $\beta=y-\eta$. The integral is taken along the line $\alpha-l'\beta=t$; β_1 and β_2 are the intersections of this line and the boundary of the wing plan form. θ is given by $l'(\eta)=B\cos\theta$, where, in this example,

$$l(\eta)=a[1-(1-\eta^2/b^2)^{1/2}].$$

We get $$S'(t)=\frac{8\delta(b^2-\eta^2)^2}{a^3b^3}\left\{\frac{ab}{(b^2-\eta^2)^{1/2}}-t\right\}\left\{\frac{2abt}{(b^2-\eta^2)^{1/2}}-t^2\right\}^{1/2}$$

and $$S''(t)=\frac{8\delta(b^2-\eta^2)^2}{a^3b^3t^{1/2}}\left\{\frac{a^2b^2}{(b^2-\eta^2)}-\frac{2abt}{(b^2-\eta^2)^{1/2}}+t^2\right\}\left\{\frac{2ab}{(b^2-\eta^2)^{1/2}}-t\right\}^{-1/2}-$$

$$-\frac{8\delta(b^2-\eta^2)^2}{a^3b^3}t^{1/2}\left\{\frac{2ab}{(b^2-\eta^2)^{1/2}}-t\right\}^{1/2}.$$

Hence $$F(\tau,\theta)=\frac{4\sqrt{2}}{3\pi}\frac{\delta b}{a^{3/2}}\left(1-\frac{\eta^2}{b^2}\right)^{5/4}\left\{[8(b_1/a_1)^2-5]\,\mathrm{K}(b_1/a_1)+\right.$$

$$\left.+[8-16(b_1/a_1)^2\mathrm{E}(b_1/a_1)]\right\}. \qquad (61)$$

$\mathrm{K}(k)$ and $\mathrm{E}(k)$ are the complete elliptic functions of the first and second kinds respectively.

In equation (61), $b_1=\tau^{1/2}$ and $a_1=(2ab)^{1/2}(b^2-\eta^2)^{-1/4}$.

Let $$x=\frac{\left(\frac{\tau}{2a}\right)^{1/2}}{\left(1+\frac{B^2b^2\cos^2\theta}{a^2}\right)^{1/4}},$$

and let $G(x)=(8x^2-5)\,\mathrm{K}(x)+(8-16x^2)\,E(x)$. The first zero of $G(x)$ occurs at $x=0{\cdot}56$.

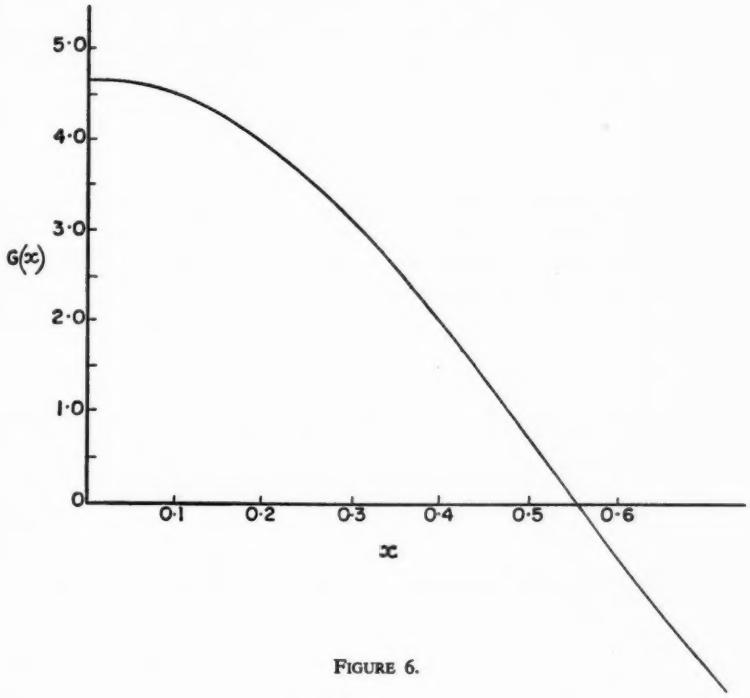

FIGURE 6.

Then $$F(\tau,\theta)=\frac{4\sqrt{2}}{3\pi}\frac{\delta b}{a^{3/2}}\frac{G(x)}{\left(1+\dfrac{B^2b^2\cos^2\theta}{a^2}\right)^{5/4}}. \qquad . \quad . \quad . \quad (62)$$

Figure 6 shows the variation of $G(x)$ with x.

To find the position and strength of the front shock wave, we must evaluate

$$\int_0^{T_0} F(\tau,\theta)\,d\tau,$$

where T_0 is the first zero of $F(\tau,\theta)$. This gives

$$\int_0^{T_0} F(\tau,\theta)\,d\tau=\frac{16\sqrt{2}\,\delta b}{3\pi a^{1/2}}\frac{\displaystyle\int_0^X xG(x)\,dx}{\left(1+\dfrac{B^2b^2\cos^2\theta}{a^2}\right)^{3/4}} \qquad . \quad . \quad . \quad (63)$$

where $X=0{\cdot}56$.

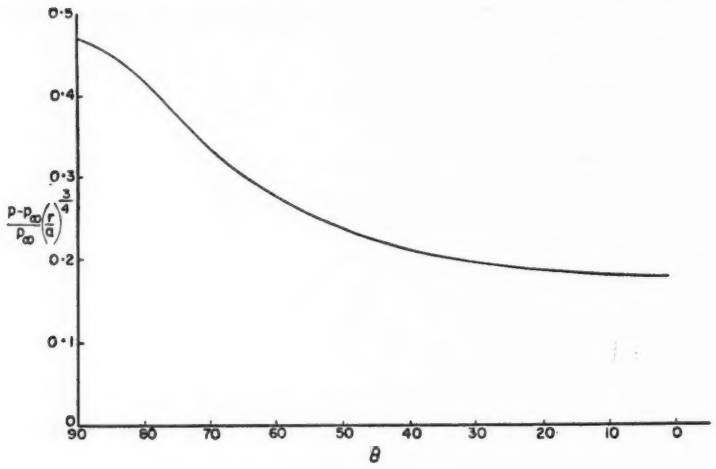

FIGURE 7.

$\int_0^X x\,G(x)$ was evaluated numerically to be 0·34. Hence (63) becomes

$$\int_0^{\tau_0} F(\tau,\theta)\,d\tau = \frac{0{\cdot}815\delta b}{a^{1/2}\left(1+\dfrac{B^2b^2\cos^2\theta}{a^2}\right)^{3/4}}.$$

The asymptotic formula for the strength of the front shock is

$$\frac{p-p_\infty}{p_\infty} = \frac{\gamma M_\infty^{\,2}}{r^{3/4}}\left\{\frac{(2B)^{1/2}}{(\gamma+1)M_\infty^{\,4}}\int_0^{\tau_0} F(\tau,\theta)\,d\tau\right\}^{1/2} \quad . \quad . \quad . \quad (64)$$

In this example

$$\frac{p-p_\infty}{p_\infty} = \frac{0{\cdot}97B^{1/4}\delta^{1/2}b^{1/2}}{a(r/a)^{3/4}\left(1+\dfrac{B^2b^2\cos^2\theta}{a^2}\right)^{3/8}} \quad . \quad . \quad . \quad . \quad (65)$$

In Fig. 7, $[(p-p_\infty)/p_\infty](r/a)^{3/4}$ is plotted against θ for $\delta/a=0{\cdot}087$, $b/a=2$, and $M=2$. From Fig. 7, it is seen that, as $r\longrightarrow\infty$, at $M=2$, the shock strength in the plane of the wing is 0·358 times that in a plane perpendicular to the wing.

In the direction $\theta=\frac{1}{2}\pi$, the value of shock strength predicted by the asymptotic formula for the shock strength is almost exact for $r>12a$.

When $\theta=0$, the ratio $[(p-p_\infty)/p_\infty]'$ to $(p-p_\infty)/p_\infty$ is given for different values of r/a. $(p-p_\infty)/p_\infty$ is the exact shock strength and it is calculated from equations (25) and (26) by evaluating

$$F(T,0) \quad \text{and} \quad \int_0^T F(\tau,0)\,d\tau$$

($F(T,0)$ is given by equation (61)) for a given value of T; r/a is found from (26) and $(p-p_\infty)/p_\infty$ is the corresponding value of the shock strength given by the second equation of (25). $[(p-p_\infty)/p_\infty]'$ represents the asymptotic value of the shock strength at the distance r/a, calculated from (26). $[(p-p_\infty)/p_\infty]'$ is given in equation (65). The resulting values are

r/a	365·3	380·6	1460	9395
$\dfrac{(p-p_\infty)/p_\infty}{[(p-p_\infty)/p_\infty]'}$	0·6298	0·7213	0·8281	0·9000

The position of the shock relative to the linear characteristic $x-l(\eta)-Br=T_0$ is given by

$$x-l(\eta)-Br=T_0-\left\{\frac{(\gamma+1)M_\infty{}^4 2^{1/2}}{B^{3/2}}\int_0^{T_0}F(\tau,\theta)\,d\tau\right\}^{1/2}r^{1/4}.$$

In this example,

$$x-l(\eta)-Br=0{\cdot}627a\left(1+\frac{B^2b^2\cos^2\theta}{a^2}\right)^{1/2}-\frac{2{\cdot}58M_\infty{}^2\delta^{1/2}b^{1/2}(r/a)^{1/4}}{B^{3/4}\left(1+\frac{B^2b^2\cos^2\theta}{a^2}\right)^{3/8}}.$$

5.2. A Wing-Body Combination

Consider the effect of a wing-body combination at large distances from the axis in the directions $\theta=\pm\frac{1}{2}\pi$.

The body of revolution is given by

$$R(x)=\begin{cases}(\delta x/l)(l-x), & \text{for } 0<x<l\\ 0, & \text{for } x<0, x>l.\end{cases}$$

The wing, which has a delta-shaped plan form, is inclined at an angle α to the main stream; it has a thickness distribution which is given by

$$Z=\delta_2(y)\left\{1-\left(\frac{x-\frac{1}{2}(c+my)}{\frac{1}{2}(c-my)}\right)^2\right\}$$

and $\quad \delta_2(y)=\delta_1(1-y^2/a^2)$.

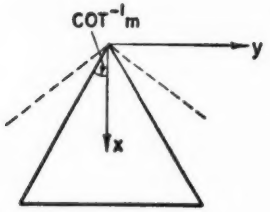

FIGURE 8.

The wing plan form is illustrated in Fig. 8. The thickness of the wing is zero on the boundary of the wing plan form. In this example the vertex of the wing plan form is placed at a distance of one quarter of the body's length from the nose.

The contribution from the body of revolution to $F(\tau, \pm\frac{1}{2}\pi)$ for the combination is

$$2\delta^2 l^{1/2}\{(\tau/l)^{1/2} - 4(\tau/l)^{3/2} + 16/5(\tau/l)^{5/2}\}.$$

For $0 < \tau_1 < 0{\cdot}75$, the contribution to $F(\tau, \pm\frac{1}{2}\pi)$ from the interference potential is

$$+\frac{16\delta\delta_1}{\pi c^{1/2}}\left\{-\frac{12}{5}\left(\frac{\tau_1}{c}\right)^{5/2} + \frac{7}{3}\left(\frac{\tau_1}{c}\right)^{3/2}\right\}.$$

Here, and hereafter, $\tau_1 = \tau - 0{\cdot}25l$ and $c = 0{\cdot}75l$. The contribution from the interference potential is zero for $\tau_1 < 0$.

The contributions to $F(\tau_1 \pm \frac{1}{2}\pi)$ from the thickness of the wing is found by first integrating $\partial Z(x, y)/\partial x$ along lines $x = t$, where t is constant; this integration is between the points of intersection of the line $x = t$ and the leading edges of the wing. Next, we differentiate this integral with respect to t, divide by $\pi\sqrt{(\tau_1 - t)}$ and integrate the result with respect to t for $0 < t < \tau_1$. Thus, for $0 < \tau_1 < c$, the contribution to $F(\tau, \pm\frac{1}{2}\pi)$ from the wing at zero incidence is

$$\frac{16\delta_1}{\pi m c^{1/2}}\left\{\frac{8}{3}(\tau_1/c)^{3/2} - 3(\tau_1/c)^{1/2} + 4\sqrt{(1-\tau_1/c)}\tan^{-1}\left[\frac{(\tau_1/c)^{1/2}}{\sqrt{(1-\tau_1/c)}}\right] + \right.$$

$$\left. + \frac{2(\tau_1/c)}{\sqrt{(1+\tau_1/c)}}\log\left[\frac{\sqrt{(1+\tau_1/c)} - \sqrt{(\tau_1/c)}}{\sqrt{(1+\tau_1/c)} + \sqrt{(\tau_1/c)}}\right]\right\}.$$

The contribution is zero for $\tau_1 < 0$.

To find the contribution from the wing at incidence we replace $\partial Z(x, y)/\partial x$ by $\Delta p/(\frac{1}{2}\rho_\infty U^2)$ and proceed as for the thick wing at zero incidence; this result, multiplied by $\mp B/4$, is the contribution to $F(\tau, \pm\frac{1}{2}\pi)$ for the combination, due to incidence effects of the wing.

For a delta wing swept-back inside the Mach cone, Goldstein and Ward[6] have shown that

$$\frac{\Delta p}{\frac{1}{2}\rho_\infty U^2} = \frac{4\alpha m_1^2}{\mathrm{E}(k)\sqrt{(m_1^2 - y^2/x^2)}}.$$

E is the complete elliptic function of the second kind to modulus $k = \sqrt{(1 - m_1^2 B^2)}$ and $m_1 = 1/m$.

It follows that the conribution to $F(\tau, \pm\frac{1}{2}\pi)$ due to incidence effects is

$$\mp \frac{2\alpha c^{1/2} B}{m^2 \mathrm{E}(k)} \left(\frac{\tau_1}{c}\right)^{1/2}, \qquad 0 < \tau_1 < c.$$

For $\tau_1 < 0$ this contribution is zero. This result is that obtained by Whitham[2]. For $\tau_1 > c$ this contribution to $F(\tau, \pm\frac{1}{2}\pi)$ decays in a way typical of a finite body.

$F(\tau, \pm\frac{1}{2}\pi)$ for the combination is the sum of the contributions from the wing, the body, and the interference effects.

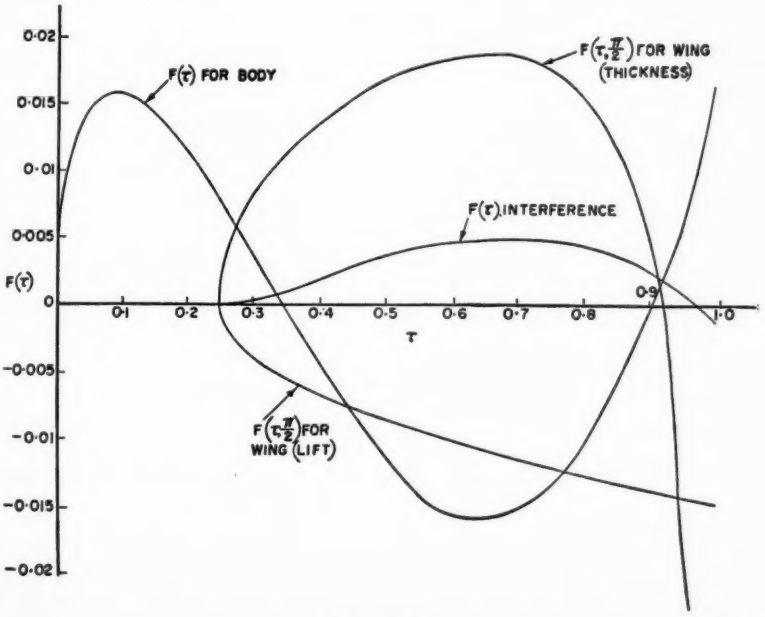

FIGURE 9.

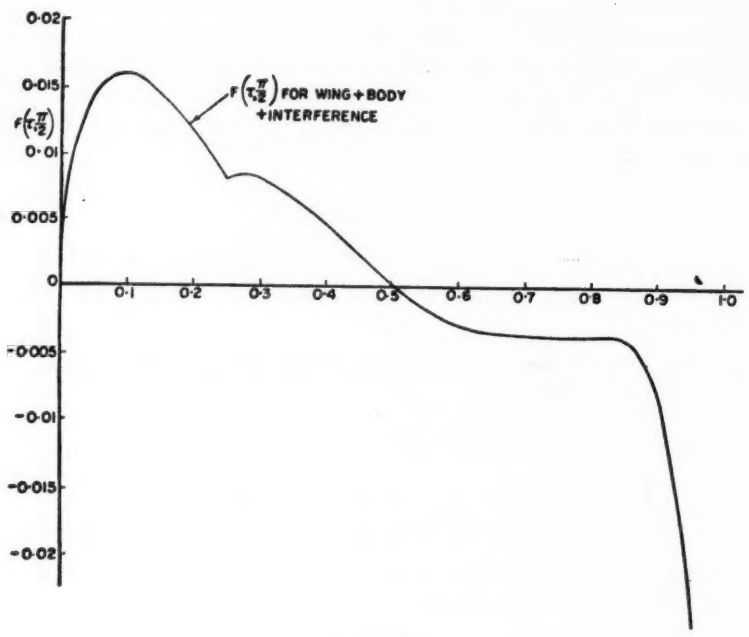

FIGURE 10.

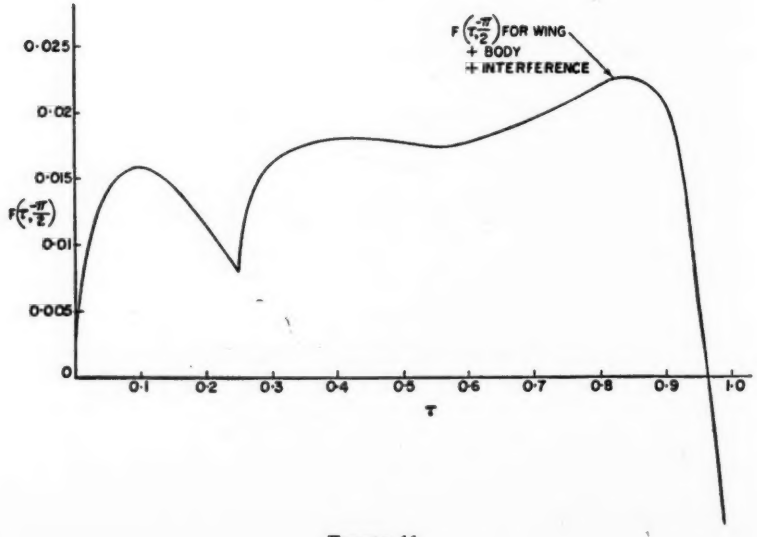

FIGURE 11.

Figures 10 and 11 are of $F(\tau, \frac{1}{2}\pi)$ and $F(\tau, -\frac{1}{2}\pi)$ for the wing-body combination, where the length of the body is $l=1$, $c=0{\cdot}75$, $\delta_1=0{\cdot}01$, $\delta=0{\cdot}2$, $M=2$, $m=\cot 29°$ and $\alpha=1\frac{1}{2}°$. Fig. 9 shows the variation with τ of the individual contributions to $F(\tau, \pm\frac{1}{2}\pi)$. Under these conditions

$$\int_0^{T_0} F(\tau, \tfrac{1}{2}\pi)=0{\cdot}0046,$$

and

$$\int_0^{T_1} F(\tau, -\tfrac{1}{2}\pi)=0{\cdot}0161.$$

These integrals were evaluated numerically.

For a given Mach number the asymptotic value for the shock strength at large distances in the direction $\theta=\frac{1}{2}\pi$ is proportional to

$$\left\{\int_0^{T_0} F(\tau, \tfrac{1}{2}\pi)\, d\tau\right\}^{1/2}.$$

T_0 is the least non-zero value of τ for which $F(\tau, \frac{1}{2}\pi)=0$.

Similarly in the direction $\theta=-\frac{1}{2}\pi$, the asymptotic value for the shock strength at large distances is proportional to

$$\left\{\int_0^{T_1} F(\tau, -\tfrac{1}{2}\pi)\, d\tau\right\}^{1/2}.$$

T_1 is the least non-zero value of τ for which $F(\tau, -\frac{1}{2}\pi)=0$.

For this example, when $\theta=\frac{1}{2}\pi$,

$$\frac{p-p_\infty}{p_\infty}=\frac{0{\cdot}084}{r^{3/4}},$$

and when $\theta=-\frac{1}{2}\pi$,

$$\frac{p-p_\infty}{p_\infty}=\frac{0{\cdot}156}{r^{3/4}}.$$

When $M=2$ the asymptotic formulae overestimate the strength of the front shock wave, produced by the combination, by less than 10 per cent of its true value if $r>91$ when $\theta=-\frac{1}{2}\pi$, and $r>2036$ when $\theta=+\frac{1}{2}\pi$. The unit of length is taken to be the overall length of the combination.

ACKNOWLEDGMENT

The author would like to thank Dr. G. B. Whitham for his guidance in the writing of this paper.

REFERENCES

1. WHITHAM, G. B. The Flow Pattern of a Supersonic Projectile (with an Appendix on two-dimensional steady and one-dimensional unsteady-flows). *Communications in Pure and Applied Mathematics.* Vol. V, p. 290, August 1952.

2. WHITHAM, G. B. On the Propagation of Weak Shock Waves. *Journal of Fluid Mechanics,* Vol. I, p. 290, September 1956.

3. RAO, P. S. Supersonic Bangs, Part I. *The Aeronautical Quarterly,* Vol. VII, p. 135, May 1956.

4. WARD, G. N. *Linearized Theory of Steady High Speed Flow.* Cambridge University Press, 1955.

5. CHESTER, W. Supersonic Flow Past Wing-Body Combinations. *The Aeronautical Quarterly,* Vol. IV, p. 287, August 1953.

6. GOLDSTEIN, S. and WARD, G. N. The Linearised Theory of Conical Fields in Supersonic Flow with Application to Plane Aerofoils. *The Aeronautical Quarterly,* Vol. II, p. 39, May 1950.

Errata

February 1958 (Vol. IX, Part 1)

The paper "The Wave Drag of Wing-Quasi-Cylinder Combinations at Zero Incidence" by L. E. FRAENKEL contains the following printing errors:—

(*i*) In equation (7), p. 59, t should be $\bar{t}$ on the right-hand side of the first line; in the second line, the limits $0, 2\pi$ have been omitted from the first integral sign.

(*ii*) In Table I, p. 64, the ε_w^2 in the top left-hand corner should be underlined.

ACKNOWLEDGMENT

The author would like to thank Dr. G. B. Whitham for his guidance in the writing of this paper.

REFERENCES

1. WHITHAM, G. B. The Flow Pattern of a Supersonic Projectile (with an Appendix on two-dimensional steady and one-dimensional unsteady-flows). *Communications in Pure and Applied Mathematics.* Vol. V, p. 290, August 1952.

2. WHITHAM, G. B. On the Propagation of Weak Shock Waves. *Journal of Fluid Mechanics,* Vol. I, p. 290, September 1956.

3. RAO, P. S. Supersonic Bangs, Part I. *The Aeronautical Quarterly,* Vol. VII, p. 135, May 1956.

4. WARD, G. N. *Linearized Theory of Steady High Speed Flow.* Cambridge University Press, 1955.

5. CHESTER, W. Supersonic Flow Past Wing-Body Combinations. *The Aeronautical Quarterly,* Vol. IV, p. 287, August 1953.

6. GOLDSTEIN, S. and WARD, G. N. The Linearised Theory of Conical Fields in Supersonic Flow with Application to Plane Aerofoils. *The Aeronautical Quarterly,* Vol. II, p. 39, May 1950.

Errata

February 1958 (Vol. IX, Part 1)

The paper "The Wave Drag of Wing-Quasi-Cylinder Combinations at Zero Incidence" by L. E. FRAENKEL contains the following printing errors:—

(*i*) In equation (7), p. 59, t should be $\bar{t}$ on the right-hand side of the first line; in the second line, the limits $0, 2\pi$ have been omitted from the first integral sign.

(*ii*) In Table I, p. 64, the ε_w^2 in the top left-hand corner should be underlined.